
The contribution of spike-frequency adaptation to the variability of spike responses in a sensory neuron

Karin Fisch

Dissertation
an der Fakultät für Biologie
der Ludwig-Maximilians-Universität
München

vorgelegt von
Karin Fisch

München, Juli 2011

Erstgutachter: Prof. Dr. Andreas Herz
Zweitgutachter: PD Dr. Thomas Wachtler
Tag der mündlichen Prüfung: 23.09.2011

Contents

Summary	xiii
Zusammenfassung	xvii
I Introduction	1
1 Spike-response variability	3
2 Sources of spike-response variability	5
2.1 Channel noise	6
3 Role of noise in the nervous system	11
3.1 Noise in sensory systems	11
4 Spike-frequency adaptation in sensory systems	15
5 The auditory system of <i>Locusta migratoria</i>	17
II Material & methods	21
6 Intracellular recordings	23
6.1 Electrophysiology	23
6.2 Stimuli	24
6.3 Data analysis	24
6.3.1 Interspike-interval statistics	24
6.3.2 Spike-count statistics	26
6.3.3 Effective time constants of adaptation	27
7 Model of the locust auditory transduction cascade	29
7.1 Spike generator with spike-frequency adaptation	29
7.2 Model of the mechanosensory transduction process	31
7.3 Kinetic schemes for the stochastic ion channel models	32
7.4 Simulation of stochastic opening ion channels	34

8	Effect of spike-frequency adaptation on the interspike-interval statistics	35
8.1	Hodgkin-Huxley-type model with adaptation	35
9	Effect of spike-frequency adaptation on the spike-count statistics	37
9.1	PIF model with colored noise or stochastic adaptation	37
9.2	Hodgkin-Huxley-type model with two adaptation currents	39
III	Results	41
10	What are the sources of spike-response variability?	43
10.1	Spike-response variability in locust auditory receptor neurons	44
10.1.1	Interspike-interval distributions	46
10.1.2	Interspike-interval correlations	48
10.2	Locust auditory transduction model with ion channel noise	51
10.2.1	Mechanosensitive channel gating	52
10.2.2	Single-current stochasticity	55
11	How does adaptation contribute to the interspike-interval variability?	61
11.1	How noisy adaptation of neurons shapes ISI histograms and correlations .	62
11.2	ISI statistics of a Hodgkin-Huxley-type model with stochastic adaptation .	66
11.2.1	Interspike-interval distributions	66
11.2.2	Interspike-interval correlations	68
11.2.3	Mixed-case model with fast and slow noise sources	69
11.3	Locust auditory transduction model with mixed channel noise sources . .	71
12	How does adaptation contribute to the spike-count variability?	75
12.1	Spike-frequency adaptation with two time constants	75
12.2	Spike-count variability in locust auditory receptors	76
12.3	Locust auditory transduction model with two stochastic adaptation currents	80
13	How do two time scales of adaptation shape the spike-count variability?	85
13.1	Spike-count variability in models with two adaptation currents	86
13.1.1	PIF model driven by colored noise	86
13.1.2	PIF model with adaptation currents	89
13.1.3	Interaction of two adaptation currents	91
13.2	Firing-rate models with two adaptation currents	93
13.2.1	Linear adaptation model	96
13.2.2	Non-linear adaptation model	100
IV	Discussion	105
14	Spike-response variability in locust auditory receptor neurons	107

CONTENTS	vii
15 Different noise sources and how they contribute to the ISI variability	109
16 Effect of multiple time scales of adaptation on the spike-count variability	115
17 Functional role of channel noise	119
References	123
Danksagung/Acknowledgments	137

List of Figures

1.1	Spike-response variability	4
2.1	Conductance variance of a population of ion channels	7
2.2	Variability in the number of open ion channels	8
2.3	The simulation of an action potential with deterministic and stochastic voltage-dependent currents	9
3.1	A potential beneficial effect of a high noise level	13
4.1	Spike-frequency adaptation in an auditory receptor neurons	16
5.1	Müller’s organ	19
5.2	Auditory transduction cascade of locusts	20
10.1	Interspike-interval variability in auditory receptor neurons	45
10.2	Response characteristics of auditory receptor neurons	46
10.3	Comparison of interspike-interval histograms with the colored- and white-noise ISI distributions	47
10.4	Shape of the interspike-interval histograms	49
10.5	Correlations between successive interspike intervals	50
10.6	Auditory signal processing	52
10.7	Influence of the mechanosensitive channel gating on the response properties of the auditory receptor cells	54
10.8	Low-pass filter properties of the mechanosensory receptor channels	55
10.9	Comparison of the interspike-interval variability resulting from different channel-noise sources	56
10.10	Comparison of the diffusion coefficient resulting from different channel-noise sources	57
10.11	Interspike-interval distributions resulting from fast and slow channel noise	58
10.12	Interspike-interval correlations resulting from fast and slow channel noise	59
10.13	Interspike-interval distributions and correlations caused by stochastic potassium channels	60
11.1	Integrate-and-fire dynamics with adaptation channels	63
11.2	ISI histograms of the Traub-Miles model – deterministic vs. stochastic adaptation	67

11.3	Shape parameters of the ISIH for deterministic and stochastic adaptation	68
11.4	Shape parameters of the ISIH as a function of the time scale separation	69
11.5	Serial correlation coefficient at lag 1 as a function of the time scale separation	70
11.6	Serial correlation coefficient as a function of the lag between ISIs	70
11.7	ISI statistics of the Traub-Miles model in the presence of both stochastic adaptation and white noise	71
11.8	ISI statistics of the mixed stochastic channel models	72
11.9	Comparison of the model with stochastic receptor/sodium and adaptation channels with experimental data	73
12.1	Two processes mediating spike-frequency adaptation in locust auditory receptor neurons	76
12.2	Effective time constants of two adaptation processes	77
12.3	Fano factor analysis of the spike trains of an auditory receptor neuron for different sound intensities	78
12.4	Fano factor curves of the locust auditory transduction model with one and two stochastic adaptation currents	81
12.5	Fano factor curves of the locust auditory transduction model with one fast stochastic M-type and one slow stochastic calcium-dependent potassium currents	82
13.1	The exponent κ for different correlation time constants	86
13.2	Fano factor curves of a PIF model driven by Ornstein-Uhlenbeck noise	88
13.3	The exponent κ for different correlation time constants of one vs. two Ornstein-Uhlenbeck noise sources	89
13.4	Fano factor curves of a PIF model with stochastic adaptation currents	90
13.5	Effect of adaptation strength, noise intensity and time constant on the Fano factor curve	91
13.6	Two adaptation currents counteract and affect the ISI and spike-count variability	92
13.7	Variability in a PIF and Traub-Miles model with two stochastic adaptation currents	94
13.8	Variability in a PIF and Traub-Miles model with one fast stochastic and one slow deterministic adaptation current	95
13.9	Linear firing-rate model with two adaptation currents	98
13.10	Comparison of the effective time constants of the firing-rate model with one and two adaptation currents	99
13.11	Generalized firing-rate models with two adaptation currents in comparison to a Traub-Miles model	101

List of Tables

- 13.1 Calculation of the strengths α and β as well as the time constants τ_A and τ_B of two adaptation currents from the mean spike frequency over time . . . 102

Summary

Spike-timing variability is a prevalent feature of neurons that is commonly believed to impact neuronal information processing. Despite this variability of neuronal spike responses, sensorimotor actions can be very precise. For example, if we hear a sound, we are able to localize the sound source and to turn in its direction with a very high accuracy.

So far, little is known about the nature of the sources of neuronal response variability. The most functionally important intrinsic noise source of sensory neurons may arise from the stochastic gating of ion channels. In this thesis, I investigate potential channel noise sources in the auditory receptor neurons of *Locusta migratoria*. The auditory system of locusts is a well-established system for studying the processing of acoustic patterns, and the anatomical and functional properties of the receptor neurons are well understood. To directly measure the noise characteristics of the underlying ionic currents, somatic recordings of sensory neurons are required. These, however, are hard to achieve in the locust auditory system without damaging the sensory transduction machinery. Here, I therefore employ an indirect approach to assess the stochastic dynamics of the sensory neurons based on interspike-interval and spike-count statistics of neuronal spike train responses. This allowed me to record the spike responses of the auditory receptor neurons intracellularly from the auditory nerve far away from the ear. The interspike intervals (ISI) of the spike responses, i.e. the time between subsequent action potentials, as well as the spike count, i.e. the number of action potentials fired in a defined time frame, are statistically analyzed. By means of simulations of integrate-and-fire and conductance-based models, different assumptions of possible noise sources are tested which explain the ISI and spike-count statistics of the experimental data.

The results of this thesis are divided into four sections addressing the following questions:

1. *What are the sources of spike-response variability?* The ISI statistics of the locust auditory receptor cells are analyzed. Spike responses exhibit ISI distributions that can be well described by the inverse Gaussian (IG) distribution and show negative serial ISI correlations for sufficiently low sound intensities evoking spike frequencies of less than 50 Hz. These findings can be explained by a white-noise source that interacts

with an adaptation current. Stimulation with sound intensities that elicit firing rates greater than 50 Hz, in contrast, results in more peaked distributions and positive serial ISI correlations, as expected from an integrate-and-fire model of suprathreshold firing driven by colored noise. Such colored noise potentially arises from a stochastic adaptation current. Simulations of a minimal conductance-based model of the auditory receptor neuron with single stochastic ionic currents exclude the delayed rectifier potassium current as a possible noise source. The simulations instead suggest the receptor or sodium current as possible candidates of the white-noise source while slow channel noise from stochastic adaptation currents may act as the colored-noise source. This shows for the first time that noise from stochastic adaptation currents may have a distinct effect on the ISI statistics and, thus, on the neuronal spike-response variability.

2. *How does adaptation contribute to the interspike-interval variability?* The contribution of adaptation to the interspike-interval variability is theoretically analyzed. I compare two limit cases: (i) stochastic adaptation and (ii) the commonly studied case of a deterministic adaptation current and additive white noise. For fast fluctuations and deterministic adaptation, the ISI density is well approximated by the IG distribution and the ISI correlations are negative. In contrast, for stochastic adaptation, the density is more peaked and has a heavier tail than the IG density and the serial correlations are positive. A mixed case study where both fast fluctuations and adaptation channel noise are present reveals a smooth transition between the limit cases. By means of simulations of a minimal conductance-based model of the auditory receptor neuron with a mixture of stochastic ionic currents from adaptation channels and stochastic receptor or sodium channels the ISI statistics of locust auditory receptor cells can be reproduced. This indicates that two different types of noise sources shape the ISI variability, i.e. slow adaptation channel noise effectively acting as colored noise and fast channel fluctuations effectively acting as white noise. This combination of stochastic currents reproducing the ISI variability, however, is not able to explain the spike-count variability of locust auditory receptor neurons.

3. *How does adaptation contribute to the spike-count variability?* The spike-count variability of locust auditory receptor neurons is analyzed which in contrast to the ISI variability also captures noise processes on long time scales. The variability of the spike count is measured by the Fano factor as a function of the counting time frame length. Locust auditory receptor neurons show minimal Fano factor values for medium counting times and increasing values for large counting times. Furthermore, the experimental data show a shift of the Fano factor minimum and the exponent, that describes the Fano factor increase for large counting times, with increasing sound intensities. Simulations of the locust auditory receptor neurons with two stochastic adaptation currents can explain both the ISI and spike-count statistics of the experimental data. The Fano factor curves can be explained by a second additional adaptation current working on much slower time scales of several seconds is also visible in intracellularly recorded spike responses of long duration.

4. *How do two time scales of adaptation shape spike-count variability?* The contribution of adaptation to the spike-count variability is theoretically analyzed. Simulations of

both integrate-and-fire and conductance-based models reveal a mutual interaction of two adaptation currents that also influences spike-count variability. Analytical solutions for the firing-rate dynamics with two adaptation currents confirms this interaction. Moreover, equations are derived which can be used to estimate the properties of two adaptation currents, i.e. strengths and time constants, from experimentally measured spike responses.

By comparing both the interspike-interval and spike-count statistics of experimental data with the ones known from standard models we were able to infer two distinct noise sources, white- and colored-noise sources, and several time scales of slow noise based on recordings from the auditory nerve that left the delicate ear intact. This demonstrates how higher-order statistics can be used to distinguish different kinds of noise sources. Therefore, the indirect methods introduced in this thesis may be used to uncover potential noise sources in various sensory systems that do not allow direct electrophysiological measurements.

Zusammenfassung

Im zentralen Nervensystem ist Variabilität ein verbreitetes Phänomen in Erregungsmustern von Neuronen, das häufig als nachteilig für die neuronale Signalverarbeitung betrachtet wird. Trotz dieser Variabilität neuronaler Antworten ist es uns jedoch möglich, sensomotorische Abläufe sehr präzise auszuführen. Beispielsweise können wir eine Geräuschquelle sehr genau lokalisieren und uns präzise in die Richtung drehen, aus der das Geräusch kommt.

Bislang ist jedoch nur wenig über die Eigenschaften der Quellen bekannt, die neuronale Variabilität verursachen. Die Stochastizität von Ionenkanälen wird häufig als die funktionell bedeutendste intrinsische Rauschquelle in sensorischen Neuronen angesehen. Diese Arbeit untersucht daher potentielle Ionenkanal-Rauschquellen am Beispiel der auditorischen Rezeptorneurone von *Locusta migratoria* (Wanderheuschrecke). Das auditorische System der Wanderheuschrecke ist ein etabliertes Modellsystem für die Untersuchung der Verarbeitung akustischer Signale. Sowohl die anatomischen als auch die funktionellen Eigenschaften der auditorischen Rezeptorneurone sind sehr gut untersucht. Direkte Messungen der fluktuierenden Ionenströme, die neuronale Variabilität verursachen, erfordern intrazelluläre Ableitungen am Soma sensorischer Neurone. Diese sind jedoch im auditorischen System der Wanderheuschrecke schwer durchzuführen, ohne die sensorische Signalverarbeitung zu beeinträchtigen. Aus diesem Grund stelle ich in dieser Dissertation eine indirekte Methode vor, die es erlaubt, die stochastische Dynamik sensorischer Neurone auf der Grundlage von statistischen Untersuchungen der neuronalen Antworten zu analysieren. Dies erlaubte mir, die neuronalen Antworten der auditorischen Rezeptorneurone im Hörnerv intrazellulär abzuleiten, ohne die Signalverarbeitung im weiter entfernten Ohr zu beeinträchtigen. Die Interspike-Intervalle der neuronalen Antworten, d.h. die Zeit zwischen zwei aufeinanderfolgenden Aktionspotentialen, sowie die Spikeanzahl, d.h. die Anzahl an Aktionspotentialen in einem definierten Zeitfenster, werden statistisch untersucht. Anhand von Computersimulationen werden unterschiedliche Hypothesen möglicher Rauschquellen getestet, die die Statistik der Interspike-Intervalle sowie der Spikeanzahl der experimentellen Daten erklären können.

Die Ergebnisse dieser Dissertation sind in vier Abschnitte gegliedert, welche folgende Fragen behandeln:

1. *Was ist der Ursprung neuronaler Variabilität?* Die Interspike-Intervall-Statistik der auditorischen Rezeptorneurone der Wanderheuschrecke wird analysiert. Für Stimulationen mit Schallintensitäten, die Feuerraten niedriger als 50 Hz hervorrufen, weisen die neuronalen Antworten Interspike-Intervall-Verteilungen auf, die mit der inversen Gauß-Verteilung beschrieben werden können. Die Spikeantworten zeigen weiterhin negative Korrelationen zwischen aufeinanderfolgenden Aktionspotentialen. Dies bedeutet, dass im Mittel entweder ein langes Interspike-Intervall auf ein kurzes folgt und umgekehrt. Diese Ergebnisse können mit einer Rauschquelle erklärt werden, die weißes Rauschen erzeugt und mit einem Adaptationsstrom interagiert, der die Frequenz an Aktionspotentialen bei gleichbleibender Reizung abnehmen lässt. Für Stimulationen mit Schallintensitäten, die Feuerraten höher als 50 Hz hervorrufen, zeigen die neuronalen Antworten dagegen Interspike-Intervall-Verteilungen, die spitzer sind als die inverse Gauß-Verteilung, sowie positive Korrelationen zwischen aufeinanderfolgenden Aktionspotentialen. Diese Eigenschaften sind von überschwellig feuernenden „Integrate-and-Fire“ Modellen bekannt, die durch farbiges Rauschen getrieben werden. Farbiges Rauschen kann von stochastischen Adaptationsströmen erzeugt werden. Simulationen minimaler Leitfähigkeitsmodelle auditorischer Rezeptorneurone mit einzelnen stochastischen Ionenströmen schließen den verzögerten Gleichrichter-Kaliumstrom als Rauschquelle aus. Die Simulationen deuten stattdessen darauf hin, dass stochastische Ionenströme von Rezeptor- bzw. Natriumkanälen mögliche Quellen für weißes Rauschen darstellen, während langsames Kanalrauschen stochastischer Adaptationsströme als farbiges Rauschquelle wirken kann. Diese Ergebnisse zeigen erstmals, dass Rauschen von stochastischen Adaptationsströmen einen deutlichen Effekt auf die Interspike-Intervall-Statistik und somit auch auf die Variabilität neuronaler Antworten haben kann.

2. *Welchen Einfluss hat Adaptation auf die Interspike-Intervall Variabilität?* Der Einfluss von Adaptation auf die Interspike-Intervall Statistik wird theoretisch untersucht. Dabei vergleiche ich zwei Grenzfälle miteinander: (i) stochastische Adaptation und (ii) deterministische Adaptation plus additives weißes Rauschen. Der letztere Grenzfall zeigt Interspike-Intervall-Wahrscheinlichkeitsdichten, die mit der inversen Gauß-Verteilung beschrieben werden können, sowie negative Korrelationen zwischen benachbarten Aktionspotentialen. Im Gegensatz dazu weist der Grenzfall der stochastischen Adaptation spitzere Verteilungen und positive Korrelationen auf. Simulationen, die sowohl schnelle Fluktuationen als auch langsames Adaptationskanalrauschen beinhalten, ergeben einen gleichmäßigen Übergang zwischen den beiden Grenzfällen. Simulationen minimaler Leitfähigkeitsmodelle auditorischer Rezeptorneurone mit einer Kombination aus stochastischen Adaptationsströmen und stochastischen Rezeptor- bzw. Natriumströmen können die komplette Interspike-Intervall-Statistik der experimentellen Daten reproduzieren und erklären. Dies weist darauf hin, dass zwei unterschiedliche Typen von Rauschquellen die Variabilität neuronaler Antworten der auditorischen Rezeptorzellen der Wanderheuschrecke beeinflussen: Zum einen schnelle Ionenkanalfluktuationen, die wie weißes Rauschen wirken, und zum anderen langsame Adaptationskanäle, die als farbiges Rauschen wirken. Diese Kombination aus stochastischen Ionenströmen, die die Interspike-Intervall-Statistik der auditorischen Rezeptorneurone reproduzieren kann,

erweist sich jedoch als nicht ausreichend, um die Variabilität in der Spikeanzahl zu erklären.

3. *Welchen Einfluss hat Adaptation auf die Variabilität in der Spikeanzahl?* Die Variabilität der Spikeanzahl neuronaler Antworten auditorischer Rezeptorneurone der Wanderheuschrecke wird analysiert. Diese zeigt im Gegensatz zur Interspike-Intervall Variabilität zusätzlich Effekte von Rauschquellen, die auf langen Zeitskalen wirken. Die Variabilität in der Spikeanzahl wird anhand des Fano-Faktors quantifiziert, der für verschiedene Zeitfenster berechnet wird. Die auditorischen Rezeptorneurone zeigen minimale Fano-Faktor-Werte für mittlere Zeitfenster und steigende Werte für lange Zeiten von mehreren Sekunden. Außerdem weisen die experimentellen Daten eine Verschiebung des Minimums und des Exponenten, mit dem die Fano-Faktor-Kurve ansteigt, für steigende Schallintensitäten, die zur Stimulation genutzt wurden auf. Simulationen der auditorischen Rezeptorneurone zeigen, dass die Kombination aus stochastischen Rezeptor- bzw. Natriumströmen sowie von Ionenströmen zweier stochastischer Adaptationskanäle sowohl die Spikeanzahl- als auch Interspike-Intervall-Variabilität der experimentellen Daten reproduzieren und erklären kann. Der zweite zusätzliche Adaptationsstrom, der eine Zeitkonstante von mehreren Sekunden aufweist, erklärt die Verschiebungen sowie die hohen Fano-Faktor-Werte für lange Zeitskalen. Diese zusätzliche Adaptation der Spikefrequenz wird auch in intrazellulären Ableitungen mit einer Dauer von einer Minute sichtbar.

4. *Wie beeinflussen zwei Adaptationsströme die Variabilität in der Spikeanzahl?* Der Einfluss von Adaptation auf die Statistik der Spikeanzahl wird theoretisch untersucht. Simulationen von „Integrate-and-Fire“ als auch Leitfähigkeits-Modellen mit Adaptation zeigen, dass zwei Adaptationsströme interagieren und einander entgegenwirken. Diese Interaktion beeinflusst die Variabilität neuronaler Antworten und die Form der Fano-Faktor-Kurven. Analytische Lösungen eines phänomenologischen Feuerratenmodells mit Adaptation auf zwei Zeitskalen bestätigen diese Interaktion. Weiterhin werden Gleichungen hergeleitet, die es erlauben, Adaptationsparameter, d.h. Stärken und Zeitkonstanten zweier Adaptationsströme, von experimentell gemessenen Spikeantworten zu bestimmen.

Durch den Vergleich der Spikeanzahl- und Interspike-Intervall-Statistiken experimenteller Daten mit denen, die von Standard-Neuronenmodellen bekannt sind, können in dieser Arbeit zwei unterschiedliche Typen von Rauschquellen (weißes Rauschen und farbiges Rauschen auf zwei Zeitskalen) anhand von intrazellulären Ableitungen im Hörnerv unterschieden werden, die das empfindliche Ohr der Wanderheuschrecke unversehrt lassen. Diese Ergebnisse zeigen, wie Statistik höherer Ordnung eine Unterscheidung unterschiedlicher Rauschquellentypen ermöglicht. Die hier dargestellten indirekten Methoden können daher auch in anderen sensorischen Systemen Anwendung finden, die direkte elektrophysiologische Messungen ausschließen.

Part I. INTRODUCTION

*Spike-response variability in the auditory system of
Locusta migratoria*

Spike-response variability

Spike-response variability is a prominent and ubiquitous characteristic of neuronal responses (see Fig. 1.1 as example). These fluctuations, both in spike timing and in spike count, can be observed both within (“intra-trial variability”) and across stimulus repetitions (“trial-to-trial variability”). The variability can be expressed both in the time between two action potentials, i.e. the interspike intervals (“interspike-interval variability”), and in the number of spikes (“spike-count variability”). The question how the nervous system is able to ensure reliable responses, such as a behavioral output, within a noisy environment is a fundamental issue in neuroscience.

However, not all neurons were found to show equal variability. Neurons which were stimulated intracellularly with a known time-dependent input current displayed spike activity which seemed to be almost deterministic (Bryant and Segundo, 1976; Mainen and Sejnowski, 1995). A much more regular spike timing was found in neurons during stimulation with rapidly changing external stimuli in contrast to stimulations with constant or slowly varying stimuli (Bair and Koch, 1996; Berry et al., 1997; de Ruyter van Steveninck et al., 1997). On the other hand, neurons can also generate very irregular spike responses in the absence of any temporally structured stimuli (Rose, 1979; Softky and Koch, 1993; Kostál and Lánský, 2008). This suggests that a neuron’s spiking behavior may depend on the stimulus itself.

Variability in neuronal responses may set limits to the discrimination of sensory stimuli. In the brains of both vertebrates and invertebrates, it was shown that the degree of neuronal variability even increases for higher stages of sensory processing. Given the same stimulus, lowest variability was found for the periphery with increasing variability for higher-order neurons, such as cortical neurons (Kara et al., 2000; Prut and Perlmutter, 2003; Vogel et al., 2005; Ronacher et al., 2008). Despite this variability it is astonishing how precisely and reliably sensorimotor actions, for instance, can be performed. If we hear a sound, we are able to localize the sound source and to turn in its direction with a very high accuracy.

In order to comprehend neuronal codes used for the representation and processing of a sensory input and how a reliable signal processing is possible, it is important to

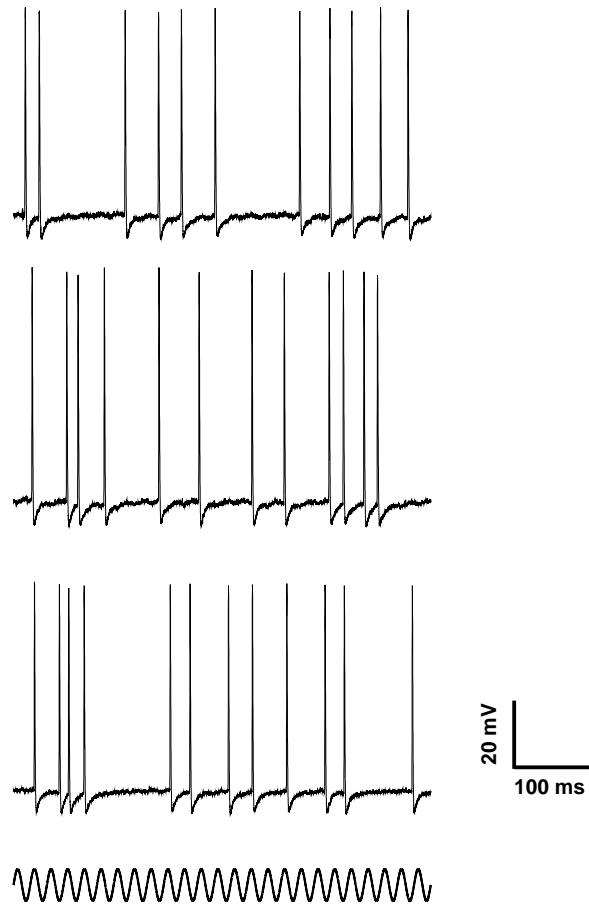


Figure 1.1: Spike-response variability. Three different traces of spike responses that were recorded intracellularly from a locust auditory receptor neuron during stimulation with a pure-tone stimulus of constant sound intensity (schematically drawn as slow sine wave).

understand the nature and origin of the observed response variability. To this end, the focus of this thesis is what the sources of spike-response variability are and how we can identify and analyze them.

Sources of spike-response variability

In the nervous system, variability can be found at various levels which range from the detection of sensory stimuli to the generation of motor responses. Spike-response variability is usually considered to result from neuronal noise (Shadlen and Newsome, 1994, 1998). Various noise sources are known that have a strong contribution to neuronal response variability (see Faisal et al., 2008 for a review). We can classify them into two groups: (i) extrinsic and (ii) intrinsic noise sources.

Variability at the first stages of signal processing can arise from extrinsic noise which enters with the sensory stimulus. Via the signal transduction pathway this noisy sensory stimulus will be amplified and, subsequently, converted into an electrical signal by the receptors. An example of such noise in the visual system is given by photon noise which causes fluctuations of the depolarizing currents of photoreceptor neurons by the quantal nature of light (Grewe et al., 2003, 2007). These fluctuations, in turn, may cause variability in spike responses of higher-order neurons. In the auditory system, the temporal structure of an acoustic stimulus may be distorted by environmental noise or the interference from other objects before arriving at the ear (Richard and Wiley, 1980; Römer and Lewald, 1992; Brumm et al., 2004).

A second type of extrinsic noise, which directly affects single neurons is given by synaptic noise resulting from the synaptic bombardment of a myriad of synapses (Calvin and Stevens, 1967, 1968). Synaptic noise is very complex and can originate from different sources. Factors affecting the post-synaptic responses are e.g., the quantal release of neurotransmitters (Castillo and Katz, 1954), variations in the neurotransmitter concentration within the synaptic cleft (Franks et al., 2003) or stochastic fluctuations in the number of activated postsynaptic receptors (Faber et al., 1992).

Noise sources which arise at the level of an individual neuron are called intrinsic noise sources. Thermal noise is an ubiquitous intrinsic noise source. Thermal agitation of electrons due to the passive membrane resistance gives rise to random fluctuations in the membrane potential ("Johnson noise", Johnson, 1928). Fluctuations can also arise from the transmission of a finite number of electrons or ions through leak channels or other pores in the neuronal membrane ("Shot noise", Frehland and Faulhaber, 1980). In the

auditory system, thermal noise can lead to thermal fluctuations of the hair bundles, e.g. when fluid molecules collide with the auditory hair bundles due to Brownian motion (Jaramillo and Wiesenfeld, 1998; Nadrowski et al., 2004). Thermodynamic noise can also affect tastes and smells due to a random arrival of diffusing molecules at the receptor sites (Berg and Purcell, 1977; Bialek and Setayeshgar, 2008). It was, however, shown that the effect of these noise sources on the spike-response variability is very small (Lecar and Nossal, 1971; Manwani and Koch, 1999).

The most functionally important intrinsic noise source of sensory neurons concerning the neuronal dynamics may arise from ion channel noise (White et al., 2000). The membrane conductance of a neuron is directly proportional to the number of open ion channels which show an intrinsically stochastic behavior (Hille, 2001). The resulting conductance fluctuations caused by a finite number of ion channels result in variability in neuronal spike responses.

2.1 Channel noise

Already very early, with the work of Hodgkin and Huxley (1952), gating variables were introduced which are nowadays interpreted as ion channel opening probabilities. The first patch-clamp recordings of single ion channels by Neher and Sakmann (see e.g., Sakmann and Neher, 1995) have then experimentally shown that ion channels in the neuronal membrane are stochastic molecular structures. The recorded currents demonstrated that ion channels can very rapidly switch between conducting and non-conducting states.

The transitions between the different channel states are usually modeled based on Markov schemes (Colquhoun and Hawkes, 1977). The most simple description of a voltage-dependent ion channel is given by the following two-state scheme:



where $\alpha(V)$ and $\beta(V)$ define the voltage-dependent transition rates between the open and closed state. Several ion channels, however, have more than two states. These are defined by a Markov scheme with a specified number of states as well as rate constants which define the transition between all possible states.

Each state of a Markov scheme corresponds biophysically to a change in the conformation of the channel protein subunits (Hille, 2001). In the case of voltage-gated ion channels, a depolarisation of the cell can cause the helix of a protein domain to move and, as a consequence, change the protein conformation. The conformational change of ligand-gated ion channels can be caused by the binding of a ligand at the receptor site of the channel. In the case of mechanosensory ion channels, mechanical forces (e.g. stretch or bending of the cell membrane, channel or membrane displacement by a tether) can directly gate the channels which are attached to the membrane (Kung, 2005). Since not

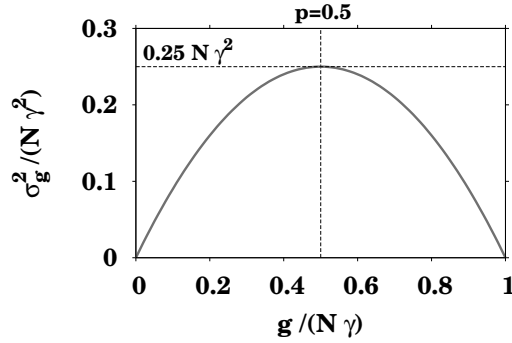


Figure 2.1: Conductance variance of a population of ion channels. The channel open probability $p = g/(N\gamma)$ and the conductance variance $\sigma_g^2/(N\gamma^2) = p(1-p)$ are given by Eqs. (2.2)-(2.3). The variance is maximal for an open probability $p = 0.5$ where the variance is $\frac{1}{4}N\gamma^2$ (black dashed line).

every transition between all states is possible, a Markov gating scheme defines only the transitions that are permitted.

The probabilistic transitions between the states of each channel of a channel population in a neuronal membrane causes fluctuations of the total membrane current in a cell. Assuming that the channel states are independent, the total conductance g of N ion channels and its variance σ_g^2 are given by (Ehrenstein et al., 1970; Begenisich and Stevens, 1975):

$$g = Np\gamma \quad (2.2)$$

$$\sigma_g^2 = Np(1-p)\gamma^2 \quad (2.3)$$

where γ is the single-channel conductance and $p = \alpha/(\alpha + \beta)$ is the mean steady-state open probability of a channel.

The open probability p is one factor strongly influencing neuronal noise. Open probabilities of voltage-dependent ion channels, for instance, change with the membrane potential. For the steady-state open probability $p = 0.5$, the variance of the current passing the channels is highest (see Fig. 2.1, Sigworth, 1980), because the number of occurring state transitions is maximal. For smaller and larger open probabilities, respectively, the conductance/current fluctuations decrease. When all channels are either completely open or closed, the noise level is zero.

The variance of the fluctuations is dependent on the number of channels. This becomes obvious when we regard the number of open channel channels, N_o , as a function of time (see Fig. 2.2). Small N yield large fluctuations in the number of open (conducting) channels in relation to the mean N_o (see Fig. 2.2A,C). Large N , in contrast, result in small relative variability (see Fig. 2.2B,D).

The fluctuations decline proportionally to the square root of the ion channel number (White et al., 2000). Quantifying the conductance noise level by the coefficient of variation, which is given by the ratio of the standard deviation to the mean (see Eq. (2.2)-(2.3)),

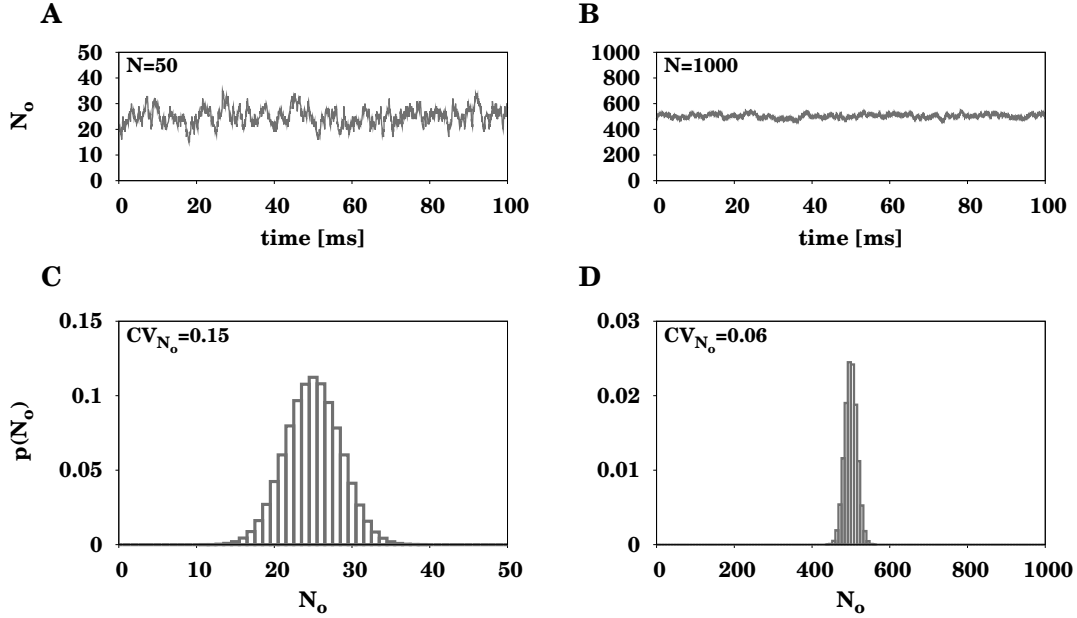


Figure 2.2: Variability in the number of open ion channels. **A,B** Number of open channels N_o over time out of a total of (A) $N = 50$ and (B) $N = 1000$ stochastic two-state ion channels ($p = 0.5$). **C,D** The distribution of N_o for the same simulation shown in A and B. CV_{N_o} defines the ratio of the standard deviation to the mean N_o .

gives us:

$$CV_g = \frac{\sigma_g}{g} = \sqrt{\frac{1-p}{Np}}. \quad (2.4)$$

Hence, small N yields large relative fluctuations with a high CV_g for a given steady-state open probability p and vice versa.

Another factor which affects spike-response variability is given by the single-channel conductance γ . In a current trace of a single-channel patch-clamp recording, this effect becomes obvious when we look at the current steps when an ion channel opens (see e.g., Neher and Stevens, 1977). The open-channel current is given by the product of the voltage and the single-channel conductance, $i(V) = \gamma(V - E)$ where V is the membrane potential and E is the reversal potential. If γ is large, the current steps visible in current traces are large. The contrary holds true for small γ . This effect can be shown in simulations of action potential generation with different sodium and potassium channel numbers, N_K and N_{Na} , and with a single-channel conductance which is proportional to the channel numbers, $\gamma_K = g_K/N_K$ and $\gamma_{Na} = g_{Na}/N_{Na}$ where g_K and g_{Na} are the total-channel conductances (see Fig. 2.3). Simulations with large N_K and N_{Na} result in voltage-dependent currents responsible for action potential generation that do not show current steps and seem to behave like deterministic currents (see Fig. 2.3A). Small N_K and N_{Na} , in contrast, yield large current steps demonstrating the stochastic nature of the

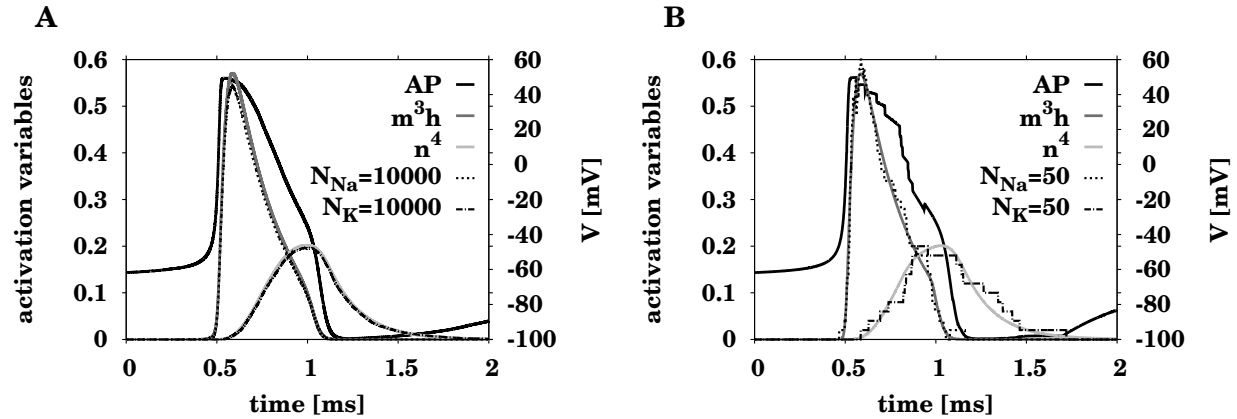


Figure 2.3: The simulation of an action potential with deterministic and stochastic voltage-dependent currents. The currents responsible for the generation of an action potential (AP, black solid lines) causing a change of the membrane potential V were mediated by deterministic (dark and light gray solid lines) or stochastic sodium and delayed-rectifier potassium channels (black dashed lines). They are proportional to the open probabilities of the deterministic currents which are determined by the Hodgkin-Huxley activation variables m^3h defining the open state of the deterministic sodium channel and n^4 for the open state of the deterministic potassium channels. The corresponding stochastic currents passing (A) $N_{Na} = 10000$ sodium and $N_K = 10000$ potassium channels and (B) $N_{Na} = 50$ sodium and $N_K = 50$ potassium channels, respectively, were simulated using Gillespie's algorithm (see section 7.4). The total-channel conductances were kept constant at $g_K = 80 \text{ mS/cm}^2$ and $g_{Na} = 100 \text{ mS/cm}^2$, while the single-channel conductances were scaled with $\gamma_K = g_K/N_K$ and $\gamma_{Na} = g_{Na}/N_{Na}$.

ion channels, which in addition affect the evolution of the membrane potential during an action potential (see Fig. 2.3B).

To understand the implications of biophysical noise sources, such as channel noise, on signal processing in the nervous system, it will be important to decode the basic concepts of channel noise in more detail.

Role of noise in the nervous system

Noise in the nervous system is ubiquitous and has to be considered when discussing neural information processing. Variability at the single neuron level translates into noise at higher-order neurons which even increases with increasing neuronal level (Kara et al., 2000; Prut and Perlmutter, 2003; Vogel et al., 2005; Ronacher et al., 2008). This suggests that variability may place limits on the reliability of behavioral responses.

In sensorimotor systems, a precise motor control requires accurate knowledge of the current body position and reliable processing of the sensory input. A sensory input, for instance, may be an acoustic signal eliciting a movement in the direction of the sound source. For the performance of this task, it is important to precisely localize the acoustic signal and, additionally, to accurately determine the movement angle to approach the sound source. Although neuronal responses are quite variable, motor performance, however, can be very precise. This suggests that the nervous system can cope with noisy neuronal responses and that variability in the nervous system may offer distinct advantages and play a specified functional role in information processing.

To analyze the role of noise in a sensorimotor system, it is important to first understand the variability and its origin at the very early stages of signal processing. In this thesis, we therefore focus on noise at the first stage of perception, i.e. on noise in sensory receptors neurons.

3.1 Noise in sensory systems

In sensory systems, a basic but crucial task in perception is the recognition and localization of stimuli, like objects, smells or sounds. The goal of the nervous system is to extract the relevant stimulus characteristics while ignoring unwanted background information.

Subthreshold noise has been shown to help enhance the detection and the extraction of the relevant information of weak signals when an optimal level of background noise is present. This phenomenon is called “stochastic resonance” (Benzi et al., 1981; Wiesenfeld and Moss, 1995; McDonnell and Abbott, 2009). Stochastic resonance can have a beneficial

effect on the transmission of details for instance about the stimulus shape (see Fig. 3.1). A subthreshold sine wave (see Fig. 3.1A) or square pulse stimulus (see Fig. 3.1B) with added low-amplitude white noise can yield action potentials at a relatively fixed period of the stimulus where the stimulus is closest to the spike threshold (see Fig. 3.1C,D). These spike responses may be hardly distinguishable for sine and square wave stimuli with the same cycle period. In this case, this means that it is not possible to extract information about the stimulus shape from the spike responses. Adding stronger noise to the same subthreshold stimuli, in contrast, can result in spike responses (averaged over many stimulus repetitions) which follow the distinct stimulus shapes (see Fig. 3.1E,F). At stimulus phases where the subthreshold stimulus is close to the spike threshold, the neuron generates action potentials with higher probabilities and vice versa. Thus, a higher noise level may yield spike responses with action potentials at all stimulus phases, and the spike probability, hence, can follow the shape of the stimulus.

Stochastic resonance has been reported in a range of sensory systems. Examples include the mechanoreceptor cells of crayfish (Douglass et al., 1993), shark multimodal sensory cells (Braun et al., 1994), cercal sensory neurons of cricket (Levin and Miller, 1996) and human muscle spindles (Cordo et al., 1996). One functional role was suggested in the extension of the dynamic range of neurons (Stocks, 2000). Another role of noise was reported in the alteration of firing patterns by means of changes of the noise level due to temperature or electric-field gradients (Braun et al., 1994, 1997). In studies on paddlefish, stochastic resonance was shown to enhance the detection and capture of *Daphnia*, i.e. planktonic prey, which suggests a functional role in animal behavior (Russell et al., 1999).

The phenomenon of stochastic resonance is also known to occur in ion channels that switch between two states that are separated by an energy barrier (Bezrukov and Vodyanoy, 1995; White et al., 1998; Parc et al., 2009). To switch from one state to another, the energy difference has to be overcome. A weak signal will not have enough energy to induce a state transition. The addition of noise, however, will occasionally yield an escape from the well and induce a transition. In sensory systems, an optimal noise level will, hence, yield a maximal signal-to-noise ratio for which a weak sensory signal is optimally transduced.

Suprathreshold stochastic resonance is a particular variant of stochastic resonance which unlike the classical one is not restricted to a weak subthreshold signal. This type reveals a facilitation of information by noise through a parallel array of independent threshold devices (Stocks, 2000). Regarding the nervous system, this means that a population of sensory neurons receiving the same input signal may collectively encode a stimulus. The output from all devices or neurons is then summed up to give an overall output response. This may be beneficial, for instance, for the detection of suprathreshold acoustic stimuli in a loud environment.

A recent theoretical study showed that suprathreshold stochastic resonance may be induced by ion channel fluctuations and that an optimal amount of channel fluctuations may optimize signal transmission (Ashida and Kubo, 2010). This suggests that channel noise potentially plays a crucial role in population coding in neurons.

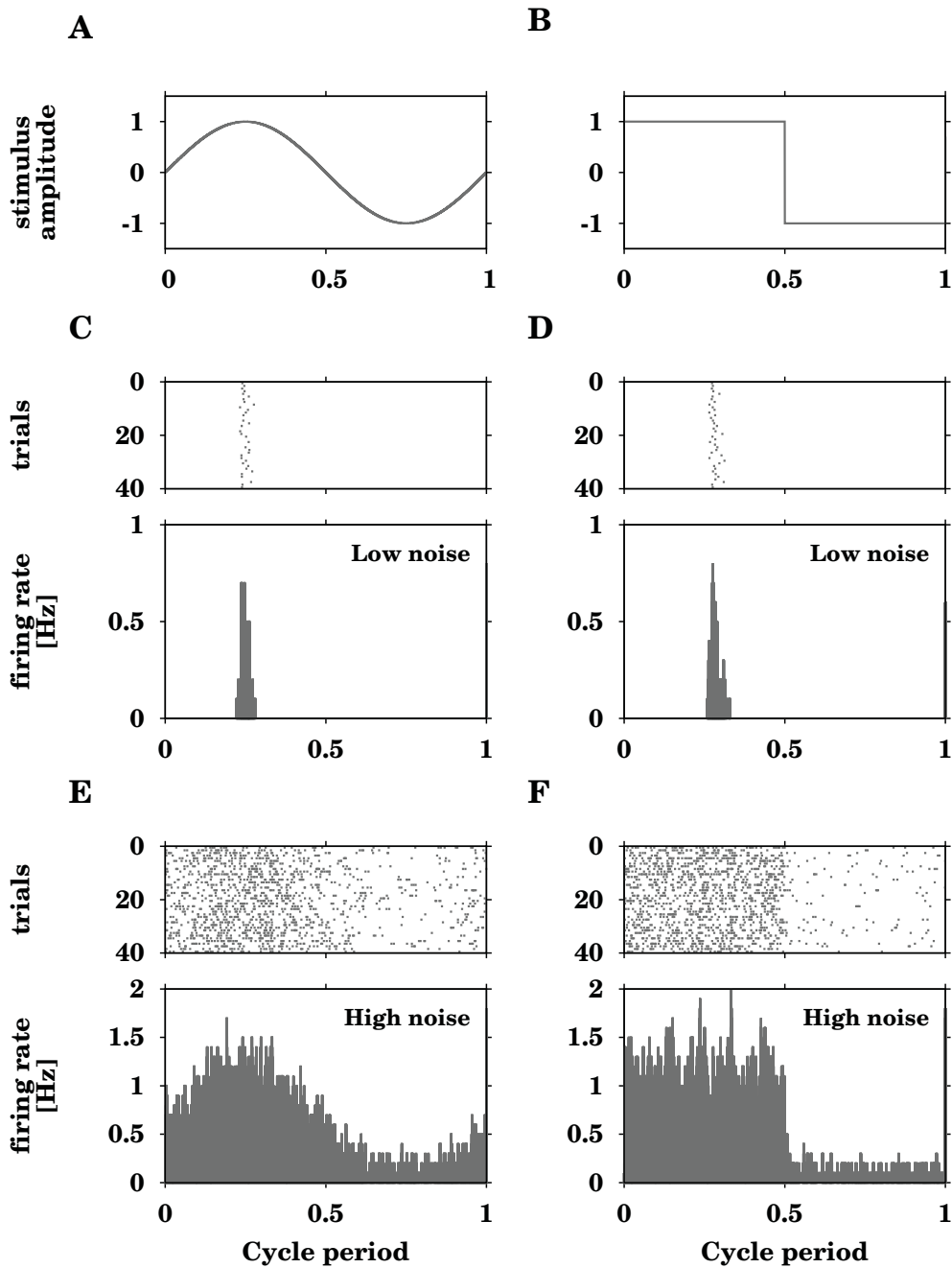


Figure 3.1: A potential beneficial effect of a high noise level. Leaky integrate-and-fire model driven by a subthreshold **A,C,E** sine wave or **B,D,F** step pulse stimulus and additional white noise input. **C,D** A low noise level yields spike responses (top: 40 out of 100 trials, bottom: mean event rate across all trials) for both stimuli which occur at a relatively fixed phase of the cycle and which are indistinguishable for a (A) sine and (B) square wave. **E,F** High noise, in contrast, results in spike responses (top: 40 out of 100 trials, bottom: mean event rate across all trials) which last for the whole cycle and follow the different shapes of the stimuli.

Beside the effects of stochastic resonance, it was furthermore shown that noise in combination with negative correlations between interspike intervals can improve information transmission (Chacron et al., 2001). Positive interspike interval correlations give rise to Fano factor curves quantifying spike-count variability which express a minimum for a defined observation time (Middleton et al., 2003). This indicates that noise may define time frames for which signal detectability is optimal.

Various studies have demonstrated a constructive role of noise in the transmission of neuronal signals. However, little is known about the specific underlying mechanisms causing variability and how they work.

Spike-frequency adaptation in sensory systems

Spike-frequency adaptation is a widespread phenomenon throughout the nervous system and denotes the reduction of the firing rate of neurons to prolonged stimuli (see Fig. 4.1 as example). This phenomenon has been observed in many sensory neurons of both vertebrates and invertebrates, such as in the visual (Laughlin, 1989; Peron and Gabbiani, 2009a), olfactory (Demmer and Kloppenburg, 2009), electrosensory (Nelson et al., 1997; Benda et al., 2005) or auditory system (Westerman and Smith, 1984; Epping, 1990; Givois and Pollack, 2000; Ronacher et al., 2004).

Spike-frequency adaptation is likely to play a crucial role in shaping spike-response variability (Gabbiani and Krapp, 2006). Such noise shaping is known from models with dynamic thresholds (Chacron et al., 2004). In a recent study, it was shown that adaptation can account for a reduction of the noise level in neurons and facilitate population coding in neural ensembles (Farkhooi et al., 2011). However, only little is known about a potential functional role of spike-frequency adaptation in shaping the spike-response variability of sensory neurons.

So far, three major functional roles of spike-frequency adaptation have been described. Adaptation was shown to shift the dynamic range of neurons thereby causing forward masking. Forward masking is a temporal analog to lateral inhibition in which a neuronal response to a stronger stimulus, like a loud sound, suppresses the response to a subsequent weaker input (Sobel and Tank, 1994). This temporal inhibition may be used to induce selective attention to preferred stimuli. Another role may be given by high-pass filtering in sensory neurons. Using high-pass filter properties, neurons can separate fast and slow stimulus components which yields an enhancement of the response to fast stimulus components independent of the stimulus intensity (Benda et al., 2005). A third role of spike-frequency adaptation has been described as a selectivity filter. This means that adaptation selectively reduces the spike response to non-preferred stimuli (Peron and Gabbiani, 2009a).

Spike-frequency adaptation can result from different mechanisms, such as the trans-

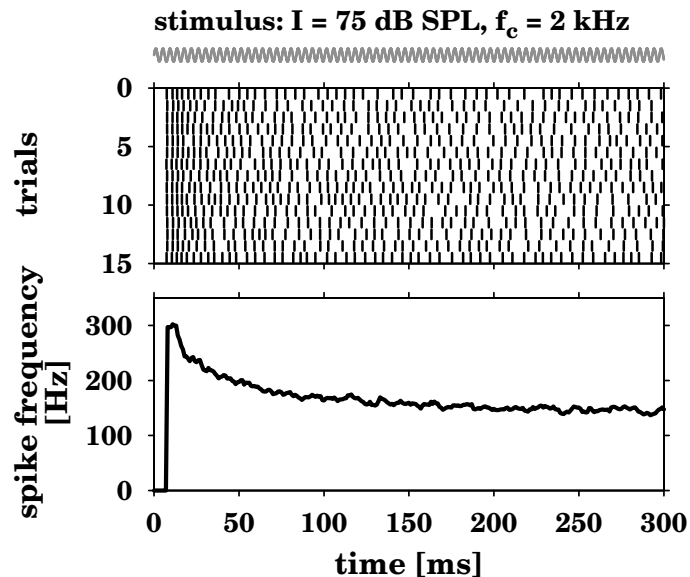


Figure 4.1: Spike-frequency adaptation in an auditory receptor neuron. Spike-responses were intracellularly recorded from axons in the locust auditory nerve during stimulation with a 2 kHz pure tone of 75 dB SPL sound intensity (schematically drawn as a slow sine wave). *top*: The first 15 out of 70 recorded spike trains. *bottom*: The spike frequency calculated as the inverse interspike interval shows spike-frequency adaptation, i.e. a reduction of an initially high spike frequency to prolonged stimulation.

duction process of receptor neurons (Hudspeth et al., 2000; Gollisch and Herz, 2004; Albert et al., 2007), synaptic depression (Abbott et al., 1997; Chance et al., 1998) or inhibitory inputs (Finlayson and Adam, 1997; Ingham and McAlpine, 2005). Within the variety of mechanisms causing spike-frequency adaptation ionic currents that are induced by the spike response of neurons are of particular importance. These ionic currents can result from voltage-dependent M-type (Brown and Adams, 1980; Storm, 1990) or calcium-activated potassium channels (Madison and Nicoll, 1984; Vergara et al., 1998; Sah and Davies, 2000) which have an inhibitory effect on the spike-response. Another important type of adaptation currents which are activated by the neuron's output results from the slow inactivation of voltage-dependent sodium channels (Fleidervish et al., 1996; Vilin and Ruben, 2001; Torkkeli et al., 2001; Kim and Rieke, 2003). This type of adaptation results from a reduction in the number of sodium channels available for the generation of action potentials and, thus, reduces the excitability of a neuron.

The auditory system of *Locusta migratoria*

The auditory system is a prominent sensory system where the action potential generation is influenced by both stochastic current fluctuations and spike-frequency adaptation (Manley and Müller-Preuss, 1978; Ingham and McAlpine, 2004; Schaette et al., 2005; Avissar et al., 2007; Kuznetsova et al., 2008). In this thesis, we explore how spike-frequency adaptation and other noise sources may contribute to the spike-response variability in the auditory system. We analyze this issue in the auditory system of *Locusta migratoria* which is simply structured and well established as a model system with several parallels to the vertebrate auditory system.

In auditory systems, the most relevant information about a sender and its communication signals is carried by the temporal structure and by amplitude modulations of an acoustic signal (Shannon et al., 1995; Joris et al., 2004). The reliable processing of the signal's information is, therefore, crucial for the recognition, localization, as well as interpretation of acoustic signals especially with fast amplitude modulations and specific temporal patterns. However, signal recognition and processing are usually constrained by different noise sources on various levels of signal processing. This may limit for instance the detection of weak signals in a loud environment (e.g. in a jungle) or the discrimination of conspecific signals from songs of different species in the same biotope.

In many grasshopper species, acoustic communication signals play an important role in mating in terms of attracting sexual partners. Acridid grasshoppers generate their mating call songs by rubbing the inner side of the femur of their hind legs in a species-specific temporal pattern against a vein of the forewings ("stridulation", von Helversen, 1972; von Helversen and von Helversen, 1997). The communication occurs in a bidirectional manner. Male grasshoppers start the communication and produce calling songs to attract females. If a female recognized and accepted the conspecific song, she responds with a song of a similar pattern. Upon hearing this response, the male turns very rapidly towards the direction of the female ("phonotaxis") and moves forward. This procedure is then repeated and, that way, the male approaches the female in a stepwise manner.

The auditory receptor cells constitute the first stage of auditory signal processing in

grasshoppers. They are mechanosensory and convert incoming sound pressure waves into neuronal signals. In locusts, the somata of a total of 60-80 receptor cells are located in the auditory ganglion (Popov and Svetlogorskaya, 1972; Michelsen, 1971), the so called Müller's organ, which is attached to the inner surface of the tympanal membrane (eardrum) on both sides of the animal (see Fig. 5.1A-C). Their axons extend through the auditory nerve to the metathoracic ganglion (Stumpner and Ronacher, 1991; Stumpner et al., 1991). From there, they project onto local neurons which in turn are directly connected to ascending neurons transmitting information to the brain. The auditory nerve is easily accessible. This allows intracellular recordings of receptor spike responses from single axons in the nerve without damaging the sensory transduction machinery.

The anatomy and organization of the auditory ganglion of *Locusta migratoria* was described in detail by Gray (1960). The auditory receptor cells of locusts are chordotonal organs which are prevalent structures in insect mechanoreception. They are composed of specialized sensilla, the so called scolopidia, which contain one bipolar neuron, i.e. the receptor neuron. Their dendrites bear a single cilium at its tips. This cilium is connected to the tympanal membrane via an attachment cell. The dendrites of all receptor neurons project to four different attachment sites each exhibiting different resonance characteristics. The locations of maximal tympanal displacements were shown to depend on the sound frequency (Michelsen, 1971). Characteristic frequencies are about 4 kHz for low-frequency receptor cells, and about 15 kHz for high-frequency receptor cells (Römer, 1976). These tuning properties resemble a *place principle* similar to the one known for vertebrates (Michelsen, 1971; Windmill et al., 2008).

The functional properties of locust auditory receptor cells and the transduction from acoustic signals to receptor responses have been extensively investigated (Machens et al., 2001, 2003; Gollisch et al., 2002; Gollisch and Herz, 2005; Rokem et al., 2006). Using stimulus reconstruction techniques, it was shown that already single auditory receptor cells are able to precisely represent amplitude modulations of an acoustic signal with a high signal-to-noise ratio (Machens et al., 2001). Specifically, in response to stimuli with steep amplitude rises, receptors show a very precise spiking behavior (Krahe and Ronacher, 1993; Rokem et al., 2006). This is in marked contrast to acoustic stimuli with small or no amplitude modulations which yield high spike-response variability in auditory receptor cells (Machens et al., 2001; Schaette et al., 2005).

The underlying mechanosensory signal transduction process is well understood in respect to a transduction cascade consisting of linear filters and static nonlinearities (Gollisch et al., 2002; Gollisch and Herz, 2005). A schematic view of the locust auditory transduction cascade from sound input to the generation of action potentials in auditory receptor neurons is given in Fig. 5.2: A sound pressure wave causes the tympanal membrane to vibrate (Scholten et al., 1981; French, 1988; Robert and Göpfert, 2002). As a result, mechanosensory ion channels in the membrane of auditory receptor neurons open and transform the vibrations into electrical currents (Hill, 1983; Gillespie and Walker, 2001). Our hypothesis is that this channel opening is a stochastic process causing fluctuating ionic currents through the membrane which in turn are responsible for spike-timing variability.

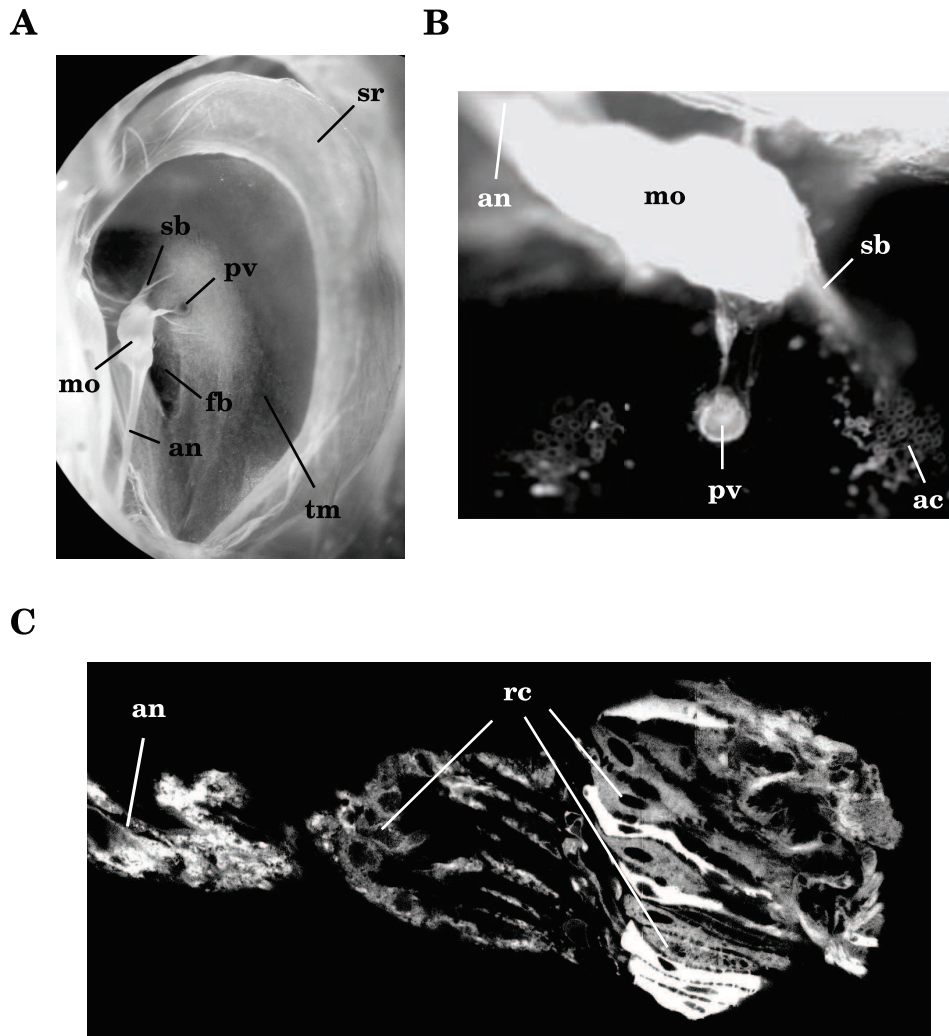


Figure 5.1: Müller's organ. **A** Photograph of the ear of *Locusta migratoria* from the inside of the animal. The tympanal membrane (*tm*) is spanned up by a sclerotized ring (*sr*). The Müller's organ (*mo*) which contains 60-80 auditory receptor cells (*rc*) is attached to the inner surface of the tympanal membrane via attachment cells (*ac*). **B,C** View of the Müller's organ after a backfill with biocytin and after fluorescence labeling with Streptavidin-Cy3 visualized with (B) a fluorescence microscope and (C) a confocal laser scanning microscope. *an*: auditory nerve, *sb*: styliform body, *pv*: pyriform vesicle, *fb*: folded body.

In this thesis, we investigate the source of the spike-response variability observed in recordings of auditory receptor cells of *Locusta migratoria* (Hill, 1983; Ronacher et al., 2004; Schaette et al., 2005, see also Fig. 1.1). The broad background of experimental and theoretical studies on the auditory system of locusts makes this system a suitable model system to analyze the biophysical mechanisms of the underlying auditory signal transduction process causing variability.

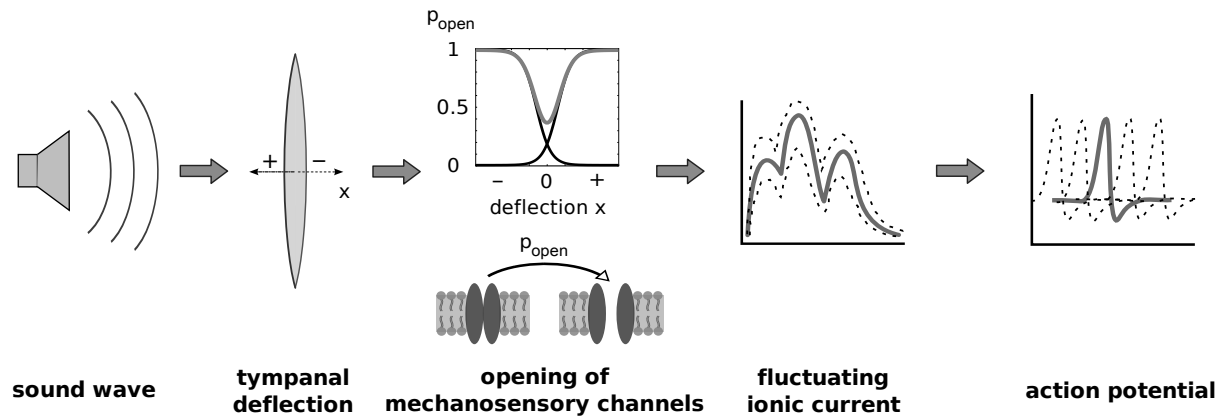


Figure 5.2: Auditory transduction cascade of locusts. Tympanal deflections induced by sound waves of different intensities cause mechanosensory ion channels in the membrane of auditory receptor neurons to open (schematically drawn). This mechanosensory transduction can be modeled as a quadratic nonlinearity (Gollisch and Herz, 2005) which we model in this thesis as the sum of two Boltzmann functions that describe the open probabilities (p_{open}) of the mechanosensory ion channels. The resulting ionic currents activate voltage-dependent ion channels which trigger action potentials. Our hypothesis is that stochastic opening and closing of ion channels causes fluctuations of the mediated ionic currents eventually causing variability in spike timing.

Part II. MATERIAL & METHODS

Experimental approaches and theoretical analysis

Intracellular recordings from axons of locust auditory receptor cells

6.1 Electrophysiology

Intracellular recordings were performed from axons of auditory receptor neurons of adult *Locusta migratoria*. All experiments were done at room temperature (22–24 °C). After decapitation and removal of legs and wings, the abdomen's tip was cut to extract the gut. The ventral side of the animal was then glued to an animal holder using sticking wax. The upper part of the metathorax was removed and the torso was filled with locust saline (Pearson and Robertson, 1981). After exposing the metathoracic ganglion and the auditory nerve, the nerve was fixed with a custom-made forceps. The recordings were performed from the proximal fibers in the auditory nerve. We used standard glass microelectrodes (borosilicate; 1.5 mm outer diameter; World Precision Instruments, Sarasota FL, USA, and GB150F-8P, Science Products, Hofheim, Germany) pulled to a resistance of 30–80 M Ω (Model P-97, Sutter Instrument Co., Novato, CA, USA) and filled with a 1 M KCl solution. The signals from the auditory receptor cells were amplified (BRAMP-01 or SEC-05LX, npi electronic, Tamm, Germany) and recorded by a data acquisition board (PCI-6229, National Instruments, Austin TX, USA) with a sampling rate of 20 kHz. For online spike detection, data analysis, and the generation of acoustic stimuli we used the software *RELACS* (www.relacs.net) running on a Debian Linux computer. Acoustic stimuli transmitted by the acquisition board (sampling rate: 120 or 240 kHz) were sent to a custom-made attenuator (ATN-01M, npi electronic, Tamm, Germany) based on the Chrystal CS3310 attenuator chip (Cirrus logic, Austin, TX, USA) for adjusting the sound intensity, amplified (RKB-250, Rotel, North Reading, MA), and then forwarded to two loudspeakers (DSM 25 FFL-8, Visaton, Haan, Germany). The loudspeakers were positioned orthogonal to the locust body axis at a distance of 25 cm. For calibrating the sound intensity we used a 1/2" microphone (40AC on a 26AM preamplifier, G.R.A.S., Holte, Denmark) on a constant voltage amplifier (12AK,

G.R.A.S., Holte, Denmark). To reduce echoes, the experimental setup was lined with sound-attenuating foam.

6.2 Stimuli

For acoustic stimulation pure tones of different but constant sound intensities (measured in dB SPL, sound pressure level) were presented ipsilaterally to the recorded auditory neuron. The sound frequency was set to the characteristic frequency of the recorded receptor neuron (2-17 kHz). All stimuli started and ended with a 2 ms ramp. Short stimuli of 500 ms duration separated by gaps of 1 second were used for most of the analysis of the interspike-interval (ISI) statistics. Long stimulus durations of 1 min were used for measuring ISI correlations at spike frequencies below 50 Hz as well as for the analysis of spike-count variability. For the determination of the effective time constants of spike-frequency adaptation both types of stimuli were used (see section 6.3.3).

6.3 Data analysis

6.3.1 Interspike-interval statistics

For the analysis of the interspike-interval statistics, we used $N = 12$ recordings of auditory receptor cells of different animals with stimulus durations of 500 ms (recording duration > 20 min) and $N = 14$ recordings of different animals with stimulus durations of 1 min. Due to the firing rate transients induced by spike-frequency adaptation we disregarded the first 200 ms of each trial of 500 ms duration and the first 10 s of each trial evoked by a 1 min pure tone stimulus.

ISI variability was quantified by both the coefficient of variation $CV = \sqrt{\langle \Delta T^2 \rangle} / \langle T \rangle$ and the quantity $D_{rnwl} = \langle \Delta T^2 \rangle / (2 \langle T \rangle^3)$ where $\langle T \rangle$ is the mean and $\langle \Delta T^2 \rangle = \langle T^2 \rangle - \langle T \rangle^2$ the variance of the ISIs. D_{rnwl} corresponds to the diffusion coefficient of the spike count of the ISI shuffled spike train and will be referred in the following in short as the diffusion coefficient. For a perfect integrate-and-fire (PIF) model driven by white noise, D_{rnwl} is proportional to the noise intensity of the driving fluctuations, i.e. to the *input* noise intensity (e.g. Vilela and Lindner, 2009).

We also constructed ISI histograms and compared them with probability density functions of simple noise-driven neuron models. The ISI density of a perfect integrate-and-fire neuron with white noise driving (Gerstein and Mandelbrot, 1964) is given by

$$p_{wn}(T) = \frac{1}{\sqrt{4\pi D_{rnwl} T^3}} \exp \left[-\frac{(T - \langle T \rangle)^2}{4D_{rnwl} T \langle T \rangle^2} \right]. \quad (6.1)$$

This probability density is also known as the “inverse Gaussian”. The name was introduced by Tweedie (1947) who noted the inverse relationship between cumulant generating functions of this distribution and those of a Gaussian distribution. The inverse

Gaussian also approximates well the ISI density of a PIF neuron with a *deterministic* adaptation current and additive white Gaussian noise of intensity D_{rnwl} (Schwalger et al., 2010). In contrast, an approximation of the ISI density of an adapting PIF neuron with a *stochastic* adaptation current and no white noise driving is given by a probability density resulting from a PIF neuron driven by exponentially correlated colored noise (Ornstein-Uhlenbeck noise, Lindner, 2004):

$$p_{\text{cn}}(T) = \frac{1}{2\tilde{\tau}\sqrt{4\pi\epsilon\gamma_1^3}} \exp\left[-\frac{(T - \langle T \rangle)^2}{4\epsilon\tilde{\tau}^2\gamma_1}\right] \left\{ \frac{[(\langle T \rangle - T)\gamma_2 + 2\gamma_1\tilde{\tau}]^2}{2\gamma_1\tilde{\tau}^2} - \epsilon(\gamma_2^2 - 2\gamma_1e^{-T/\tilde{\tau}}) \right\} \quad (6.2)$$

with $\gamma_1(T) = T/\tilde{\tau} + e^{-T/\tilde{\tau}} - 1$, $\gamma_2(T) = 1 - e^{-T/\tilde{\tau}}$ and the correlation time $\tilde{\tau}$ which is proportional to the adaptation time constant τ . The parameter $\epsilon = \sigma^2/\mu^2$ is the variance of the noise rescaled by the square of the mean current μ of the PIF model. The squared coefficient of variation of the density, Eq. (6.2), is given by

$$C_V^2 = \frac{2}{\delta} \left[\epsilon \left(1 - \frac{1 - e^{-\delta}}{\delta} \right) + \epsilon^2 \left(e^{-\delta} + \frac{(1 - e^{-\delta})(1 - 2e^{-\delta})}{\delta} \right) \right] \quad (6.3)$$

with $\delta = \langle T \rangle / \tilde{\tau}$. Given the mean and variance of the ISIs, we can eliminate ϵ via Eq. (6.3) (the quadratic equation has only one positive solution in ϵ) and then fit $p_{\text{cn}}(T)$ to the ISI histograms (ISIH) by a least-square fit of the unknown correlation time constant $\tilde{\tau}$ using a simplex algorithm. To quantify the fit quality of p_{wn} and p_{cn} to the ISIH, we used the Kolmogorov-Smirnov (KS) test. This statistical test yields 1 if two probability densities are completely identical and 0 if they completely differ.

To quantify the shape of the ISI densities we used two measures introduced by Schwalger et al. (2010): rescaled versions of the skewness $\gamma_s = \langle T \rangle_3 / (\sqrt{\langle \Delta T^2 \rangle} \langle \Delta T^2 \rangle)$ and kurtosis $\gamma_e = \langle T \rangle_4 / \langle \Delta T^2 \rangle^2 - 3$ where $\langle T \rangle_3 = \langle (T - \langle T \rangle)^3 \rangle$ and $\langle T \rangle_4 = \langle (T - \langle T \rangle)^4 \rangle$ are the third and fourth moments about the mean ISI $\langle T \rangle$. These measures given by

$$\alpha_s = \frac{\gamma_s}{3C_V} \quad (6.4)$$

$$\alpha_e = \frac{\gamma_e}{15C_V^2} \quad (6.5)$$

are identical to one for the inverse Gaussian ISI density (Eq. (6.1)). Values larger than one indicate that the density is more skewed and peaked compared to $p_{\text{wn}}(T)$. This is the case for the colored noise distribution p_{cn} (Eq. (6.2)) with $\tilde{\tau} \gg 0$.

We quantified the correlations among succeeding ISIs ($k = 1$) by the serial correlation coefficient

$$\rho_k = \frac{\langle T_i T_{i+k} \rangle - \langle T_i \rangle^2}{\langle T_i^2 \rangle - \langle T_i \rangle^2}. \quad (6.6)$$

For the analysis of the spike train responses evoked by short acoustical stimuli of 500 ms, we calculated ρ_1 across all trials because the ISI statistics was too small to obtain reliable

values for each spike train trial separately. In the cases where we used a 1 min stimulus, we divided each trial in sections of 300 ISIs and calculated the mean serial correlation coefficient by averaging over all sections.

To test the significance of negative serial correlations we determined the distribution of correlations occurring by chance after shuffling the ISIs of each spike train section 2000 times. The measured serial correlation was considered significant if the integral over the shuffled distribution up to this value was smaller than 0.05 (Fig. 10.5 D).

6.3.2 Spike-count statistics

The Fano factor (Fano, 1947) is defined as the ratio of the variance and the mean of the spike count $N(t_c)$ for different non-overlapping counting time frames of length t_c :

$$F(t_c) = \frac{\langle \Delta N(t_c)^2 \rangle}{\langle N(t_c) \rangle}. \quad (6.7)$$

It gives us a measure for the spike-count variability. For small t_c , the Fano factor approaches $F(t_c) = 1$ (Teich et al., 1997). For large t_c , its steady-state F_∞ is related to the ISI correlations ρ_i of lag i and to the CV by (Cox and Lewis, 1966):

$$F_\infty = CV^2 \left(1 + 2 \sum_{i=0}^{\infty} \rho_i \right). \quad (6.8)$$

For a renewal process with uncorrelated ISIs the Fano factor for large t_c is given by $F_\infty = CV^2$. Negative ISI correlations give rise to a decreased spike-count variance compared to the one of a renewal process, $F_\infty < CV^2$, while positive serial correlations cause an increased count variance, $F_\infty > CV^2$.

For the PIF model with Ornstein-Uhlenbeck noise (Eq. (9.1)-(9.2)) which is known to cause positive ISI correlations (Schwalger et al., 2010), Middleton et al. (2003) extensively analyzed the Fano factor and derived analytic expressions for small and large counting times, F_{small} and F_{large} , as well as for the position of the Fano factor minimum t_c^{min} :

$$F_{small}(t_c) \approx \frac{v_{th}}{4\mu t_c} \quad (6.9)$$

$$F_{large}(t_c) = \frac{2D^{OU}\tau^{OU}}{v_{th}\mu} \left[1 - \frac{\tau^{OU}}{t_c} (1 - \exp^{-t_c/\tau^{OU}}) \right] \quad (6.10)$$

$$t_c^{min} \approx \frac{v_{th}}{2\sqrt{D^{OU}}} \quad (6.11)$$

where v_{th} is the spike threshold, μ is a constant input current and D^{OU} and τ^{OU} are the noise intensity and correlation time constant of the Ornstein-Uhlenbeck noise, respectively. The Fano factor for moderate counting times, i.e. $t_c < \tau^{OU}$, follows a power-law with exponent κ and is given by

$$F(t_c) \approx D^{OU} t_c^\kappa \quad (6.12)$$

where $\kappa = 1$ for the colored noise driven PIF model. For $F \rightarrow \infty$ (i.e. saturation) the Fano factor can be approximated by

$$F(t_c) \approx D^{OU} \tau^{OU}. \quad (6.13)$$

6.3.3 Effective time constants of adaptation

Short stimulus durations were used to calculate the effective time constants τ_{eff_A} of the fast adaptation currents. The effective time constants τ_{eff_B} of the slow adaptation currents were determined from recordings during stimulation with 1 min pure tones.

To determine τ_{eff_A} we used the recordings with 500 ms stimulus duration. From these types of recordings, we received many trials (20-380) of short spike trains for a given sound intensity where the mean spike frequency defined as the inverse interspike interval gives smooth curves with a clear onset frequency f_0 (see Fig. 12.2A). For recordings with 1 min stimulus duration the number of recorded spike trains is in the range of 1-6 trials. Here, we calculated the mean firing rate which is given by the mean number of spikes in a defined time window (see Fig. 12.2B). To eliminate the frequency decay resulting from the fast adaptation current we chose a time window of 100 ms. We fitted (least-square fit) a single exponential to both the mean spike frequency and firing rate of the following form:

$$f(t) = (f_0 - f_\infty) \exp^{-t/\tau_{eff}} + f_\infty \quad (6.14)$$

where f_0 and f_∞ are the onset and steady-state spike frequency, respectively.

Model of the locust auditory transduction cascade

A schematic drawing of a locust auditory transduction cascade is given in Fig. 10.6 A. Deflections of the tympanal membrane induced by a sound stimulus cause mechanosensory ion channels in the membrane of auditory receptor cells to open. The resulting ionic currents activate voltage-dependent ion channels triggering action potentials as well as additional currents mediating spike-frequency adaptation. We separated these processes in two parts: (i) the spike generating receptor neuron model with spike-frequency adaptation and (ii) the mechanosensory transduction cascade from the sound input to the activation of the mechanosensory currents driving the spike generator.

7.1 Spike generator with spike-frequency adaptation

For the simulation of the membrane potential dynamics and the generation of action potentials, we used the single-compartment conductance-based Traub & Miles model with spike-frequency adaptation modified by Ermentrout (1998). The membrane potential V (in mV) is described by

$$C_m \frac{dV}{dt} = -I_{Na} - I_K - I_L - I_A - I_B - I_R \quad (7.1)$$

where $C_m = 1 \mu\text{F}/\text{cm}^2$ and I_R is the driving current passing through the mechanosensory channels of an auditory receptor neuron (in $\mu\text{A}/\text{cm}^2$). The deterministic ionic currents responsible for the action potential generation are given by the following equations (Ermentrout, 1998):

Sodium current: $I_{Na} = \bar{g}_{Na} m^3 h (V - E_{Na}),$
 $\bar{g}_{Na} = \vartheta \cdot 100 \text{ mS}/\text{cm}^2, E_{Na} = +50 \text{ mV},$
 $dm/dt = \alpha_m(V)(1 - m) - \beta_m(V)m, dh/dt = \alpha_h(V)(1 - h) - \beta_h(V)h,$

$$\begin{aligned}\alpha_m(V) &= 0.32(V + 54)/(1 - \exp(-(V + 54)/4)), \\ \beta_m(V) &= 0.28(V + 27)/(\exp((V + 27)/5) - 1), \\ \alpha_h(V) &= 0.128 \exp(-(V + 50)/18), \\ \beta_h(V) &= 4/(1 + \exp(-(V + 27)/5)).\end{aligned}$$

Potassium current: $I_K = \bar{g}_K n^4 (V - E_K)$,

$$\begin{aligned}\bar{g}_K &= \vartheta \cdot 80 \text{ mS/cm}^2, E_K = -100 \text{ mV}, dn/dt = \alpha_n(V)(1 - n) - \beta_n(V)n, \\ \alpha_n(V) &= 0.032(V + 52)/(1 - \exp(-(V + 52)/5)), \\ \beta_n(V) &= 0.5 \exp(-(V + 57)/40).\end{aligned}$$

Leak current: $I_L = \bar{g}_L (V - E_L)$,

$$\bar{g}_L = \vartheta \cdot 0.1 \text{ mS/cm}^2, E_L = -67 \text{ mV}.$$

To yield a membrane time constant in the sub-millisecond range (Gollisch and Herz, 2005), the sodium, potassium and leak conductances were multiplied by $\vartheta = 20$. The membrane time constant for the model using $\bar{g}_L = 2 \text{ mS/cm}^2$ is then $\tau_m = C_m/\bar{g}_L = 0.5 \text{ ms}$. The driving current I_R described below was chosen to result in a steady-state firing rate at its saturation level of 180 Hz which is about 150 Hz smaller than the onset-state firing rate (Benda et al., 2001, see Fig. 10.1 B).

Spike-frequency adaptation on a fast time scale of a hundred milliseconds was mediated by a fast M-type adaptation current I_A , i.e. a slow voltage-dependent potassium current:

Fast M-type adaptation current: $I_A = \bar{g}_A w (V - E_A)$,

$$\begin{aligned}E_A &= -100 \text{ mV}, \tau_w(V)dw/dt = w_\infty(V) - w, \tau_w(V) = 100 \text{ ms}, \\ w_\infty(V) &= 1/(1 + \exp(-(V + 20)/5)).\end{aligned}$$

In the model with one adaptation current, the conductivity \bar{g}_A was set to 5.0 mS/cm^2 and the second adaptation current was set to $I_B = 0 \mu\text{A/cm}^2$. In the model with two adaptation currents \bar{g}_A was set to 3.0 mS/cm^2 .

In the model with two adaptation currents, the slow adaptation current I_B was either modeled as a voltage-dependent (M-type) current or a calcium-dependent (AHP) potassium current:

Slow voltage-dependent potassium current: $I_B = \bar{g}_M v (V - E_M)$,

$$\begin{aligned}\bar{g}_M &= 5.0 \text{ mS/cm}^2, E_M = -100 \text{ mV}, \\ \tau_v(V)dv/dt &= v_\infty(V) - v, \tau_v(V) = 9 \text{ s}, v_\infty(V) = 1/(1 + \exp(-(V + 20)/5)).\end{aligned}$$

Slow calcium-dependent potassium current: $I_B = \bar{g}_{AHP} q (V - E_{AHP})$,

$$\begin{aligned}\bar{g}_{AHP} &= 9.0 \text{ mS/cm}^2, E_{AHP} = -100 \text{ mV}, \\ q &= 0.057([Ca] - 0.5)/(1.0 - \exp(-([Ca] - 0.5)/0.1)), \\ \tau_{AHP}d[Ca]/dt &= -0.16I_{Ca} - [Ca], \tau_{AHP} = 9 \text{ s}\end{aligned}$$

The dynamics of the AHP current was adopted from Ermentrout (1998) with a modified activation function q .

7.2 Model of the mechanosensory transduction process

The activating input signal for the mechanosensory transduction process was a pure tone sound pressure wave $s(t)$ of amplitude A and frequency f : $s(t) = A \sin(2\pi ft)$. The sound frequency was set to $f = 4$ kHz, a typical characteristic frequency of low-frequency receptors of locusts (Michelsen, 1971). The amplitude A can be calculated from the sound intensity I by $A = 20 \mu\text{Pa} \cdot 10^{I/20}$ in dB SPL (sound pressure level). It was shown that the amplitude of the tympanal deflection depends linearly on the sound pressure for pure tones (Michelsen and Rohrseitz, 1995). Thus, the tympanal vibration $x(t)$ is proportional to the sound pressure wave: $x(t) = \tilde{c} \cdot s(t)$.

The cilia of the locust auditory receptor neurons are connected to the tympanum via attachment cells (Gray, 1960). Gollisch and Herz (2005) have shown that the transmitted signal during the transduction process between the mechanical vibration of the eardrum and the accumulation of electrical charge at the receptor cell membrane undergoes a squaring. Moreover, the spike frequency of spike train responses saturates at stimulus intensities about 20 dB above threshold intensity (Römer, 1976). This saturation is caused by the saturation of the mechano-electrical transduction process (Wolf and Benda, personal communication).

Based on this information, we assumed two populations of ion channels in the membrane of the mechanosensory receptor neurons that open either for positive or negative deflections of the eardrum and whose open probabilities follow a Boltzmann distribution. The sum of the two Boltzmann functions of both receptor channel populations comprises, thus, the quadratic nonlinearity at low and medium sound intensities and the saturation of firing rates:

$$g(x) = p_o^+(x) + p_o^-(x) \quad (7.2)$$

where $p_o^+(x)$ and $p_o^-(x)$ are the open probabilities for positive and negative tympanal displacements, respectively. Assuming the channel gating acting as a spring following Hooke's law, the steady-state open probabilities are given by

$$p_o^+(x) = \frac{1}{1 + \exp(-c(x - x_0))} \quad (7.3)$$

$$p_o^-(x) = \frac{1}{1 + \exp(c(x + x_0))} \quad (7.4)$$

with the single channel gating force c indicating the channel sensitivity to the tympanal deflections and x_0 being the displacement for which the channel open probability is 0.5 (Howard and Hudspeth, 1988; Hudspeth et al., 2000). The parameters \tilde{c} , c and x_0 influence both the dynamic range of the auditory receptor neuron model and the minimal open probability at the tympanal resting position. We chose $\tilde{c}c = 250 \mu\text{Pa}^{-1}$ and $x_0/\tilde{c} = 0.012 \mu\text{Pa}$ so that the resulting f-I curves are comparable to the ones observed in locust auditory receptor cells, in particular with a dynamic range that is about 20 dB wide and with a peak of the diffusion coefficient D_{rnwl} in the lower dynamic range (cf. Fig. 10.2).

In the models with deterministic receptor current mediated by an infinite population of receptor channels ($N_R \rightarrow \infty$), the time evolution of the open probability is given by

$$\tau_r \dot{p}^+ = -p^+ + p_o^+(x) \quad (7.5)$$

$$\tau_r \dot{p}^- = -p^- + p_o^-(x) \quad (7.6)$$

with the receptor channel time constant $\tau_r = 0.1$ ms if not otherwise stated. Here, the mean number of open receptor channels corresponds to $N_o = \frac{1}{2}N_R p^+ + \frac{1}{2}N_R p^-$ with N_R being the total number of channels of both receptor channel populations. Note that in this study the total number of simulated receptor channels is always declared as the sum of channel numbers of both channel populations whereas each population is composed of identical channel numbers. The receptor current I_R passing the fraction of open channels $W = N_o/N_R$ is determined by

$$I_R = \bar{g}_R W (V - E_R) \quad (7.7)$$

where \bar{g}_R denotes the maximal conductivity and E_R constitutes the reversal potential of the receptor current. We assumed $E_R = 0$ mV so that the reversal potential is much higher than the neuron's resting potential.

In the stochastic models, the receptor channel gating was simulated using Gillespie's algorithm (see below). The transition rates α_r and β_r defined in the Markov scheme 7.9 are given by:

$$\alpha_r^{+/-} = \frac{p_o^{+/-}(x)}{\tau_r} \quad \beta_r^{+/-} = \frac{1 - p_o^{+/-}(x)}{\tau_r}. \quad (7.8)$$

According to the deterministic models, the current passing the receptor channels is defined by the fraction of open channels W as defined in Eq. (7.7).

In the models with one adaptation current the maximal receptor channel conductivity of $\bar{g}_R = 0.6$ mS/cm² was chosen for both the deterministic and stochastic receptor channels. In the models with two adaptation currents \bar{g}_R was set to 0.4 mS/cm² to result in the same f-I curves as the experimental data.

7.3 Kinetic schemes for the stochastic ion channel models

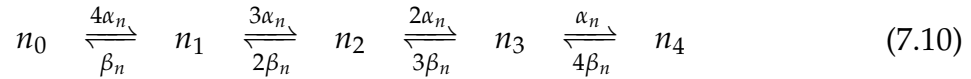
For the spike generating model, we employed diverse stochastic models. In the first model type, one type of ion channel was simulated as a finite population of N channels mediating a stochastic current while the remaining channel types corresponded to infinite channel populations mediating deterministic ionic currents. The second type of stochastic model only differed in the fact that we have a mixture of two ion channel populations: One finite population of fast ion channels and one finite population of slow adaptation channels working on a time scale of a hundred milliseconds. The third type is an expansion of the second model type where we included a second adaptation current working on a time scale of several seconds.

Stochastic ion channels can be modeled as Markov processes (Neher and Stevens, 1977). Assuming the channels carrying the receptor current being simple ion channels consisting of the two states closed and open, the kinetic scheme can be drawn as



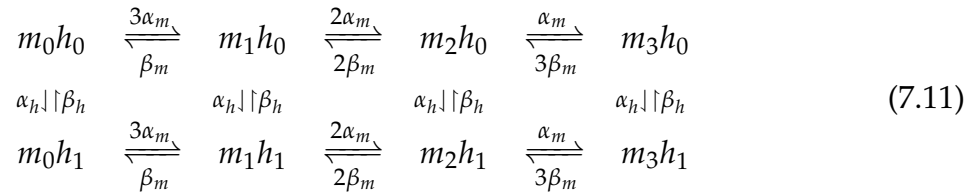
where α_r and β_r define the rates (transition probability per unit time) from r_0 to r_1 and vice versa. According to the Markov assumption the probability of an arbitrary transition depends only on the state in which the system is and can thus be defined by $p_\infty = \alpha_r / (\alpha_r + \beta_r)$. The time which is required to perform a state transition is $\tau_r = 1 / (\alpha_r + \beta_r)$.

Assuming a simple Markov process for the potassium channel composed of four identical gates n with an opening transition rate α_n and a closing transition rate of β_n , the potassium channel kinetic scheme can be written as



where n_4 corresponds to the open state where all four channel gates are open (Neher and Stevens, 1977). The stochastic potassium current passing a fraction of open channels is then given by $I_K = \bar{g}_K (N_K^o / N_K) (V - E_K)$.

The Markov kinetic scheme for a sodium channel with three activating gates m and one inactivating gate h is expressed by



where $m_3 h_1$ defines the open state where the three activating gates m and the inactivating gate h are open (Neher and Stevens, 1977). The stochastic sodium current passing a fraction of open channels is given by $I_{Na} = \bar{g}_{Na} (N_{Na}^o / N_{Na}) (V - E_{Na})$.

For the channels carrying the voltage-dependent adaptation current we assumed just as for the receptor channels a simple two state channel model:



where $\alpha_w = w_\infty / \tau_w$ is the opening and $\beta_w = (1 - w_\infty) / \tau_w$ the closing transition rate and where w_1 defines the open state. Fast voltage-dependent adaptation channels were modeled with a time constant $\tau_w = 0.1$ s, while the slow ones were modeled with $\tau_w = \tau_v = 9$ s. The stochastic voltage-dependent adaptation currents passing a fraction of open channels were given by $I_A = \bar{g}_A (N_A^o / N_A) (V - E_A)$ and $I_B = \bar{g}_M (N_B^o / N_B) (V - E_M)$.

In the model with one fast voltage-dependent and one slow calcium-dependent potassium current, we modeled the stochastic calcium dynamics by $d[Ca]/dt = \frac{-0.16I_{Ca} - [Ca]}{\tau_{AHP}} + \sqrt{\frac{2D_{Ca}}{\tau_{AHP}}} \zeta(t)$ where D_{Ca} is the intensity of the Ornstein-Uhlenbeck noise where the adaptation current was given by $I_B = \bar{g}_{AHP}(N_B^o/N_B)(V - E_{AHP})$.

7.4 Simulation of stochastic opening ion channels

The gating of the stochastic opening channels was simulated using Gillespie's stochastic integration algorithm modified for multiple ion channel populations and channels with multiple states (Gillespie, 1976; Gibson and Bruck, 2000). In short, the algorithm calculates the time interval until the next state transition, determines the reaction type, i.e. which one of the possible state transitions $A \rightarrow B$ occurs, and updates the number of channels in each possible state accordingly. Using the kinetic schemes defined in section 7.3 and the model parameters of section 7.1 and 7.2 the stochastic ion channel opening can be simulated by the following steps:

1. Specify the initial value of the number of open ion channels N_{iy}^o and closed channels N_{iy}^c in state y for each of the $i = 1, \dots, k$ ion channel populations where N_{iy} denotes the total channel number of population i in state y .
2. Define a state transition rate vector $\eta \in [\eta_{11}, \dots, \eta_{ij}, \dots, \eta_{kl}]$ with η_{ij} being the product of the channel number N_{iy} of ion channel population $i = 1, \dots, k$ in state y and the transition rate γ_j of the j th reaction with $j = 1, \dots, l$. Thus, each element of the transition vector is defined as $\eta_{ij} = N_{iy} \gamma_j$.
3. Construct a vector $\zeta \in [\zeta_{11}, \dots, \zeta_{iy}, \dots, \zeta_{kz}]$ of the sum of transition rates associated with escapes from all possible states $y = 1, \dots, z$.
4. Calculate the effective rate constant of the next state transition: $\lambda = \sum_{i=1}^k \sum_{y=1}^z N_{iy} \zeta_{iy}$.
5. Draw a random number u_1 that is uniformly distributed $[0,1)$ and compute the time of the next state transition $\Delta t = -\ln(u_1)/\lambda$.
6. If $\Delta t > t_{max}$ with $t_{max} = 1\mu s$, set $\Delta t = t_{max}$ and go back to step 3. Otherwise increment time t by Δt .
7. Draw a second random number u_2 that is uniformly distributed $[0,1)$ and determine which reaction (i, j) with state transition rate η_{ij} will occur by finding the smallest r and s such that $u_2 \lambda < \sum_{i=1}^k \sum_{j=1}^l \eta_{ij}$.
8. Perform the reaction $(i = r, j = s)$ and update N_{iy} .
9. Go back to step 3 and repeat loop.

Effect of spike-frequency adaptation on the interspike-interval statistics

8.1 Hodgkin-Huxley-type model with adaptation

To analyze the effect of adaptation on the interspike-interval statistics, we simulated the conductance-based Traub & Miles model modified by Ermentrout et al. (2001). It is a single-compartment model with an additional M-type current, i.e. a slow voltage-dependent potassium current, inducing spike-frequency adaptation. In order to contrast the effects of deterministic versus stochastic adaptation on the firing statistics of the conductance-based model, we simulated two versions with either additive white Gaussian noise or adaptation channel noise. For the first model with fast fluctuating current noise and deterministic adaptation, the membrane potential V measured in mV is determined by

$$C_m \frac{dV}{dt} = -I_{\text{Na}} - I_{\text{K}} - I_{\text{L}} - I_{\text{M}} + I + \sqrt{2D}\xi(t), \quad (8.1)$$

where $C_m = 1 \mu\text{F}/\text{cm}^2$ denotes the membrane capacitance, I is the base current, and D indicates the intensity of Gaussian white noise with correlation function $\langle \xi(t)\xi(t') \rangle = \delta(t - t')$. The deterministic ionic currents are given by the following equations (Ermentrout et al., 2001):

Sodium current: $I_{\text{Na}} = \bar{g}_{\text{Na}} m^3 h (V - E_{\text{Na}})$

$$\bar{g}_{\text{Na}} = 100 \text{ mS}/\text{cm}^2, E_{\text{Na}} = +50 \text{ mV},$$

$$dm/dt = \alpha_m(V)(1 - m) - \beta_m(V)m, dh/dt = \alpha_h(V)(1 - h) - \beta_h(V)h,$$

$$\alpha_m(V) = 0.32(V + 54)/(1 - \exp(-(V + 54)/4)),$$

$$\beta_m(V) = 0.28(V + 27)/(\exp((V + 27)/5) - 1),$$

$$\alpha_h(V) = 0.128 \exp(-(V + 50)/18), \beta_h(V) = 4/(1 + \exp(-(V + 27)/5)).$$

Potassium current: $I_{\text{K}} = \bar{g}_{\text{K}} n^4 (V - E_{\text{K}})$

$$\bar{g}_{\text{K}} = 80 \text{ mS}/\text{cm}^2, E_{\text{K}} = -100 \text{ mV}, dn/dt = \alpha_n(V)(1 - n) - \beta_n(V)n,$$

$$\alpha_n(V) = 0.032(V + 52)/(1 - \exp(-(V + 52)/5)),$$

$$\beta_n(V) = 0.5 \exp(-(V + 57)/40).$$

Leak current: $I_L = \bar{g}_L(V - E_L)$
 $\bar{g}_L = 0.2 \text{ mS/cm}^2, E_L = -67 \text{ mV}.$

M-type adaptation current: $I_M = \bar{g}_M w(V - E_M)$
 $\bar{g}_M = 1.15 \text{ mS/cm}^2, E_M = -100 \text{ mV}, dw/dt = (w_\infty(V) - w)/t_w(V),$
 $t_w(V) = 11.4 \tau_w / (3.3 \exp((V + 35)/20) + \exp(-(V + 35)/20)), \tau_w = 100 \text{ ms},$
 $w_\infty(V) = 1/(1 + \exp(-(V + 35)/10)).$

In this model, the adaptation time constant $t_w(V)$ is a voltage-dependent function that we reparametrized such that τ_w roughly corresponds to the time constant governing the exponential buildup of w during periodic firing at 100 Hz in a simulation of equation (8.1) without the I_M current and with $D = 0$.

For the second model with adaptation channel noise, the voltage is described by

$$C_m \frac{dV}{dt} = -I_{Na} - I_K - I_L - I_M^s + I. \quad (8.2)$$

The currents I_{Na} , I_K and I_L are the same as in the first model. The M-type adaptation current, however, is modeled as a stochastic current $I_M^s = \bar{g}_M W(V - E_M)$ where $W = N_{op}/N_a$ indicates the fraction of open channels. We assumed the adaptation channels to be two-state ion channels with the transition rates $\alpha_w(V) = w_\infty(V)/t_w(V)$ and $\beta_w(V) = (1 - w_\infty(V))/t_w(V)$. The gating of the adaptation channels was simulated using the Gillespie algorithm (see section 7.4).

In the model with stochastic adaptation current, the maximal channel conductance \bar{g}_M and the constant base current ($I = 18 \text{ } \mu\text{A/cm}^2$) were chosen to result in a CV ≈ 0.6 and a firing rate of 100 Hz for a simulation of $N_a = 100$ ion channels carrying the adaptation current. For the simulation with a deterministic adaptation current and additive white noise the base current was adjusted to yield the same rate $r = 100 \text{ Hz}$ while keeping the conductance \bar{g}_M the same. For $D = 0$ the base current I was $18 \text{ } \mu\text{A/cm}^2$. With increasing noise intensity I decreased to $I = 4 \text{ } \mu\text{A/cm}^2$ for $D = 200$. The units of the noise intensities are $(\mu\text{A/cm}^2)^2/\text{ms}$, the ones of the ionic currents are given by $\mu\text{A/cm}^2$.

Effect of spike-frequency adaptation on the spike-count statistics

9.1 Perfect integrate-and-fire model with Ornstein-Uhlenbeck noise or stochastic adaptation currents

Perfect integrate-and-fire (PIF) models represent minimal models of spike activity (Gerstein and Mandelbrot, 1964) following a simple fire-and-reset rule. Once a threshold v_{th} is crossed, a spike is elicited and the voltage v is reset to v_{reset} ($v_{reset} < v$). Using such simple models, Schwalger et al. (2010) have shown that a stochastic adaptation current can be effectively described by an exponentially correlated colored Gaussian noise, i.e. an Ornstein-Uhlenbeck (OU) process (cf. section 11.1). To analyze the effect of adaptation on the spike-count variability, we therefore used PIF models with one and two OU noise sources that we contrasted with PIF models with stochastic adaptation currents.

The dynamics of the membrane potential v of a PIF model with a single OU noise source (Middleton et al., 2003; Lindner, 2004) are described by

$$\dot{v} = \mu + w_A(t) \quad (9.1)$$

$$\dot{w}_A = -\frac{w_A(t)}{\tau_A^{OU}} + \sqrt{\frac{2D_A^{OU}}{\tau_A^{OU}}} \zeta(t) \quad (9.2)$$

where μ is a constant input current and where $\tau_A^{OU} = 0.1$ s and D_A^{OU} are the correlation-time constant and noise intensity of the OU process with correlation function $\langle \zeta(t)\zeta(t') \rangle = \delta(t - t')$, respectively.

The dynamics of a PIF model with two OU processes is analogously described by

$$\dot{v} = \mu + w_A(t) + w_B(t) \quad (9.3)$$

$$\dot{w}_A = -\frac{w_A(t)}{\tau_A^{OU}} + \sqrt{\frac{2D_A^{OU}}{\tau_A^{OU}}} \zeta(t) \quad (9.4)$$

$$\dot{w}_B = -\frac{w_B(t)}{\tau_B^{OU}} + \sqrt{\frac{2D_B^{OU}}{\tau_B^{OU}}} \zeta(t) \quad (9.5)$$

with a second noise source characterized by the correlation-time constant $\tau_B^{OU} = 1$ s and noise intensity D_B^{OU} . We contrasted these two models constituting OU noise with perfect integrate-and-fire models with stochastic adaptation currents.

Accordingly, we regarded PIF models with one and two stochastic adaptation currents. The dynamics of the former one is given by

$$\dot{v} = \mu - \alpha w_A(t) \quad (9.6)$$

$$\dot{w}_A = -\frac{w_A(t)}{\tau_A} + \sqrt{\frac{2D_A}{\tau_A}} \zeta(t) \quad (9.7)$$

where α denotes the adaptation strength, $\tau_A = 0.1$ s the adaptation time constant and D_A the noise intensity of the stochastic adaptation current. To achieve spike-frequency adaptation, the fire-and-reset rule was extended so that the adaptation variable w_A is incremented by $\Delta w_A = 0.005$ at each spiking event: if $(v \geq v_{th}) v \rightarrow 0, w_A \rightarrow w + \Delta w_A$.

Analogously to the PIF with a single adaptation current the model with two adaptation currents is described by

$$\dot{v} = \mu - \alpha w_A(t) - \beta w_B(t) \quad (9.8)$$

$$\dot{w}_A = -\frac{w_A(t)}{\tau_A} + \sqrt{\frac{2D_A}{\tau_A}} \zeta(t) \quad (9.9)$$

$$\dot{w}_B = -\frac{w_B(t)}{\tau_B} + \sqrt{\frac{2D_B}{\tau_B}} \zeta(t) \quad (9.10)$$

with a second adaptation current decaying with the time constant $\tau_B = 1$ s, with an adaptation strength β , and with the adaptation noise intensity D_B . The fire-and-reset rule for this model is given by: if $(v \geq v_{th}) v \rightarrow 0, w_A \rightarrow w_A + \Delta w_A, w_B \rightarrow w_B + \Delta w_B$ with $\Delta w_A = 0.005$ and $\Delta w_B = 0.05$.

Moreover, we analyzed the effect of a combination of deterministic and stochastic adaptation currents on the spike-count variability. For simulations with a fast deterministic adaptation current, we set $D_A = 0$. For models with slow deterministic adaptation, we set $D_B = 0$. The units of the noise intensities are v_{th}^2/ms . In all models, we used $v_{th} = 1, v_{reset} = 0$, and μ was chosen to result in a firing rate of 100 Hz.

9.2 Hodgkin-Huxley-type model with two adaptation currents

For the simulation of a conductance-based model with two adaptation currents we used the single-compartment Traub & Miles model modified by Ermentrout (1998). This model includes a M-type current, i.e. a slow voltage-dependent potassium channel, mediating spike-frequency adaptation. Since many neurons show spike-frequency adaptation on multiple time scales (French, 1987, 1989; Xu et al., 1996; Nelson et al., 1997; Fairhall et al., 2001a,b; Baccus and Meister, 2002; Ulanovsky et al., 2004; Wimmer et al., 2008), we here extended the model by a second voltage-dependent potassium current. The membrane potential V of this modified model is described by

$$C_m \dot{V} = -I_{Na} - I_K - I_L - I_A - I_B - I \quad (9.11)$$

where $C_m = 1 \mu\text{F}/\text{cm}^2$ and I is the driving current (in $\mu\text{A}/\text{cm}^2$) which was chosen to result in a steady-state spike frequency of 100 Hz. The deterministic ionic currents are given by the following equations (Ermentrout, 1998):

Sodium current: $I_{Na} = \bar{g}_{Na} m^3 h (V - E_{Na})$,

$$\bar{g}_{Na} = 100 \text{ mS}/\text{cm}^2, E_{Na} = +50 \text{ mV},$$

$$\dot{m} = \alpha_m(V)(1 - m) - \beta_m(V)m, \dot{h} = \alpha_h(V)(1 - h) - \beta_h(V)h,$$

$$\alpha_m(V) = 0.32(V + 54) / (1 - \exp(-(V + 54)/4)),$$

$$\beta_m(V) = 0.28(V + 27) / (\exp((V + 27)/5) - 1),$$

$$\alpha_h(V) = 0.128 \exp(-(V + 50)/18), \beta_h(V) = 4 / (1 + \exp(-(V + 27)/5)).$$

Potassium current: $I_K = \bar{g}_K n^4 (V - E_K)$,

$$\bar{g}_K = 80 \text{ mS}/\text{cm}^2, E_K = -100 \text{ mV},$$

$$\dot{n} = \alpha_n(V)(1 - n) - \beta_n(V)n,$$

$$\alpha_n(V) = 0.032(V + 52) / (1 - \exp(-(V + 52)/5)), \beta_n(V) = 0.5 \exp(-(V + 57)/40).$$

Leak current: $I_L = \bar{g}_L (V - E_L)$,

$$\bar{g}_L = 0.1 \text{ mS}/\text{cm}^2, E_L = -67 \text{ mV}.$$

The two currents mediating spike-frequency adaptation were simulated by

Fast voltage-dependent adaptation currents: $I_A = \bar{g}_A (w_A + \eta_A)(V - E_M)$,

$$\tau_A \dot{w}_A = -w_A + w_\infty$$

$$\tau_A \dot{\eta}_A = -\eta_A + \sqrt{2D_A} \zeta(t),$$

$$\tau_A = 100 \text{ ms}$$

Slow voltage-dependent adaptation currents: $I_B = \bar{g}_B (w_B + \eta_B)(V - E_M)$,

$$\tau_B \dot{w}_B = -w_B + w_\infty$$

$$\tau_B \dot{\eta}_B = -\eta_B + \sqrt{2D_B} \zeta(t)$$

$$\tau_B = 1000 \text{ ms}.$$

with $E_M = -100\text{mV}$ and $w_\infty = 1/(1 + \exp(-(V + 20)/0.05))$. The conductances \bar{g}_A and \bar{g}_B (in mS/cm^2) were set as indicated in the text. The adaptation currents were simulated both as deterministic ($D_A = 0$ or $D_B = 0$) and as stochastic currents ($D_A > 0$ or $D_B > 0$). The units of the noise intensities are $(\mu\text{A}/\text{cm}^2)^2/\text{ms}$, units of the ionic currents are given by $\mu\text{A}/\text{cm}^2$.

Part III. RESULTS

Interspike-interval and spike-count statistics

What are the sources of spike-response variability?

The variability of neuronal activity in response to repeated presentations of the same stimulus is a common feature of sensory systems (Berry et al., 1997; de Ruyter van Steveninck et al., 1997; Warzecha and Egelhaaf, 1999). This response variability has a profound impact on subsequent sensory signal processing (Kara et al., 2000; Vogel et al., 2005) and sets limits on the reliability of behavioral responses to external stimuli (Tolhurst et al., 1983; Britten et al., 1996). Several noise sources arising at different levels of a neuronal pathway cause this response variability (Faisal et al., 2008), e.g. sensory noise by noisy external stimuli which are amplified during the transduction process (Lillywhite and Laughlin, 1979; Laughlin and Lillywhite, 1982; Grewe et al., 2003), synaptic noise resulting from the bombardment of a myriad of synapses (Calvin and Stevens, 1967; Hessler et al., 1993), as well as electrical noise by stochastic gating of ion channels (“channel noise”, Neher and Stevens, 1977; Chow and White, 1996; White et al., 2000).

Already at the first stages of sensory pathways spike-timing variability emerges, as for example in retinal ganglion cells (Levine and Shefner, 1977; Levine, 2007), olfactory receptor neurons (Rospars et al., 1994; Duchamp-Viret et al., 2005), electroreceptor afferents (Kreiman et al., 2000), as well as auditory receptor neurons of insects (Ronacher et al., 2004; Schaette et al., 2005) and auditory nerve fibers of vertebrates (Teich and Khanna, 1985; Avissar et al., 2007). To characterize intrinsic stochastic properties of a neuron directly, somatic or even dendritic recordings are necessary (Sigworth, 1980; Neher and Stevens, 1977). In receptor neurons, however, such recordings are usually difficult to achieve without severely damaging the sensory transduction machinery.

In this study we investigate spike-timing variability and potential noise sources in auditory receptor neurons of *Locusta migratoria*. Although these neurons respond in a quite variable manner to pure tones with constant amplitude (Schaette et al., 2005), they transmit natural grasshopper songs as well as band-pass filtered white noise stimuli remarkably well (Machens et al., 2001, 2005) based on precise spike-timing (Rokem et al.,

2006). The locust auditory receptor cells are bipolar neurons that are directly attached to the tympanal membrane (Gray, 1960). The underlying mechanosensory transduction process is well understood in terms of a cascade of linear filters and static nonlinearities (Gollisch et al., 2002; Gollisch and Herz, 2005). Furthermore, these neurons exhibit both input and output-driven spike-frequency adaptation (Römer, 1976; Benda et al., 2001; Gollisch and Herz, 2004).

To uncover the primary noise sources in locust auditory receptor cells, we first quantified the variability of interspike intervals (ISIs) and analyzed their statistics, i.e. ISI distributions and correlations, during acoustic stimulation with pure tones of various but fixed intensities. Secondly, we employed models of the locust auditory transduction cascade in which the neuronal dynamics were affected by different channel noise sources. In particular, we focused on channel noise resulting from stochastic gating of the channels in the membrane of the receptor cells as well as on ion channels whose activation is strongly correlated to sound intensity, like the ones carrying the adaptation current and channels that play a significant role in spike generation.

10.1 Spike-response variability in locust auditory receptor neurons

Stimulation of locust auditory receptor neurons with 500 ms pure tones of constant intensity evokes a mean spike-frequency response which adapts over time (Römer, 1976; Benda et al., 2001, Fig. 10.1 A,B bottom). The initial high spike frequency directly after the onset of the acoustic stimulus declines over a duration of several ten to hundred milliseconds to its steady-state value. A sufficiently long interval of silence between the acoustic stimuli assures that the cell completely recovers from adaptation between successive stimuli.

The steady-state spike frequency computed from the final 300 ms of the response increases in a sigmoidal fashion with sound intensity and saturates at frequencies around 160 to 200 Hz (Fig. 10.2 A,B). Although the sensitivity, i.e. the minimal sound intensity required to evoke a response, varies considerably between receptor neurons, the overall shape of the f - I curves (steady-state spike-frequency versus sound intensity) is similar (Fig. 10.2 B).

The spike trains evoked by the tones with constant sound intensity show notable spike-time variability (Schaette et al., 2005, Fig. 10.1 A,B top) that is most prominent at low spike frequencies (Fig. 10.1 A top). The corresponding ISI histograms are broad at low sound intensities evoking low spike frequencies and get much narrower at higher sound intensities and the resulting higher spike frequencies (Fig. 10.1 C–E).

To quantify the dependence of the ISI variability on sound intensity, we computed both the coefficient of variation, CV , as well as the diffusion coefficient, D_{rnwl} . The CV s start out with values up to 0.9 for sound intensities at the lower end of the dynamic range (Fig. 10.2 C,D) where spike frequencies are below 50 Hz (see Fig. 10.2 B for comparison).

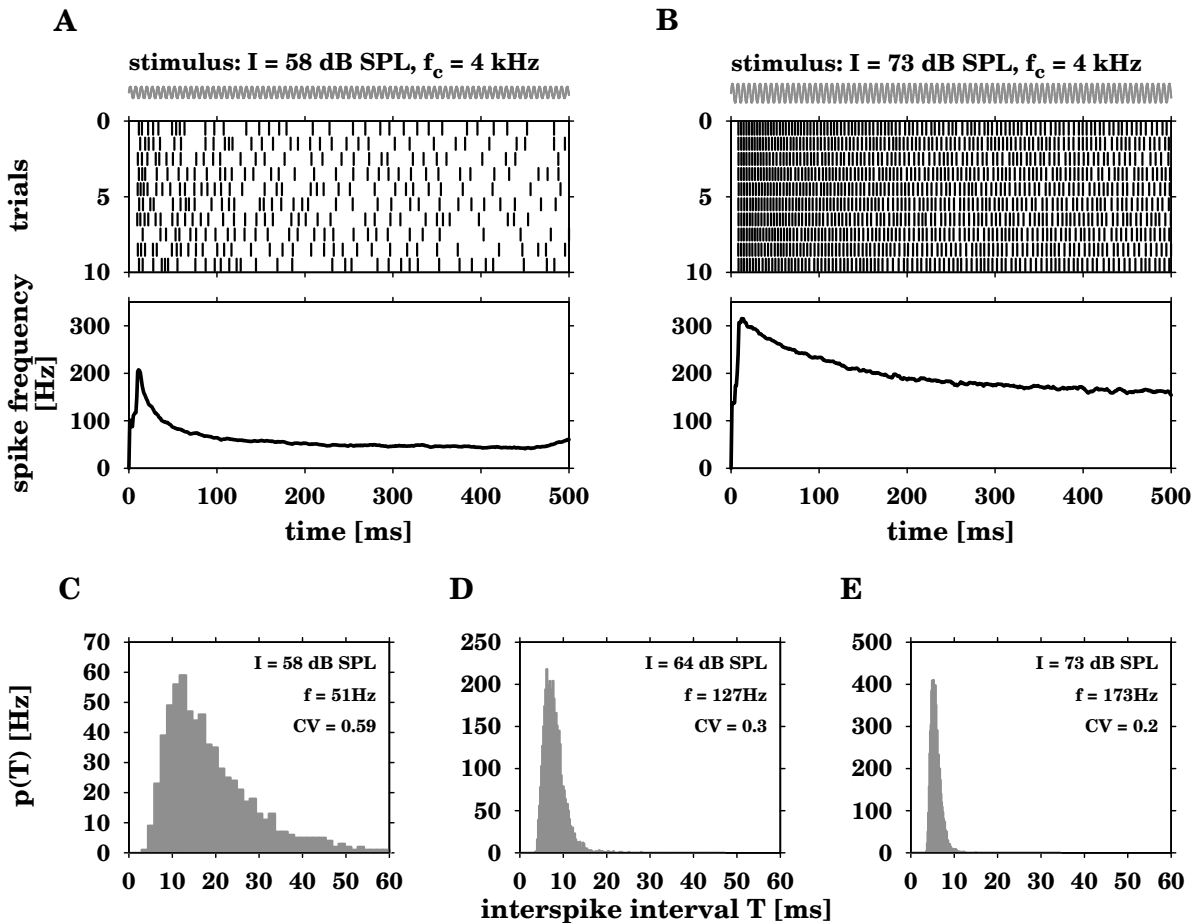


Figure 10.1: Interspike-interval variability in auditory receptor neurons. **A,B** The first 10 of 131 (A) and 206 (B) spike trains of an auditory receptor neuron evoked by stimulation with a 4 kHz (cell's best frequency) pure tone (schematically drawn as a slow sine wave) of 58 dB SPL (A) and 73 dB SPL (B), respectively (*top*). The interspike intervals (ISIs) within and across trials show high variability. The resulting spike frequency depends on sound intensity and shows spike-frequency adaptation (*bottom*). **C–E:** ISI histograms of the same cell obtained for different sound intensities I . The histograms in C and E were computed from the spike trains shown in A and B, respectively. The ISI variability is highest for sound intensities resulting in low spike frequencies (f).

With increasing sound intensity the CVs monotonically decline and saturate to low values around 0.1–0.2. The maximum in the CV-versus-relative sound intensity curves visible in a few cells and in the average of 12 cells is not significant (large error bars) because of the low number of available ISIs at these low spike frequencies. The diffusion coefficient D_{rnwl} , in contrast, shows a pronounced peak at the lower end of the receptor cells' dynamic range (Fig. 10.2 E,F). The peak height of D_{rnwl} varies from cell to cell (Mean: 9.36 Hz \pm 4.87 Hz s.d.) while the overall shape of D_{rnwl} is similar (Fig. 10.2 F).

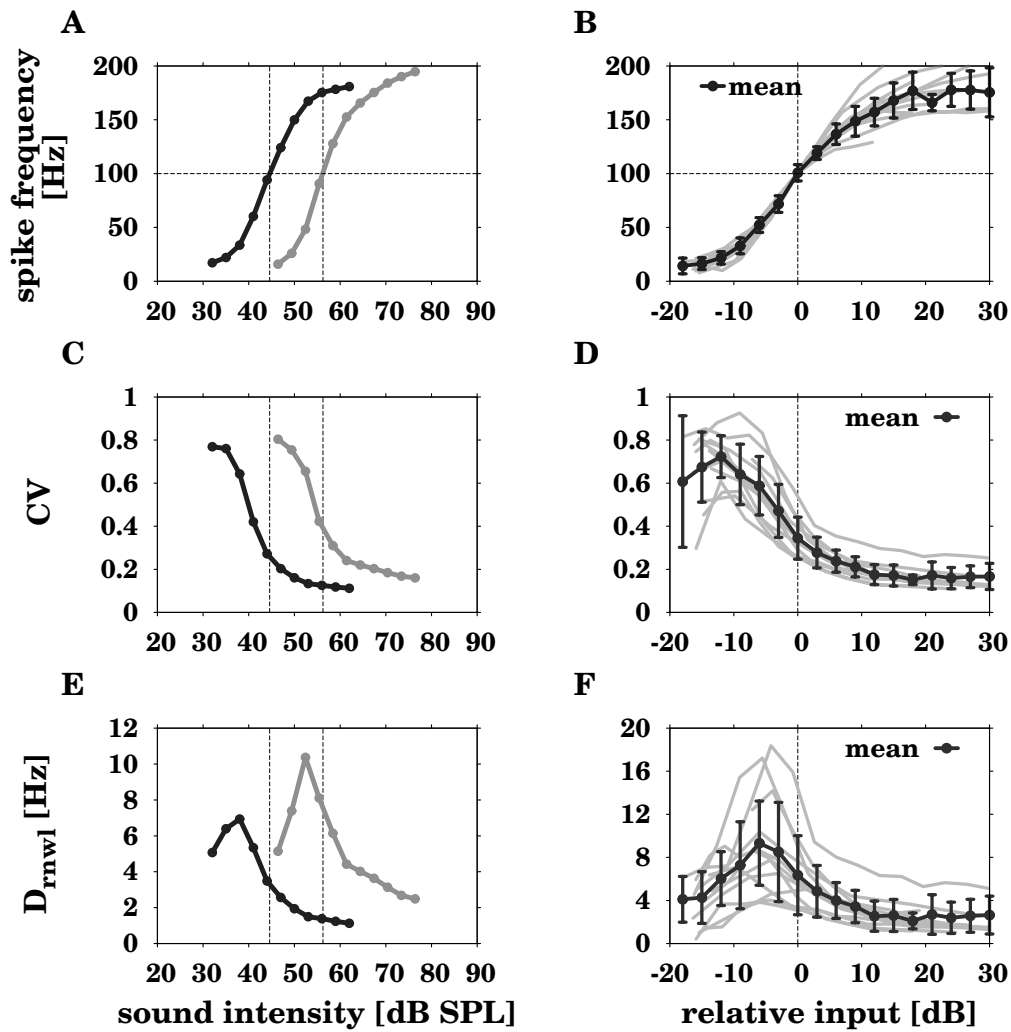


Figure 10.2: Response characteristics of auditory receptor neurons. **A** The rate-level functions (steady-state $f-I$ curve) of two different auditory receptor neurons have a similar sigmoidal shape, but differ in their sensitivity. **B** Rate-level functions of 12 different cells (gray lines) including the ones shown in **A** shifted along the intensity axis such that they align at a spike frequency of 100 Hz. The black line is the average \pm s.d. over all cells. **C** Coefficient of variation (CV) as a function of sound intensity for the two cells shown in **A** and **D** aligned for 12 neurons (as in **B**). The CVs monotonically decrease over the cell's dynamic range. **E** D_{rnwl} as a function of sound intensity for the two cells shown in **A** and **F** aligned (as in **B**). The curves show a pronounced peak in the lower part of the cells' dynamic range.

10.1.1 Interspike-interval distributions

What is the origin of the spike-timing variability? To answer this question, we first compared the observed ISI statistics with the ones known from canonical noise-driven neuron models.

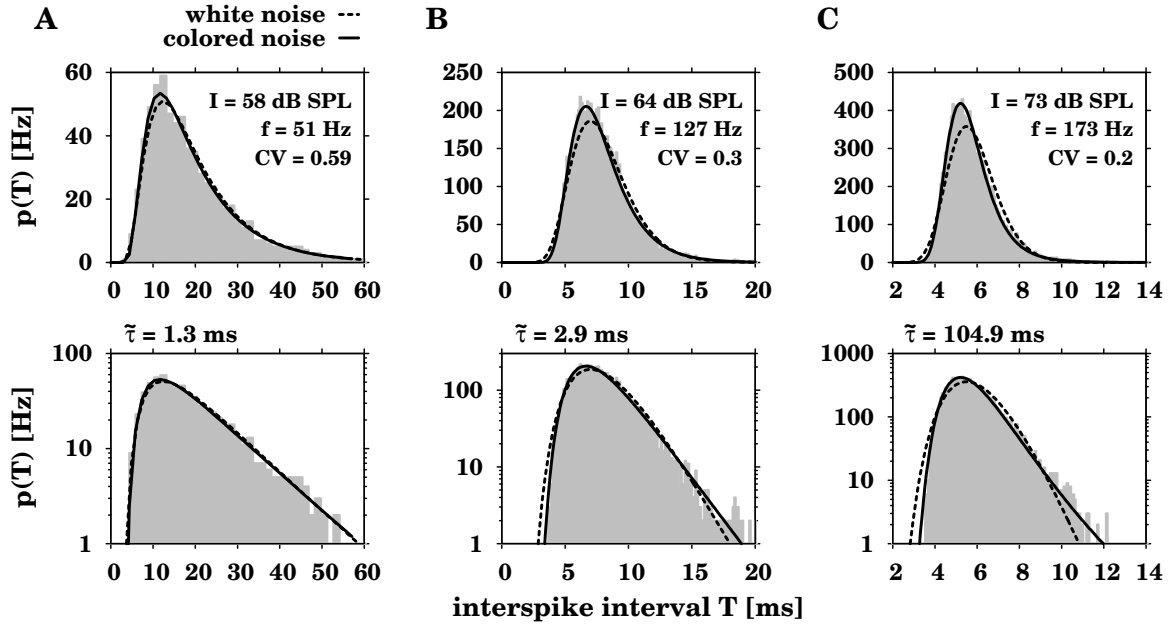


Figure 10.3: Comparison of interspike-interval histograms with the colored- and white-noise ISI distributions. Interspike-interval histograms (gray bars) computed from a recording of an auditory receptor neuron during stimulation with three different sound intensities I in comparison with the white-noise ISI density p_{wn} (dashed black line, Eq. (6.1)) and the colored-noise ISI distribution p_{cn} (solid black line, Eq. (6.2)). $\tilde{\tau}$ is the correlation time of the colored noise resulting from the fit of the colored-noise ISI distribution to the data. f : spike frequency, CV : coefficient of variation. The bottom row shows the same histograms on a logarithmic scale for emphasizing the tails. Note that the axes have different scales in A, B, and C.

Given the high firing rates and the non-exponential ISI histograms (ISIH) (Fig. 10.1 C–E), these neurons most likely operate in their super-threshold regime. The canonical model for this regime is the perfect integrate-and-fire (PIF) model. With additive white-noise driving (a signal with equal spectral power at all frequencies) the resulting ISI distribution is described by an “inverse Gaussian” density p_{wn} (Eq. (6.1), Gerstein and Mandelbrot, 1964), in the following referred to as white-noise density. With additional slow adaptation this still holds true although the parameters of the white-noise density are rescaled (Schwalger et al., 2010). Thus, we expect the ISI density p_{wn} to describe the measured ISI histograms, if the corresponding noise source is close to a white noise and if the noise is sufficiently weak.

Because the white-noise ISI density, Eq. (6.1), is a function solely of the mean and the standard deviation of the ISIs, it is completely determined by these two moments that can be directly computed from the experimentally measured spike responses. The resulting white-noise ISI density p_{wn} matches the ISIH of spike responses with low spike frequency (Fig. 10.3 A, dashed line). However, with increasing spike frequencies, p_{wn} no longer provides a good description of the data (Fig. 10.3 B,C, dashed line). The ISI histograms of the auditory receptor cells exhibit a more prominent peak and a heavier

tail in comparison to p_{wn} . Also the Kolmogorov-Smirnov test indicates that at higher spike frequencies the white-noise density p_{wn} is not a valid approximation (Fig. 10.4 A, gray line), although the null hypothesis that the densities are drawn from the same distribution could not be rejected.

Replacing the additive white noise of the PIF model by a colored noise, in particular an Ornstein-Uhlenbeck noise, results in a different ISI density p_{cn} (Eq. (6.2), Lindner, 2004). The colored-noise ISI density p_{cn} depends, in contrast to p_{wn} , additionally on the correlation time constant $\tilde{\tau}$ of the colored noise. We fitted p_{cn} to the ISI histograms of the recorded data, with $\tilde{\tau}$ being the only fit parameter. The resulting colored-noise ISI distributions describe the data remarkably well at both low and high spike frequencies (see Fig. 10.3, solid line, and KS-test, Fig. 10.4 A, black line). In the upper range of spike frequencies $\tilde{\tau}$ converges to the adaptation time constant, which is in the range of 100 ms in the locust auditory system (Fig. 10.3 C and Fig. 10.4 B). For lower spike frequencies $\tilde{\tau}$ decreases to values close to zero (Fig. 10.3 A and Fig. 10.4 B), that is the colored-noise ISI density in fact approaches the white-noise ISI density (Lindner, 2004).

Following Schwalger et al. (2010), we further quantified the transition from a white-noise ISI distribution to a colored-noise ISI distribution with non-zero correlation time by computing rescaled variants of the skewness (α_s , Eq. (6.4)) and kurtosis (α_e , Eq. (6.5)). These quantities assume unity for an inverse Gaussian distribution. Values larger than one indicate a more skewed distribution with a stronger peak and a heavier tail as is the case for the colored-noise ISI distribution. Indeed, at low spike frequencies, both α_s and α_e are close to one indicating a dominating white-noise source (Fig. 10.4 C). With increasing spike frequency both α_s and α_e monotonically increase to values larger than one further supporting our observation of a transition from an inverse Gaussian to the more peaked colored-noise distribution arising from a dominating colored-noise source.

The shapes of the ISI histograms thus suggest the presence of two different types of noise sources in the auditory receptor neurons of locusts: A white-noise source dominating at low spike-frequencies, and a colored-noise source, whose effect is more prominent at higher spike frequencies.

10.1.2 Interspike-interval correlations

Since the receptor neurons exhibit spike-frequency adaptation, we further investigated correlations between successive ISIs that may result from the interaction of the noise with the adaptation dynamics. In particular, we expect *negative* correlations for a deterministic adaptation process interacting with a white-noise input (Chacron et al., 2001; Liu and Wang, 2001; Schwalger et al., 2010) and *positive* correlations for colored noise arising from the stochasticity of an adaptation current itself (Lindner, 2004; Schwalger et al., 2010).

For spike-frequencies above about 50 Hz we found positive correlations between successive ISIs that monotonically increase with increasing spike frequency (Fig. 10.5 A, black line). The serial correlation coefficients at lag 1, ρ_1 , were obtained from the responses to the 500 ms stimuli as used before for investigating the ISI distributions. Especially at higher spike frequencies the responses are not stationary (see Fig. 10.1 B). Over the time

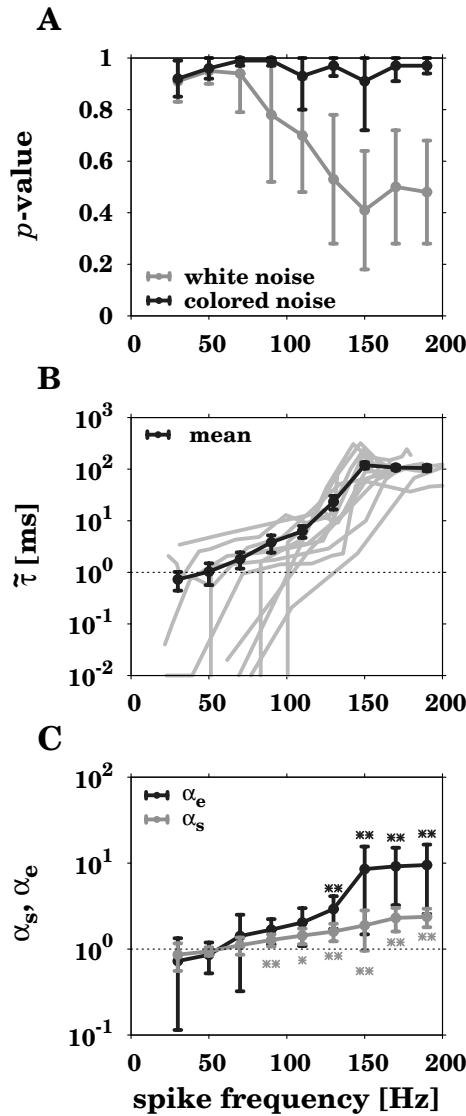


Figure 10.4: Shape of the interspike-interval histograms. Shown are data pooled from 12 auditory receptor cells as a function of spike frequency (stimulus duration: 500 ms) **A** The p -values for the null hypothesis that the ISI histograms as well as the colored-noise (black line, Eq. (6.2)) or white-noise ISI densities (gray line, Eq. (6.1)) are drawn from the same distribution (Kolmogorov-Smirnov test, mean \pm s.d.). **B** Correlation time constants $\tilde{\tau}$ determined by fitting the colored-noise ISI density to the data for each of the 12 recorded receptor neurons (gray lines) and the overall mean \pm s.e. (black line). **C** The mean \pm s.d. of the rescaled skewness (α_s , gray line, Eq. (6.4)) and kurtosis (α_e , black line, Eq. (6.5)) indicating the heaviness of the tail and the peakedness, respectively. The asterisks label the data points (α_s : grey stars, α_e : black stars) which are significantly different from one (Sign test, **: $p < 0.01$, *: $p < 0.05$).

of the stimulus the mean spike frequency slowly declines. This non-stationarity introduces positive serial correlations that may obscure correlations arising from a potential

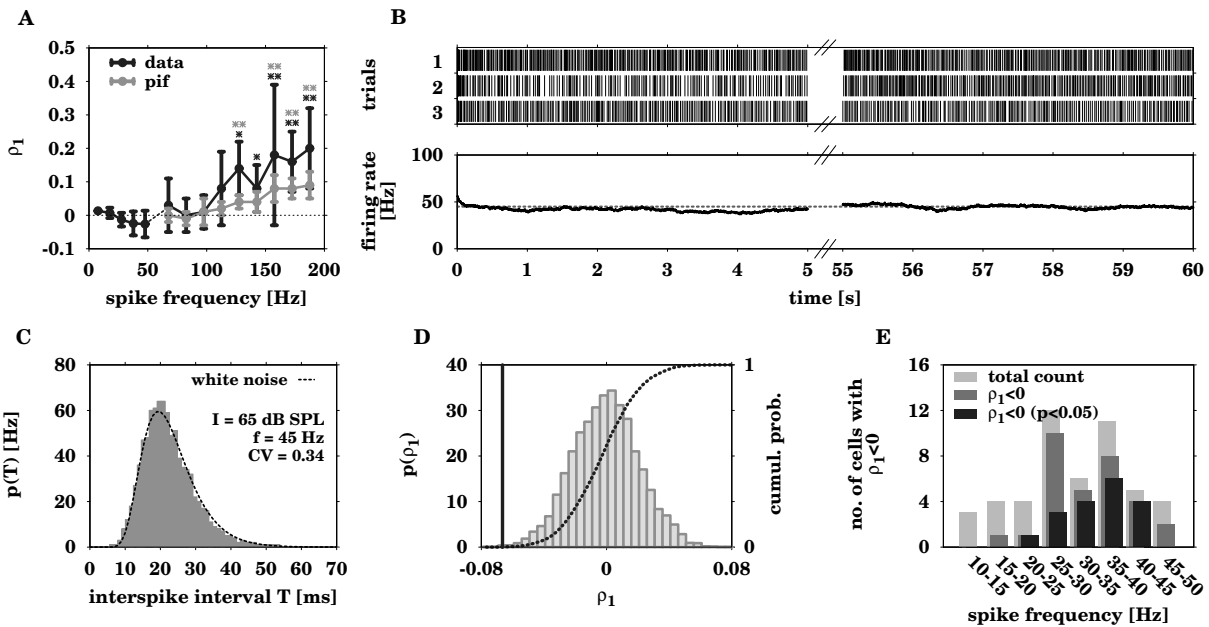


Figure 10.5: Correlations between successive interspike intervals. **A** Measured serial correlation coefficient $\rho_1 \pm$ s.d. (black lines) as a function of spike frequency f . The coefficients for $f \leq 50$ Hz were averaged over 14 cells (stimulus duration 1 min) while the ones for $f > 50$ Hz were averaged over 12 cells (stimulus duration 500 ms). The gray line shows the ISI correlations arising solely from the slight decrease of the spike frequency during the stimulus as computed from a PIF model (see text for details). The black asterisks label the data points which are significantly different from zero (Sign test, **: $p < 0.01$, *: $p < 0.05$). The gray asterisks indicate the data points for which the ISI correlations of the experimental data and of the PIF model are significantly different (Wilcoxon test, **: $p < 0.01$). **B** *top*: Spike trains recorded intracellularly during stimulation with a 1 min pure tone of 65 dB SPL and 6 kHz. *bottom*: Mean firing rate (average number of spikes per 500 ms time window) stays constant over time. **C** Comparison of the white noise distribution p_{wn} (dashed line, Eq. (6.1)) to the ISI histogram (gray boxes) obtained from the data shown in B. **D** The distribution of ISI correlations after shuffling ISIs (boxes), the corresponding cumulative histogram (dashed line) and the measured ρ_1 (solid line) for the data shown in B. **E** Number of cells with and without significantly negative ρ_1 ($p < 0.05$) as a function of spike frequency.

colored-noise source. We therefore computed the ISI correlations of a PIF model without spike-frequency adaptation with the time course of the input current adjusted such that the resulting time course of the mean spike frequency matches the experimentally measured one, and with an additive white noise that ensured the same CV of the ISIs as observed in the experimental data. The resulting ISI correlations (Fig. 10.5 A, gray line) are significantly lower than the ones obtained from the data. Thus the observed positive ISI correlations may indeed arise in part from a colored-noise source and not solely from the slow decline of the spike frequency.

For measuring the ISI correlations at lower spike frequencies we had to use acoustic stimuli of 1 min duration in order to obtain sufficiently large ISI statistics (≥ 300 ISIs per

trial). At low sound intensities the mean firing rate remained constant for the whole stimulus duration after an initial transient of a few hundred milliseconds (Fig. 10.5 B), which we discarded for the computation of correlations. Thus, the resulting ISI correlations are not obscured by slow changes of the mean spike frequency. Furthermore, the ISI histograms obtained from the spike responses to these long stimuli (Fig. 10.5 C) are also well described by the white-noise ISI density p_{wn} (Eq. (6.1)).

Using the long stimuli we indeed found slightly negative ISI correlations (Fig. 10.5 A). We tested the significance of these correlations by first calculating the distribution of serial correlation coefficients occurring by chance after shuffling the ISIs of each spike train of a given sound intensity (Fig. 10.5 D, gray bars). The correlation coefficient of the non-shuffled data (Fig. 10.5 D, solid line) was considered as significantly negative if the integral over the shuffled distribution (cumulative histogram, Fig. 10.5 D, dashed line) up to this value was smaller than 0.05. At spike frequencies in the range of 20–45 Hz most responses indeed showed significant negative ISI correlations (Fig. 10.5 E).

The results on ISI correlations exactly match the expectations based on the ISI distributions we measured. At low spike-frequencies a white-noise source shapes the ISI distribution and results, in interaction with an adaptation process, in negative ISI correlations. With increasing spike-frequency we observed a transition to a regime that is dominated by colored noise with the respective ISI distributions and the corresponding positive ISI correlations. This suggests that the dominating biophysical mechanisms generating the intrinsic noise change with increasing spike frequency.

10.2 Locust auditory transduction model with ion channel noise

To uncover potential biophysical mechanisms causing the observed interspike-interval variability we employed a model of the locust auditory receptor neuron and compared the interspike-interval statistics resulting from various possible noise sources with the experimentally measured ones. In the model (see Fig. 10.6 A, see chapter 7 for a detailed description) sound waves cause vibrations of the tympanal membrane. As a result mechanosensory ion channels in the membrane of auditory receptor neurons open and close and this way transform the vibrations into electrical currents. Caused by the resulting change of the receptor cell's membrane potential, voltage-dependent ion channels are activated that trigger action potentials.

Locust auditory receptor cells differ in their sensitivity but still have comparable variability measures, CV and $D_{r_{nwl}}$, as a function of spike frequency (Fig. 10.2). This excludes extrinsic noise and tympanal noise as possible noise sources. Furthermore, synaptic noise can be ruled out because locust auditory receptors are bipolar neurons that are directly attached to the eardrum (Gray, 1960) and generate action potentials without intermediate synapses. Thermal noise due to the membrane resistance was shown to have only a minor importance in neurons compared to other noise origins (Lecar and

Nossal, 1971; Manwani and Koch, 1999; van Rossum et al., 2003). Therefore, we expect that intrinsic noise caused by the random gating of ion channels is the main source of noise (Fig. 10.6 B). If a channel population is small, fluctuations between conducting and non-conducting states of single ion channels give rise to fluctuations of the ionic currents mediated by the channel population and cause membrane potential fluctuations as well as variability in spike timing (Schneidman et al., 1998).

For a minimal single-compartment conductance-based model of the locust auditory receptor neuron four different types of ionic currents need to be included: (i) the mechanosensory receptor current transducing the sound wave into an electrical signal, the (ii) sodium and (iii) delayed-rectifier potassium current for action potential generation, and (iv) an adaptation current mediating spike-frequency adaptation.

10.2.1 Mechanosensitive channel gating

A mechanosensory receptor channel in its simplest form includes two states, open and closed. A transition between these states results from external mechanical action, here the tension applied to the channel induced by tympanal vibration. These external forces

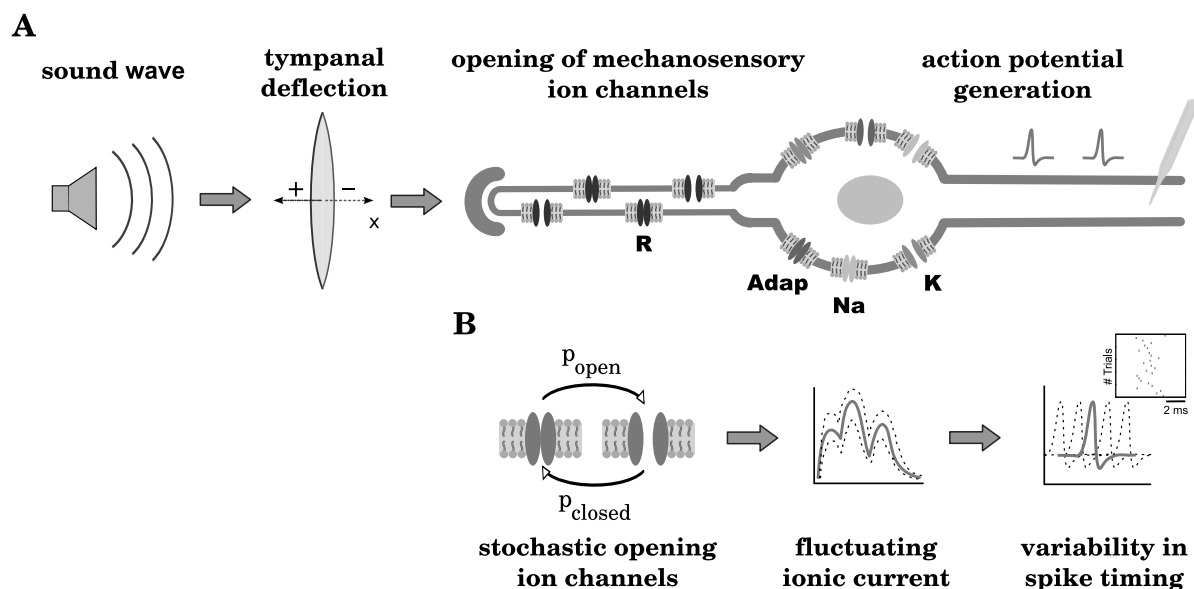


Figure 10.6: Auditory signal processing. **A** Schematic drawing of the auditory transduction cascade of *Locusta migratoria*. Tympanal deflections induced by sound waves of different intensities cause mechanosensory ion channels in the membrane of auditory receptor neurons to open and close. The resulting ionic current activates voltage-dependent ion channels that trigger action potentials. *R*: mechanosensory receptor channels, *Adap*: ion channels mediating spike-frequency adaptation, *Na*: sodium channels, *K*: delayed-rectifier potassium channels. **B** Our hypothesis is that the ISI variability originates from channel noise. Stochastic opening and closing of ion channels causes fluctuations of the mediated ionic currents eventually causing variability in spike timing.

presumably alter the energy of both states. Hence, the relationship between the channel open probability and the tympanal deflections is given by a Boltzmann relationship defined by Eqs. (7.2) - (7.4) as it was shown for transducer channels of vertebrate hair cells (Corey and Hudspeth, 1983; Howard and Hudspeth, 1988; Hudspeth et al., 2000). In the locust auditory system, the transducer channels are not yet identified, but indirect data (Gollisch and Herz, 2005) suggest the existence of two channel populations with Boltzmann gating.

The mechanical responsiveness of a mechanosensory channel to the tympanal deflection depends both on the gating force c and on the displacement x_0 of the tympanum for which half the channels of one population are open. The gating force c defines the sensitivity to a mechanical stimulus. It determines the slope of the Boltzmann function and, hence, the range of tympanal deflections x causing an opening of ion channels (see Fig. 10.7A, dashed line). For the case that the Boltzmann curves of two channel populations that open for opponent directions of tympanal vibration overlap, the transduction function, defined by the sum of the Boltzmann functions, determines the channel open probability at the tympanal resting position ($x = 0$) as well as the tympanal deflection for which the open probability approaches one (see Fig. 10.7A, solid line). Although the gating force defines the open probabilities for small and large tympanal deflections, it predominantly affects the lower dynamic range of a receptor neuron and, thus, the frequency of action potentials occurring spontaneously during absence of any stimulus or for sound intensities inducing small tympanal deflections (see Fig. 10.7B). The reason is that the average open probability determined over the whole tympanal deflection range is roughly constant for every c . This causes high ISI variability in the lower dynamic range which can result in a lack of the diffusion coefficient peak D_{rnwl} which was observed in locust auditory receptor cells (see Fig. 10.7C). In contrast to the gating force c , x_0 shifts the Boltzmann functions to higher and smaller tympanal deflections, respectively, while the slope remains unchanged (see Fig. 10.7D, dashed lines). This causes a displacement of the transduction function $g(x)$ to smaller and larger channel open probabilities, respectively (see Fig. 10.7D, solid lines). Thus, x_0 affects the spike frequencies of the whole dynamic range of a receptor neuron (see Fig. 10.7E). The sound intensities causing tympanal deflections which result in a mean channel open probability $\langle g(x) \rangle$ of 0.5 define the location of the diffusion coefficient peak D_{rnwl} . This position shifts with varying x_0 (see Fig. 10.7F). For the sound intensity causing a peak of D_{rnwl} ($\langle g(x) \rangle = 0.5$), the number of ion channel state transitions within a given time interval is maximal (Sigworth, 1980). No peak is observed for the case that combinations of c and x_0 result in $g(0) \geq 0.5$ at the resting position $x = 0$.

For modelling the locust auditory transduction cascade, we chose $x_0 = 6$ and $c = 0.5$ so that the dynamic range comprises an extent of about 40-50 dB SPL with low spontaneous spiking activity for sound intensities at the spike threshold and a D_{rnwl} peak value in the lower part of the dynamic range as observed for locust auditory receptor cells (cf. Fig. 10.2).

The time constant of the ion channels in the membrane of locust auditory receptor cells, which defines how fast the channels can respond to the tympanal vibration, is

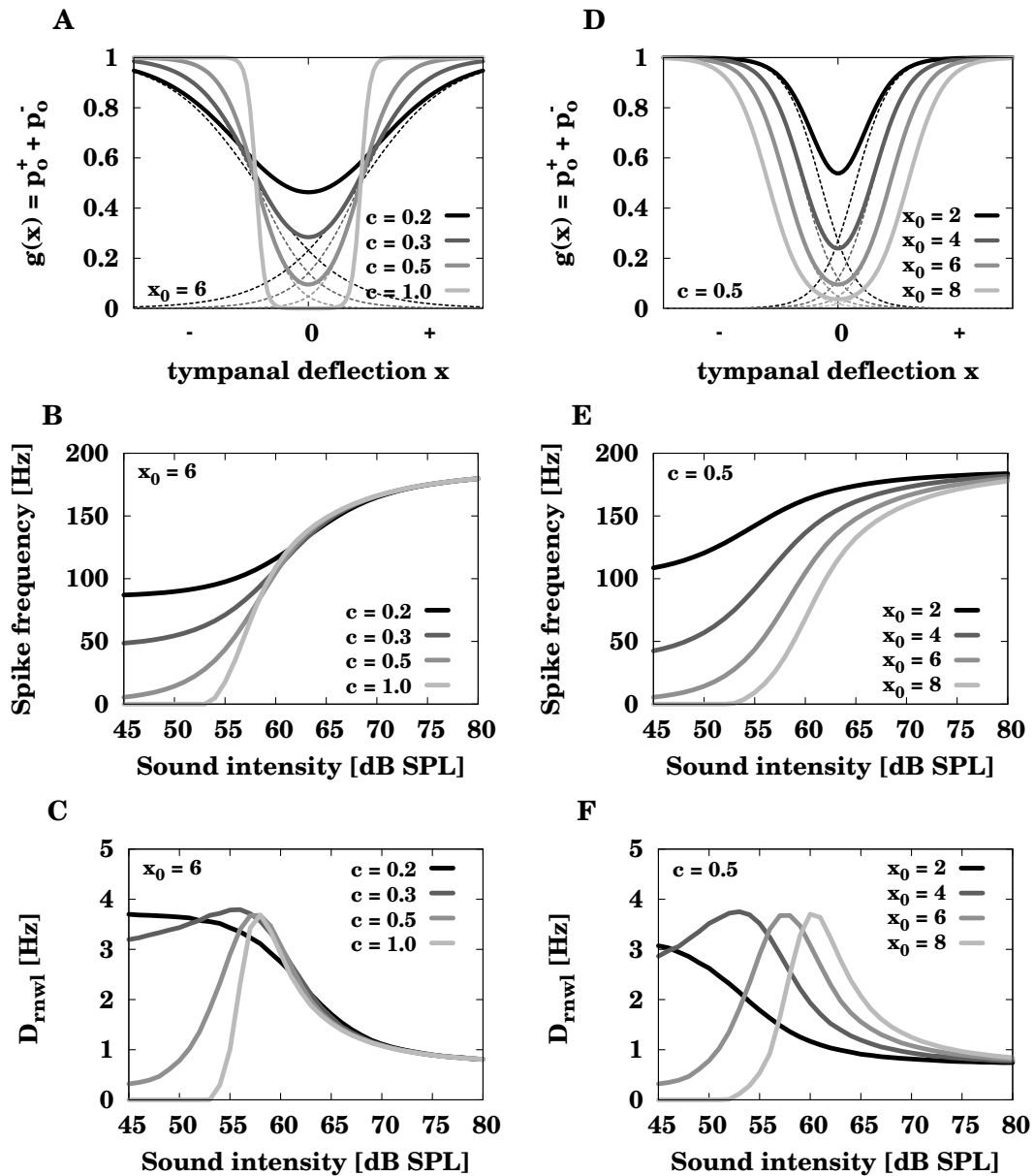


Figure 10.7: Influence of the mechanosensitive channel gating on the response properties of the auditory receptor cells. The relationship between the channel open probability and the tympanal deflection can be well described by the sum of two Boltzmann functions (see section 7.2). The gating force c as well as the tympanal displacement x_0 for which half the channels are open define the mechanical responsiveness of a channel to the tympanal deflection x . **A** The transduction function $g(x)$ (Eq. (7.2), solid lines) and the individual Boltzmann functions (dashed lines) as a function of the tympanal deflection for constant x_0 and varying c . **B** The spike frequency and **C** diffusion coefficient D_{rnwl} as a function of sound intensity for constant x_0 and varying c . **D-F** show the same curves as in A-C for constant c and varying x_0 .

not known, yet. A short time constant τ_r of 1 μs causes an immediate response, i.e. channel opening or closing, to the sound induced tympanal vibration (see Fig. 10.8A). The channel opening can easily follow the tympanal deflections and the stochastic case approaches the deterministic model. Hence, the ISI variability approaches zero (see Fig. 10.8B). In contrast, longer activation time constants yield a delayed channel opening and closing as response to the eardrum deflections (see Fig. 10.8A). Here, τ_r acts as a low-pass filter of the tympanal vibration x and causes a rise of D_{rnwl} (see Fig. 10.8 B). The increased variability results from the fact that the receptor channels are more and more driven into the regime where the mean open probability is 0.5 for which the variance of the current passing the channels is maximal (Sigworth, 1980). For a given τ_r , the standard deviation of the fraction of open receptor channels decreases at high spike frequencies, because the increasing amplitude of the tympanal deflections drives the receptor channels towards their fully open states where the fluctuations of the number of open channels decrease. For the simulations of the locust auditory transduction model, we chose $\tau_r = 0.1$ ms which yields ISIs of intermediate variability.

10.2.2 Single-current stochasticity

In a first set of simulations we investigated the effects of ion-channel stochasticity for each of the involved ionic currents individually. That is, in each of the simulations either (i) the receptor current I_R , (ii) the M-type adaptation current I_A ($I_B = 0 \mu\text{A}/\text{cm}^2$)

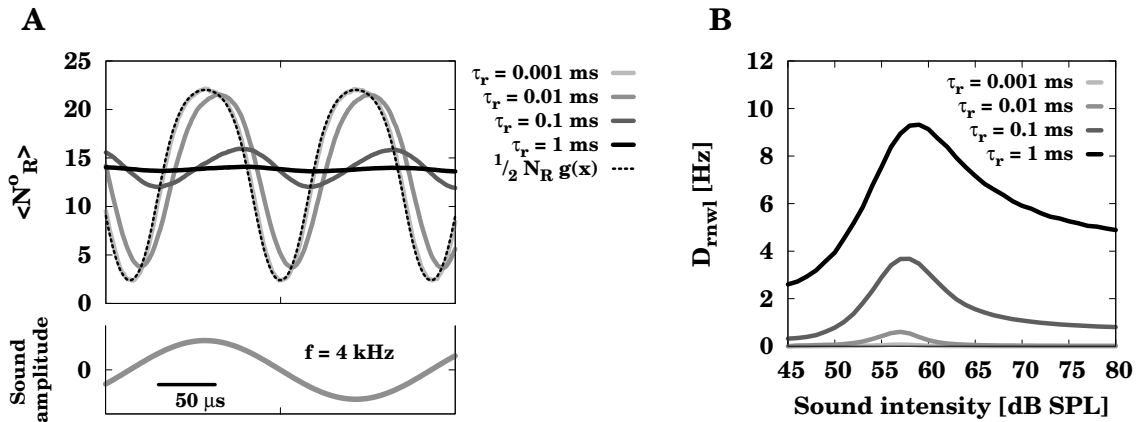


Figure 10.8: Low-pass filter properties of the mechanosensory receptor channels. The activation time constant $\tau_r = (\alpha_r + \beta_r)^{-1}$ of the stochastic auditory receptor channels ($N_R = 50$, $N=25/\text{channel}$ population) affects the state transition rates α_r and β_r which define the number of times per ms a channel changes its state and thus the number of open channels N_R^o over time. **A** The mean number of the stochastic opening channels $\langle N_R^o \rangle$ (average over 1000 repetitions) as response to the same sound stimulus for different time constants τ_r . In comparison, N_R^o of the deterministic receptor channels is illustrated as $\frac{1}{2}N_R g(x)$ (Eq. (7.2)-7.4). **B** The diffusion coefficient D_{rnwl} as a function of sound intensity for different τ_r .

or the voltage-dependent (iii) sodium I_{Na} or (iv) potassium current I_K was modeled as a stochastic current resulting from a finite population of ion channels, while all other ionic currents were modeled as deterministic currents corresponding to an infinite population of ion channels. For each case we varied the number of channels carrying the respective current and at the same time scaled the respective single-channel conductances inversely proportional to the number of channels. This results roughly in the same spike frequencies but different ISI variability as quantified by both the coefficient of variation, CV , and the diffusion coefficient, $D_{r_{nwl}}$.

Simulations of stochastic receptor, sodium and adaptation currents result in a high CV for stimuli close to the firing threshold that declines with increasing sound intensity (see Fig. 10.9 A,B,D). This is consistent with the observed statistics of the spike responses of the auditory receptor cells. Simulations of stochastic potassium channels, in contrast, yield CV s which remained roughly constant for all sound intensities (see Fig. 10.9 C).

The diffusion coefficient $D_{r_{nwl}}$ as a second measure for the regularity of a spike-count distribution showed qualitatively similar results (see Fig. 10.10). Stochastic receptor channels generate a peak in $D_{r_{nwl}}$ similar to the measured experimental data (cf. Fig. 10.2 E,F). The peak occurs at about the sound intensity inducing a tympanal displacement which

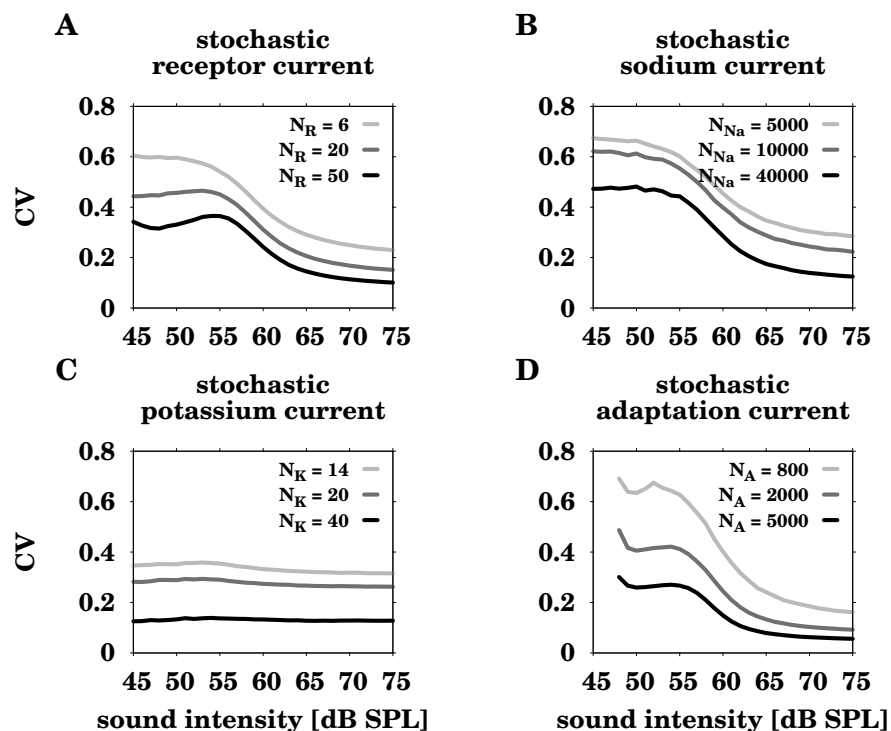


Figure 10.9: Comparison of the coefficient of variation resulting from different channel-noise sources. Shown is the coefficient of variation CV as a measure for the ISI variability computed from simulations of the auditory transduction cascade with different ionic currents modeled as populations of N stochastic ion channels as indicated.

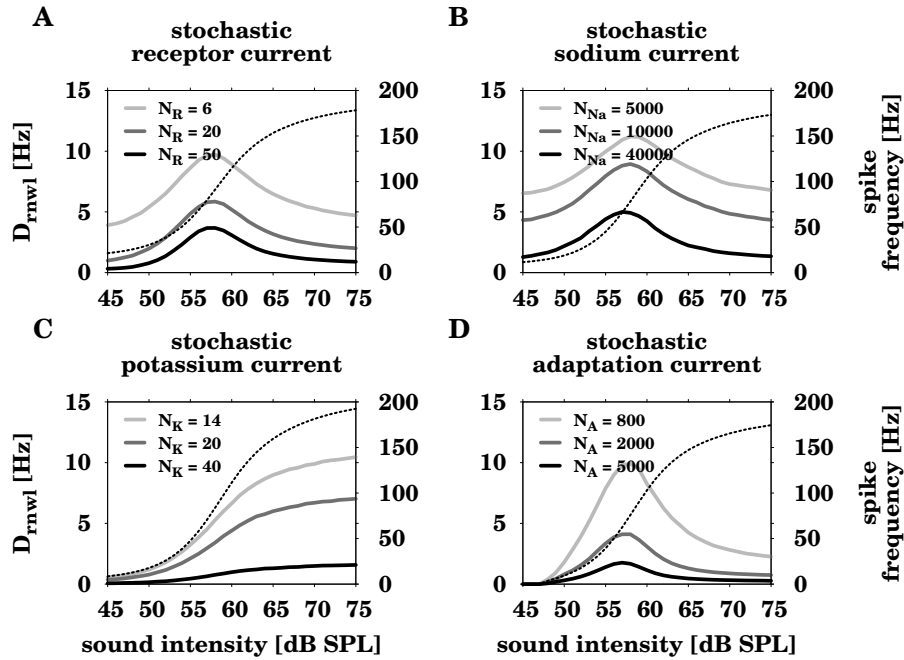


Figure 10.10: Comparison of the diffusion coefficient resulting from different channel-noise sources. Shown is the diffusion coefficient D_{rnwl} as a measure for the ISI variability computed from simulations of the auditory transduction cascade with different ionic currents modeled as populations of N stochastic ion channels as indicated. The right ordinate shows the corresponding mean spike frequency over sound intensity (dashed black line).

causes an opening of the receptor channels with a mean probability of 0.5 (as defined by Eq. (7.2), Fig. 10.10 A). For this open probability the variability of the ionic current and thus of the interspike intervals is maximal (Sigworth, 1980).

The voltage-gated sodium channels are responsible for action potential initiation. At membrane potentials close to the spike threshold, a random opening of channels can easily initiate an action potential (Schneidman et al., 1998). Similarly as in the model with stochastic receptor channels, sodium channel noise resulted in a peak of D_{rnwl} in the lower dynamic range of the receptor response comparable to the experimental data (see Fig. 10.10 B).

A stochastic delayed-rectifier potassium current responsible for the termination of an action potential, however, resulted in a sigmoidal increase of D_{rnwl} with increasing sound intensity (see Fig. 10.10 C) that definitely is not in agreement with the experimental data.

For modeling the adaptation current we used a population of voltage-gated M-type potassium channels. These channels are mainly activated during action potentials and slowly deactivate between them. Stochasticity of the adaptation channels again can reproduce the experimentally measured values of D_{rnwl} with a peak in the lower dynamic range (see Fig. 10.10 D).

To distinguish between stochastic currents showing similar ISI variability and to explore possible mechanisms accounting for both different shapes of ISI distributions and different ISI correlations observed in the experimental data, we furthermore investigated the shapes of the ISI distributions as well as the correlations between successive interspike intervals.

For the analysis of the ISIH shapes we adjusted the size of the stochastic channel populations such that all simulations with the different stochastic ionic currents resulted in the same steady-state spike frequency as well as the same CV and D_{rnwl} . Stochastic simulations of ionic currents with fast gating dynamics, i.e. sodium and receptor current, yield ISI distributions which are well described by the white-noise density p_{wn} (Eq. (6.1), Fig. 10.11 A,B). Simulations with stochastic M-type adaptation currents, however, result in ISI distributions that are more peaked than p_{wn} (see Fig. 10.11 C). However, these distributions can be well described by the colored-noise density p_{cn} (Eq. (6.2)) with a correlation time constant $\tilde{\tau}$ which is similar to the adaptation time constant.

The serial correlations were determined from the ISIs of the same simulations used for Fig. 10.10. The cases of both fast stochastic receptor (see Fig. 10.12 A) and fast stochastic sodium currents (see Fig. 10.12 B) are characterized by negative correlations at lag one. The case of slow stochastic adaptation currents, however, exhibits positive correlation coefficients ρ_1 (see Fig. 10.12 C).

To complete the ISI statistics for all types of ionic currents, we also analyzed the ISIH shape and the serial correlations for stochastic potassium currents which showed a spike-response variability that is clearly not in agreement with the experimental data. For a small number of potassium channels N_K , which was necessary to yield high variability

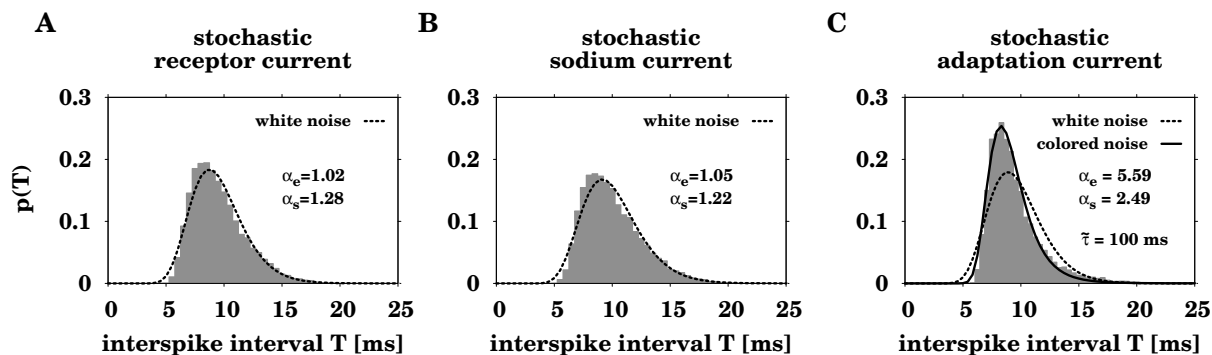


Figure 10.11: Interspike-interval distributions resulting from fast and slow channel noise. The ISI distribution resulting from the model with **A** fast stochastic receptor channels ($N_R = 50$, gray) and **B** fast stochastic sodium channels ($N_{Na} = 70000$, gray) in comparison with the white-noise density (dashed line, Eq. (6.1)). **C** Simulation of slow stochastic adaptation channels ($N_A = 2000$, gray) in comparison with the white-noise density (dashed line, Eq. (6.1)) and with the colored-noise density (solid line, Eq. (6.2)). In all simulations the steady-state spike frequency, the coefficient of variation ($CV = 0.25$) as well as the diffusion coefficient ($D_{rnwl} = 3\text{Hz}$) was kept the same. α_e : rescaled kurtosis; α_s : rescaled skewness; $\tilde{\tau}$: fitted correlation time constant of the colored noise.

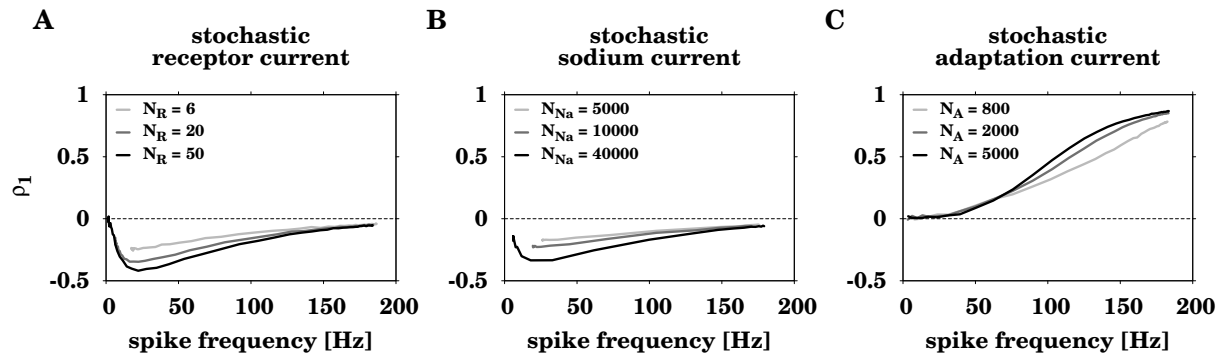


Figure 10.12: Interspike-interval correlations resulting from fast and slow channel noise. The serial correlation coefficients of lag1 resulting from the model with **A** fast stochastic receptor channels and **B** fast stochastic sodium channels as well as the ISI correlations from simulations of **C** slow stochastic adaptation channels for different channel numbers N as indicated.

comparable to the one observed in locust auditory receptors, the ISI distributions show a bimodal shape (see Fig. 10.13 A). This bimodality results in slightly positive serial correlations for succeeding ISIs (see Fig. 10.13 B). Simulations with a large number of potassium channels, in contrast, demonstrate that both the ISIH bimodality and the positive correlations, are a result of small channel numbers. Large N_K yields ISIH which have an almost right-skewed exponential shape which is neither comparable with a white-noise (see Fig. 10.13 C) nor with a colored-noise ISI density (not shown, see Fig. 10.11 for comparison). In addition, large N_K results in negative ISI correlations (see Fig. 10.13 D).

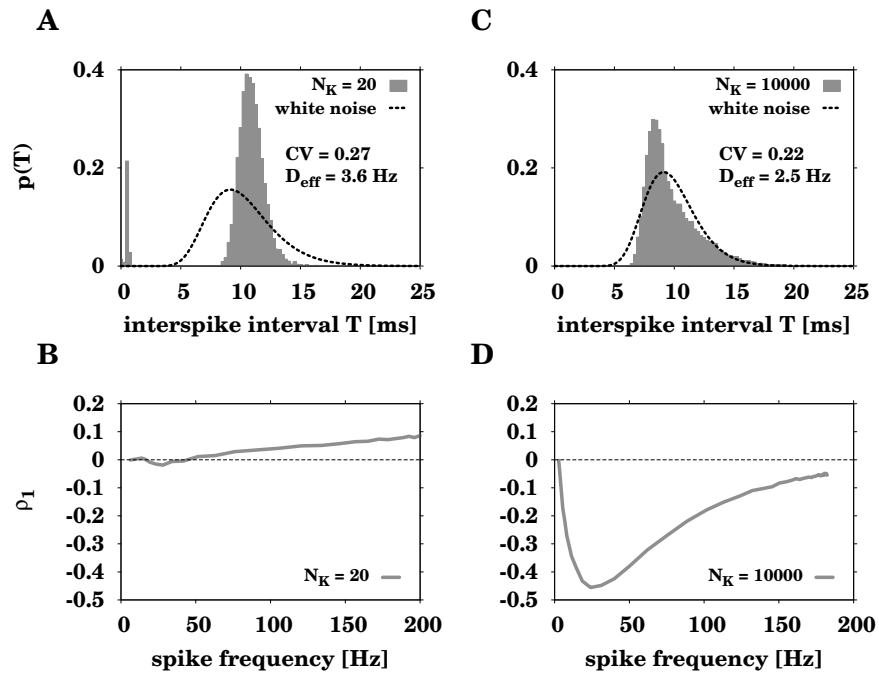


Figure 10.13: Interspike-interval distributions and correlations caused by stochastic potassium channels. **A,C** The ISI distributions from the model with stochastic potassium channels for (A) small and (C) large channel numbers N_K in comparison with the white-noise density (dashed line, Eq. (6.1)). **B,D** The serial correlation coefficients of lag1 from the model with stochastic potassium channels for (B) small and (D) large N_K .

How does adaptation contribute to the interspike-interval variability?

In the previous chapter we have shown that spike responses of locust auditory receptor neurons exhibit interspike-interval distributions that can be well described by the inverse Gaussian (IG) distribution and show negative interspike-interval correlations for sufficiently low sound intensities evoking spike frequencies of less than 50 Hz. These findings can be explained by a white-noise source that interacts with an adaptation current. Stimulations with sound intensities that elicit firing rates larger than 50 Hz result in more peaked distributions and positive interspike-interval correlations, as expected from an integrate-and-fire model of suprathreshold firing driven by colored noise. Simulations of a minimal conductance-based model of the auditory receptor neuron with single stochastic ionic currents suggest the receptor or sodium current as possible candidates of the white-noise source while slow channel noise from stochastic adaptation currents may act as the colored-noise source. This shows for the first time that noise from stochastic adaptation currents has a distinct effect on the ISI statistics and, thus, on the neuronal spike-response variability.

So far, spike-frequency adaptation has been demonstrated to play a functional role in the context of forward masking (Sobel and Tank, 1994), high-pass filtering (Benda et al., 2005; Benda and Hennig, 2008; Glantz and Schroeter, 2004), and response selectivity (Gabbiani and Krapp, 2006; Peron and Gabbiani, 2009a,b). If the neuron is driven by fast fluctuations, adaptation reveals itself in the interspike-interval statistics of neuronal firing, most prominently in the occurrence of negative correlations among interspike intervals (Wang, 1998; Ratnam and Nelson, 2000; Chacron et al., 2000; Liu and Wang, 2001; Chacron et al., 2001; Engel et al., 2008). These features can be phenomenologically captured in generalized integrate-and-fire models by introducing a slow inhibitory feedback variable, either acting as a dynamic threshold or as an inhibitory conductance or current (Geisler and Goldberg, 1966; Chacron et al., 2000; Liu and Wang, 2001; Muller et al., 2007; Benda et al., 2010), or in even more simplified models (Chacron et al., 2004; Lindner et al., 2005a; Schwalger and Lindner, 2010).

In previous studies on stochastic models with adaptation, fluctuations were considered to be fast, e.g. Poissonian synaptic spike trains passing through fast synapses or a white Gaussian input current representing a mixture of intrinsic fluctuations and background synaptic input. Channel noise, in contrast, is not only contributed by the fast ionic conductances, which establish the spike generating mechanism, but also by the ion channels that mediate adaptation currents. If the number of adaptation channels is not too large, the stochastic opening and closing of single channels will contribute a fluctuating component to the adaptation current. This noise contribution, which was so far ignored in the literature, and its impact on the ISI statistics is the subject of this chapter. Based on our findings regarding the dissimilarity of the ISI statistics resulting from fast stochastic ion channels and slow stochastic adaptation channels in section 10.2, the results described in this chapter arose from a cooperation with Benjamin Lindner and Tilo Schwalger from the Max Planck Institute for the Physics of Complex Systems in Dresden. The results summarized in section 11.1 and 11.2 have been published already in Schwalger et al. (2010). Within the scope of this cooperation, Tilo Schwalger studied the effect of adaptation noise on the ISI statistics of a perfect integrate-and-fire (PIF) model neuron by means of analytical techniques and numerical simulations. He contrasted stochastic adaptation with the commonly studied case of a fast fluctuating current noise and a deterministic adaptation current (corresponding to an infinite population of adaptation channels). The results of his work are summarized in short in section 11.1. I performed extensive simulations of a biophysically more realistic conductance-based model for these two limit cases of deterministic and stochastic adaptation. The results qualitatively confirm the ones for the PIF model and support the generality of our findings (see section 11.2). In addition, I performed simulations of locust auditory transduction model which comprised both fast current fluctuations and slow stochastic adaptation currents to test our hypothesis that a mixture of noise sources is necessary to explain the ISI statistics of spike responses of locust auditory receptor cells (see section 11.3, not part of the collaborative project published in Schwalger et al. (2010)).

11.1 How noisy adaptation of neurons shapes interspike interval histograms and correlations

This section gives a short review of the work of Tilo Schwalger that was initiated by our experimental findings. A detailed description can be found in Schwalger et al. (2010).

Tilo Schwalger analyzed the effect of adaptation noise on the ISI statistics of a PIF model. A PIF model represents a reasonable description in the suprathreshold firing regime, in which a neuron exhibits a stable limit cycle (tonic firing). The dynamics of the membrane potential V read:

$$\dot{V} = \mu - \beta W + \sqrt{2D}\xi(t), \quad (11.1)$$

where $\mu = I_0/C_m$, I_0 is the base current, C_m is the membrane capacitance and $W = N_{op}/N_a$ is the fraction of open adaptation channels. The scaling factor for the adaptation

current passing the N_{op} open channels reads $\beta = \bar{g}_a(\langle V \rangle - E_a)/C_m$ with the reversal potential E_a and with the average voltage $\langle V \rangle$ to obtain a voltage-independent adaptation current. The model was augmented with an inhibitory adaptation current mediated by a population of N_a adaptation channels (Fig. 11.1A). For simplicity, binary channels were assumed that switch stochastically between an *open* and a *closed* state (cf. Eq. (7.12), kinetic scheme). The transition rates depend on the presence or absence of an action potential. This can be approximated by passing the membrane potential V through a steady-state activation probability, $w_\infty(V)$, that attains values close to unity during action potentials, i.e. when the voltage exceeds the threshold, and is near zero for potentials below the firing threshold (Fig. 11.1B).

Although this model aims at the stationary firing statistics, we would like to stress that it exhibits spike-frequency adaptation in the presence of time-varying stimuli. In

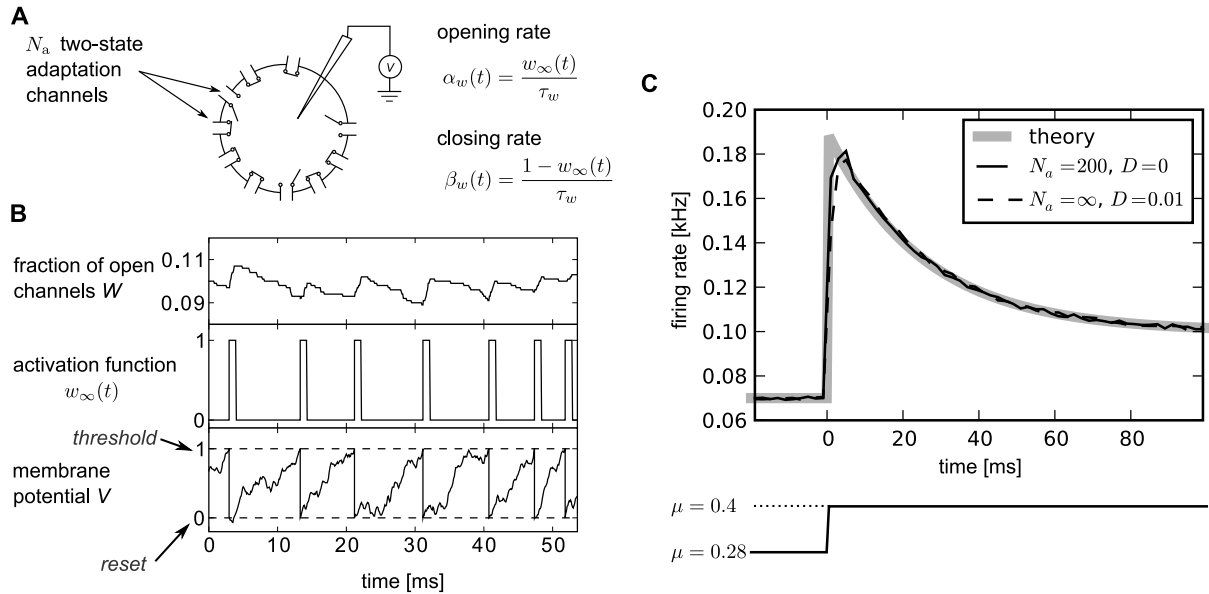


Figure 11.1: Integrate-and-fire dynamics with adaptation channels (taken from Schwalger et al., 2010). **A** Channel model: a population of N_a independent voltage-gated ion channels, which can be either in an open or closed state, mediate an adaptation current through a neuron’s membrane. **B** Perfect integrate-and-fire (PIF) model: Subthreshold dynamics of the membrane potential V (bottom). The variable V (in units of V_{th}) is reset to a value $V_{reset} = 0$ after crossing the threshold at $V = V_{th}$. Action potentials are not generated explicitly. Instead, the effect of an action potential is captured by the activation function $w_\infty(t)$, which is set to one in a short time window of 1 ms following each threshold crossing of the model (middle panel). The adaptation current is proportional to the fraction of open channels W (top panel). The sample traces were obtained from a simulation of a PIF model with $N_a = 1000$ adaptation channels, white noise intensity $D = 0.01V_{th}^2/\text{ms}$, adaptation time constant $\tau_w = 100$ ms, base current $\mu = 0.4V_{th}/\text{ms}$ and maximal adaptation current $\beta = 3V_{th}/\text{ms}$. **C** The time-dependent firing rate (top) in response to a step stimulus (bottom) is independent of the noise source (stochastic adaptation – solid line, deterministic adaptation plus white noise – dashed line). The gray line shows the mean adaptation of the non-dimensional theory derived in Schwalger et al. (2010).

particular, spike-frequency adaptation in response to a step stimulus is retained regardless of the considered noise source, channel numbers or approximations made during the theoretical analysis (Fig. 11.1C). This is a nice feature of the PIF model, for which the firing rate does not depend on the nature and magnitude of the noise. This allowed to vary the noise properties without altering the adaptation properties.

The stochastic ion channel model describing the dynamics of each individual adaptation channel could be considerably simplified by a diffusion approximation (Schwalger et al., 2010). The dynamics of the finite population of adaptation channels can be described by (i) the deterministic adaptation current and (ii) additional Gaussian fluctuations with the same filter time as the adaptation dynamics. The obtained multi-dimensional Langevin model ("diffusion model") that approximates the integrate-and-fire model with stochastic ion channels is hence given by

$$\dot{V} = \mu - \beta(w + \eta) + \sqrt{2D}\zeta(t) \quad (11.2a)$$

$$\tau_w \dot{w} = -w + w_\infty(t) \quad (11.2b)$$

$$\tau_w \dot{\eta} = -\eta + \sqrt{\frac{2\tau_w \sigma^2}{N_a}} \xi_a(t). \quad (11.2c)$$

This shows that a finite population of slow adaptation channels (instead of an infinite population and hence a deterministic adaptation dynamics) entails the presence of an additional noise $\eta(t)$ with a correlation time τ_w (time scale of the deterministic adaptation) and a variance which is inversely proportional to the number of channels. The membrane potential V of the PIF model is thus driven by four processes: (i) the base current μ , (ii) the white current fluctuations $\zeta(t)$ of intensity D (representing an applied current stimulus, channel noise originating from fast sodium or delayed-rectifier potassium currents, or shot-noise synaptic background input), (iii) a slow Ornstein-Uhlenbeck noise $\eta(t)$ due to stochasticity of the adaptation dynamics, and (iv) the deterministic feedback of the neuron's spike train $w(t)$ due to the deterministic part of the adaptation. In Eq. (11.2), the parameter β determines the strength of adaptation and σ^2 the noise strength.

To study the effect of the two different kinds of noise, the two limit cases were analyzed: In the limit of infinitely many channels, the adapting PIF model is only driven by white noise and μ . In this case, Eq. (11.2) reads

$$\dot{V} = \mu - \beta w + \sqrt{2D}\zeta(t), \quad (11.3a)$$

$$\tau_w \dot{w} = -w + w_\infty(t). \quad (11.3b)$$

We call this case *deterministic adaptation*.

In the opposite limit, only the stochasticity of the adaptation current but not the white

noise were considered. Setting $D = 0$ gives then

$$\dot{V} = \mu - \beta(w + \eta) \quad (11.4a)$$

$$\tau_w \dot{w} = -w + w_\infty(t) \quad (11.4b)$$

$$\tau_w \dot{\eta} = -\eta + \sqrt{\frac{2\tau_w \sigma^2}{N_a}} \zeta_a(t). \quad (11.4c)$$

We call this case *stochastic adaptation*. For this limit case, the adaptation variable can be approximated by an effective colored noise (Ornstein-Uhlenbeck noise; "colored noise approximation"). Hence, the dynamics of the model can be reduced to

$$\dot{V} = \tilde{\mu} - \beta \tilde{\eta} \quad (11.5a)$$

$$\tilde{\tau} \dot{\tilde{\eta}} = -\tilde{\eta} + \sqrt{\frac{2\tilde{\tau} \tilde{\sigma}^2}{N_a}} \zeta_a(t), \quad (11.5b)$$

where the effective parameters are scaled by a common scaling factor:

$$\tilde{\mu} = \lambda \mu, \quad \tilde{\tau} = \lambda \tau_w, \quad \tilde{\sigma}^2 = \lambda \sigma^2 \quad (11.6)$$

with $\lambda = (1 + \alpha \tau_w (\Delta w / v_{th}))^{-1}$.

ISI density

For the case of deterministic adaptation, the ISI densities can be well described by the IG probability density p_{wn} (Eq. (6.1)). Slight deviations of the simulated ISIH from the IG can only be seen for large intervals where the simulated density displays a stronger decay than the IG. Accordingly, the rescaled skewness, Eq. (6.4), and kurtosis, Eq. (6.5), show values slightly smaller than one.

In the opposite case of stochastic adaptation, the IG fails to describe the ISI histograms. The ISIHs possess a much stronger peak and decay slower at large interspike intervals compared to the IG with the same mean and variance of the ISIs. Hence, the rescaled skewness and kurtosis show values clearly larger than one. In addition, the ISIHs of the channel model are well approximated by both the diffusion model, Eq. (11.2), and the colored noise approximation, Eq. (11.5).

ISI correlations

Another clear distinction between stochastic and deterministic adaptation is revealed by the correlations between succeeding ISIs. For the case of deterministic adaptation purely negative correlation with an exponential decay are observed. In contrast, stochastic adaptation results in positive serial correlations with a slow exponential decay. This is also in agreement with the diffusion model. In addition, the good agreement of the colored-noise theory suggests, that adaptation noise effectively acts as a colored noise that slowly modulates the ISIs.

Mixed case of fast and slow noises

So far, it was that the two limit cases of the adapting PIF model can be well distinguished by the values of the shape parameters α_s and α_e relative to unity and the correlation coefficient ρ_1 relative to zero. Do these quantities also allow for an unambiguous distinction of the dominating source of noise in the more realistic case where both kinds of noise are present? To answer this question, simulations of the adapting PIF model for a fixed intensity of the white noise (“fast fluctuations”) but different sizes of the population of adaptation channels were performed.

For small channel numbers, i.e. large channel noise, both large values of the rescaled kurtosis $\alpha_e > 1$ and a positive serial correlation coefficient of adjacent ISIs were observed, indicating the strong impact of the colored-noise effect. As expected, at the other end of large channel population sizes the pure white-noise case can be recovered. In between, there is a critical channel number at which both the rescaled kurtosis crosses the line $\alpha_e = 1$ and the serial correlation coefficient changes its sign.

11.2 Effects of a stochastic adaptation current on the ISI statistics of a Hodgkin-Huxley-type model

In this section, we investigate whether the theoretical predictions based on the previously described PIF model are robust with respect to a more detailed Hodgkin-Huxley-type model. To this end, I performed simulations of the conductance-based Traub-Miles model with a M-type adaptation current (Eq. (8.1), Ermentrout et al., 2001).

11.2.1 Interspike-interval distributions

We separately considered the two cases of white noise input and a slow M-type channel noise to get an intuition of the individual effects on the ISI statistics. For deterministic adaptation, i.e. in the case of white noise input, the shape of the interspike-interval histograms can be well approximated by the IG distribution which was uniquely determined by the firing rate and the CV (see Fig. 11.2A). In the opposite case of a stochastic M-type current, the ISI variability solely depends on the number of slow adaptation channels (see Fig. 11.2B). The ISIHs show a strong disagreement with the IG exhibiting the same rate and CV. In particular, ISIHs exhibited a sharper peak compared to the relatively broad IG. In addition, for a small channel population ($N_a = 100$) the discreteness of the adaptation appears in the ISIH as single peaks that cannot be averaged out. This is related to realizations of the channel noise for which the fraction of open channels does not change during the ISI; realizations for which the fraction changes at least once lead to the continuous part of the ISI density.

The difference of the ISIHs observed both for a PIF and here for a Traub-Miles model with (i) deterministic and (ii) stochastic adaptation suggests that these two cases might be distinguishable from the shape of the ISIHs. To this end, we analyzed the ISIH

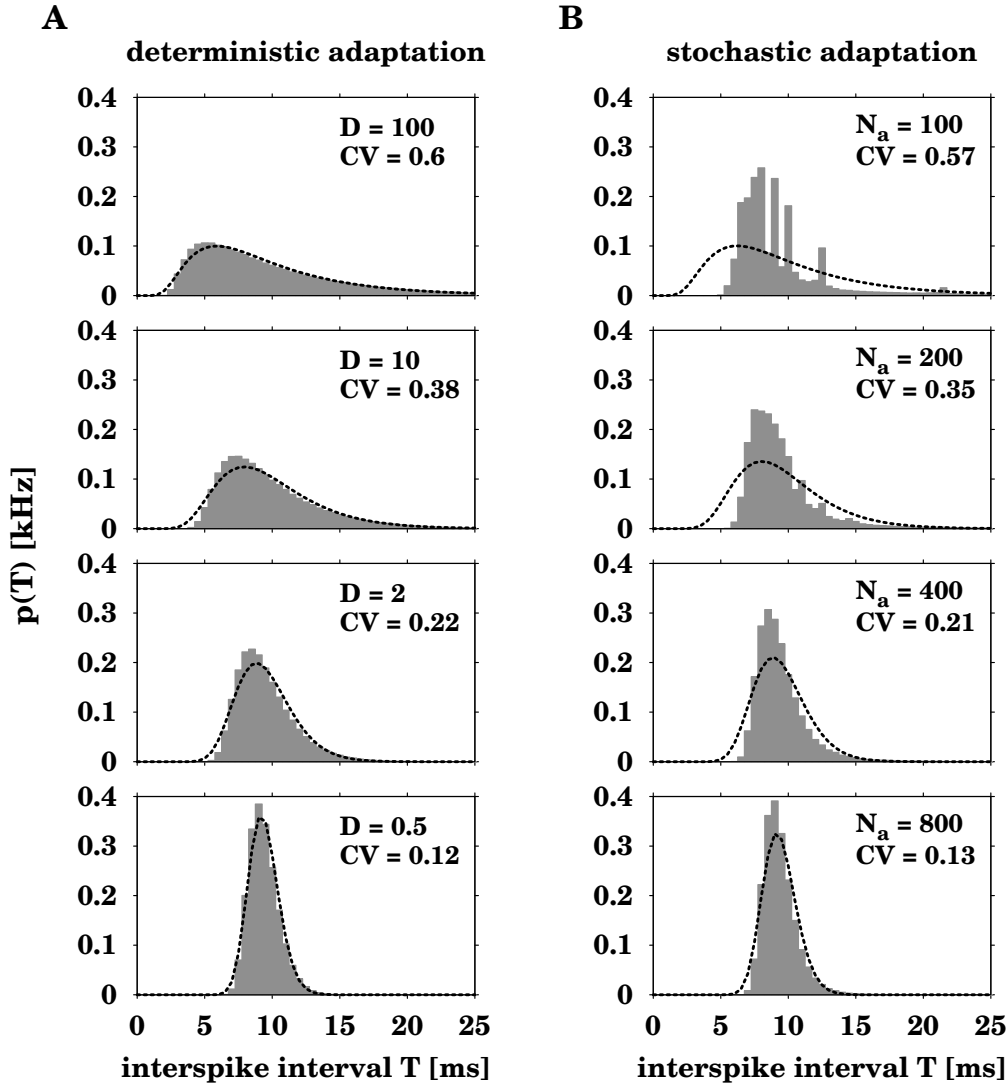


Figure 11.2: ISI histograms of the Traub-Miles model – deterministic vs. stochastic adaptation. **A** The ISI densities of the Traub-Miles neuron model with a deterministic M-type adaptation current ($N_a = \infty$) and white-noise driving (Eq. (8.1) – gray bars) is shown along with an inverse Gaussian (Eq. (6.1)) with the same mean and CV (dashed lines). To keep the firing rate at about $r = 100$ Hz the external driving current was adjusted from top to bottom according to $I = 9, 16.5, 17.7, 17.9$ (in $\mu\text{A}/\text{cm}^2$). **B** The ISI densities of the Traub-Miles model in the presence of a stochastic M-type adaptation current (Eq. (8.2) – gray bars) is shown along with an inverse Gaussian (Eq. (6.1)) with the same mean and CV (dashed line). Here, the external driving current was in all cases $I = 18 \mu\text{A}/\text{cm}^2$.

shapes using the rescaled skewness α_s , Eq. (6.4), and kurtosis α_e , Eq. (6.5), introduced by Schwalger et al. (2010). The rescaled skewness and kurtosis are significantly smaller for white noise than for adaptation noise in a wide range of CVs (see Fig. 11.3). This is in accordance with the pronounced peak of the ISIH in the case of stochastic adaptation (see

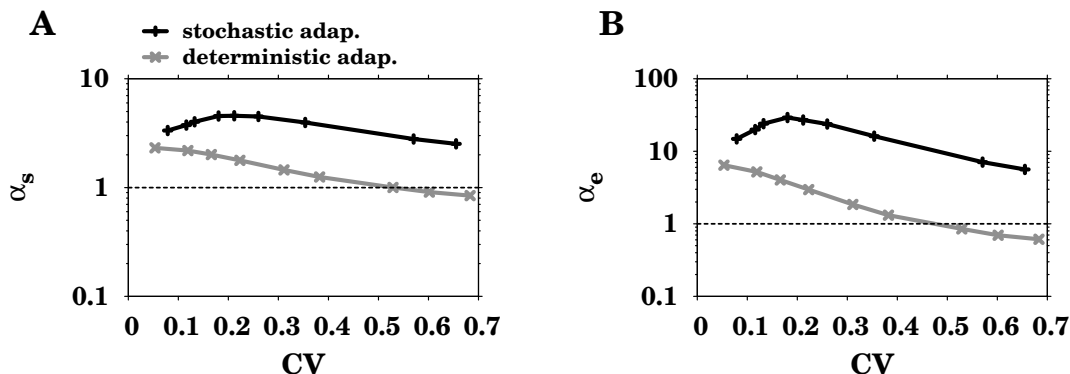


Figure 11.3: Shape parameters of the ISIH for deterministic and stochastic adaptation. **A** Rescaled skewness α_s , Eq. (6.4), and **B** rescaled kurtosis α_e , Eq. (6.5), as a function of the coefficient of variation (CV). For stochastic adaptation (Eq. (8.2), $D = 0$ – black curve) the number of channels was varied from $N_a = 2000$ to $N_a = 80$; for deterministic adaptation (Eq. (8.1), $N_a = \infty$ – gray curve), the noise intensity was varied from $D = 0.1$ to $D = 200$. The corresponding inverse Gaussian statistics, Eq. (6.1), is indicated by the dotted line.

Fig. 11.2B). However, the values are not strictly separated by $\alpha_{s/e} = 1$ as in the PIF model (see section 11.1, Schwalger et al., 2010). This discrepancy is not surprising, given that the Traub-Miles dynamics with constant input and white noise driving does not exactly yield an inverse Gaussian ISI density but only an approximate one. Importantly, however, the rescaled kurtosis α_e and skewness α_s for the case of deterministic adaptation quickly saturate at a finite value in the large τ_w limit (albeit not at unity, see Fig. 11.4, gray curves). This is markedly different from the case of stochastic adaptation. In this case, the rescaled kurtosis increases strongly as it was observed for the PIF model (see Fig. 11.4A,C, black curves). In a similar manner, the rescaled skewness also shows this distinct behavior for stochastic vs. deterministic adaptation, although the increase of the rescaled skewness is not as strong as for the rescaled kurtosis (see Fig. 11.4B,D, black curves).

11.2.2 Interspike-interval correlations

Another clear distinction between deterministic and stochastic adaptation appears in the serial correlations of ISIs (see Fig. 11.5). Similar as in the PIF model, the case of deterministic adaptation is characterized by negative ISI correlations at lag one, which are strongest at an intermediate time scale τ_w . In the limits $r\tau_w \rightarrow 0$ and $r\tau_w \rightarrow \infty$ where r denotes the stationary firing rate, however, the correlation coefficient at lag one, ρ_1 , vanishes as predicted by the theory of serial correlations (Schwalger et al., 2010) and as observed in previous studies (Liu and Wang, 2001; Benda et al., 2010). In contrast, the case of stochastic adaptation exhibits positive correlation coefficients ρ_1 , which show a maximum at an intermediate value of τ_w . For large $r\tau_w$ the correlations decrease again. This is in agreement with the colored-noise approximation (cf. section 11.1, Schwalger et al., 2010). The decrease might be due to the fact that the ISI variance grows faster with

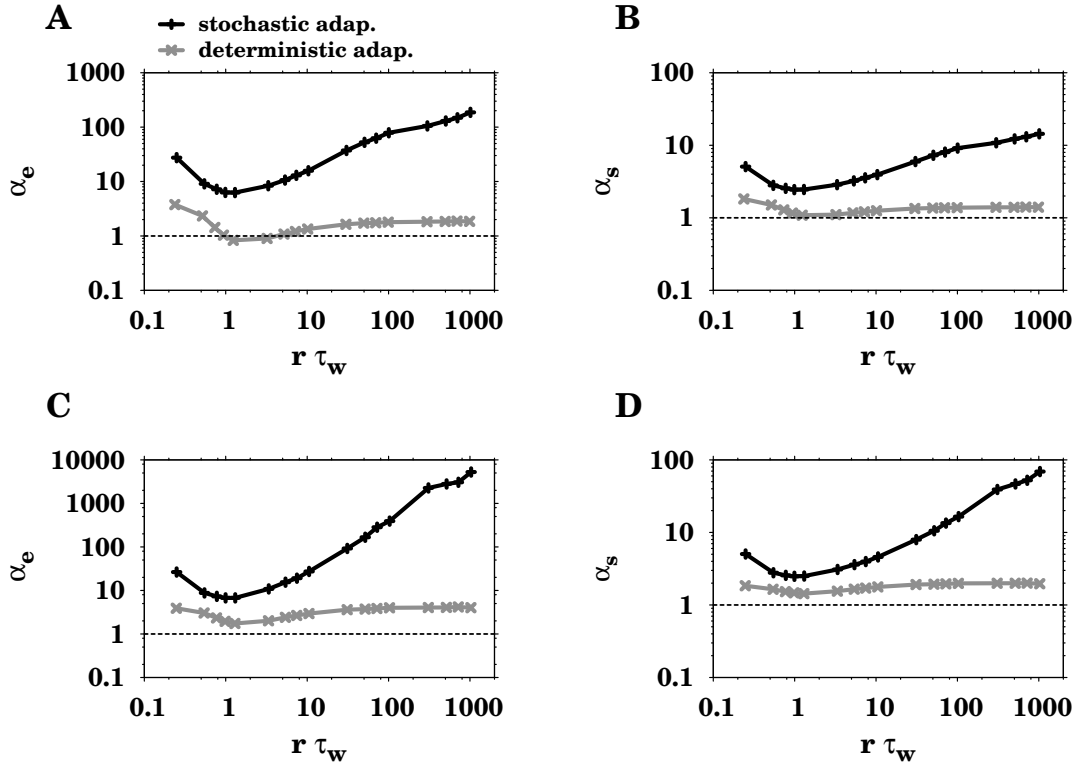


Figure 11.4: Shape parameters of the ISIH as a function of the time scale separation. **A,C** Rescaled kurtosis α_e , Eq. (6.5), and **B,D** rescaled skewness α_s , Eq. (6.4), as a function of the time scale separation $r\tau_w$ for stochastic adaptation (Eq. (8.2), $D = 0$, (A,B): $N_a = 200$; (C,D): $N_a = 400$ – black curve) and deterministic adaptation (Eq. (8.1), $N_a = \infty$, (A,B): $D = 10$; (C,D): $D = 2$ – gray curve). The corresponding inverse Gaussian statistics, Eq. (6.1), is indicated by the dotted line.

$r\tau_w$ than the covariance $\langle T_i T_{i+1} \rangle - \langle T_i \rangle^2$, thus the correlation coefficient is suppressed by the variance. A similar effect has been observed for a leaky integrate-and-fire model (Schwalger and Lindner, 2008).

Furthermore, the correlations show a rapid decay with the lag for deterministic adaptation (Fig. 11.6A) and an exponential decay for stochastic adaptation (Fig. 11.6B). As in the PIF model, the exponential decay is slower for large time constants τ_w .

11.2.3 Mixed-case model with fast and slow noise sources

Finally, we inspected the case in which both white noise and slow adaptation noise is present (Fig. 11.7). We fixed the noise intensity of the white noise and varied the number of adaptation channels N_a . In the Traub-Miles model one finds qualitatively similar curves as in the PIF model. In particular, the serial correlation coefficient at lag one shows a transition from positive to negative ISI correlations at a certain number of adaptation channels (Fig. 11.7A). This value can be used to define two regimes – one dominated by adaptation noise (white region) and another one dominated by white noise

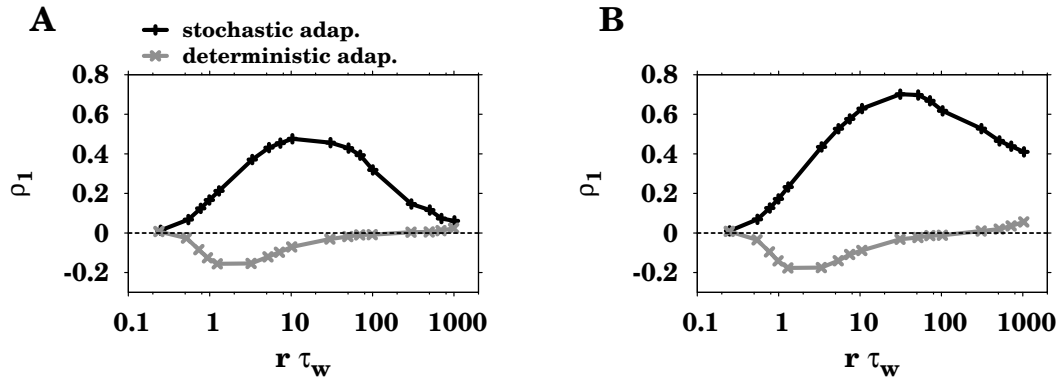


Figure 11.5: Serial correlation coefficient at lag 1 as a function of the time scale separation. **A,B** The serial correlation coefficient, Eq. (6.6), at lag 1 as a function of the time scale separation $r\tau_w$ for stochastic adaptation (Eq. (8.2), $D = 0$, (A): $N_a = 200$; (B): $N_a = 400$ – black curve) and deterministic adaptation (Eq. (8.1), $N_a = \infty$, (A): $D = 10$; (B): $D = 2$ – gray curve). The zero baseline is indicated by a dotted line.

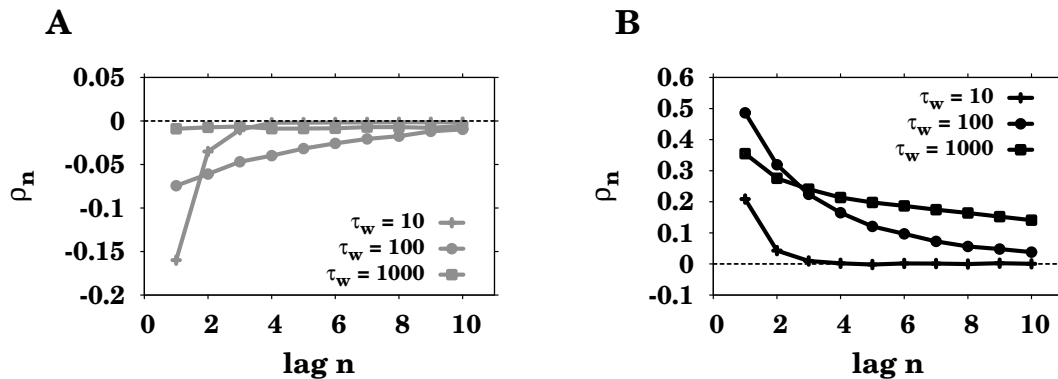


Figure 11.6: Serial correlation coefficient as a function of the lag between ISIs. **A,B** The serial correlation coefficient ρ_n , Eq. (6.6), as a function of the lag n for different time constants τ_w in *ms* as indicated for (A) deterministic adaptation (Eq. (8.1), $N_a = \infty$, $D = 10$) and (B) stochastic adaptation (Eq. (8.2), $N_a = 200$, $D = 0$). The zero baseline is indicated by a dotted line.

(gray-shaded region). In the adaptation-noise dominated regime the scaled kurtosis α_e is larger than in the white-noise dominated regime (Fig. 11.7B).

The observation that key features of the ISI statistics in the presence of a stochastic adaptation current seem to be conserved across different models suggests a common mechanism underlying these features. This mechanism is based upon the fact that a stochastic adaptation current can be effectively described by an *independent* colored noise. The long-range temporal correlations of this noise naturally yield positive ISI correlations and a slow modulation of the instantaneous spike frequency. The latter typically involves a large kurtosis due to the increased accumulation of both short and long ISIs. A significant amount of colored noise can effect the kurtosis and the ISI correlations so strongly, that details of the spike generation seem to be of minor

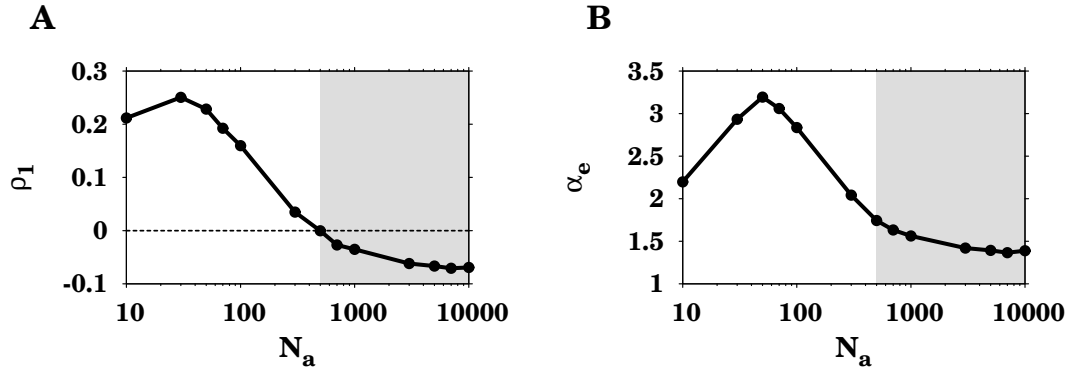


Figure 11.7: ISI statistics of the Traub-Miles model in the presence of both stochastic adaptation and white noise. **A** The serial correlation coefficient ρ_1 , Eq. (6.6), at lag one in the mixed case at a fixed amount of white noise ($D = 10$) and varying channel numbers N_a . The intersection of the ρ_1 curve with the zero line (dotted line) defines the adaptation-noise dominated regime (white region) and the white-noise dominated regime (gray-shaded region). **B** The corresponding values of the rescaled kurtosis α_e , Eq. (6.5).

importance. Thus, it becomes plausible that the spike statistics of a real neuron could be used to infer the dominant source of noise.

11.3 Locust auditory transduction model with mixed channel noise sources

The simulations of the locust auditory transduction model with single stochastic ionic currents (see section 10.2.2) showed that stochastic M-type adaptation currents explain both the ISI distributions and positive correlations of the experimentally measured spike responses of the upper dynamic range. In contrast, both stochastically gated sodium as well as receptor channels reproduce the ISI distributions of the lower dynamic range and in interaction with the deterministic adaptation current also reproduce the observed negative correlations.

This suggests that at least two processes are needed to explain the experimental data: (i) a process generating fast current fluctuations, which dominate at low sound intensities, and (ii) a slow adaptation process both for generating negative correlations in interaction with the fast noise and for generating slow current fluctuations, which dominate at high sound intensities.

In the previous section, we have shown that a mixed-case model with both white noise and slow stochastic adaptation gives rise to a transition from positive to negative ISI correlations as well as to a transition of the ISIH shape. This suggests that stochastic channels working on a fast time scale and slow stochastic adaptation channels might explain the ISI variability observed in locust auditory receptor cells. In order to test this hypothesis, we simulated the locust auditory transduction model with a stochastic

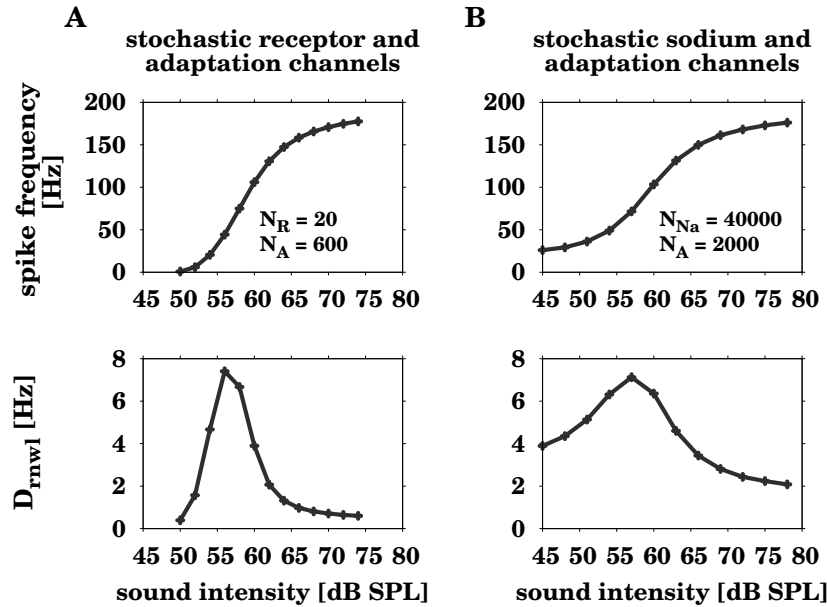


Figure 11.8: Interspike-interval statistics of the mixed stochastic channel models. Shown are the spike frequency (*top*) and the diffusion coefficient D_{rnw1} (*bottom*) as a function of sound intensity of the locust auditory transduction model with stochastic adaptation channels and either **A** stochastic receptor or **B** stochastic sodium channels with the channel numbers N as indicated.

M-type adaptation current in combination with stochastic currents mediated by either mechanosensory receptor (Figs. 11.8 A, 11.9D-F) or voltage-dependent sodium channels (Figs. 11.8 B, 11.9G-I) and contrasted the ISI statistics to the ones of the experimental data (Figs. 11.9 A-C).

Both mixed-case models are able to explain the ISI statistics of the auditory receptor cells' spike responses. The ISI variability quantified by D_{rnw1} shows a peak at the lower dynamic range of the receptor response (Fig. 11.8). The coefficient of variation reveals high variability for low steady-state spike frequencies which declines with increasing rate (Figs. 11.9 D,G). In addition to the CV , both the rescaled skewness α_s and kurtosis α_e confirm the transition from an inverse Gaussian to the more peaked colored-noise distribution (Figs. 11.9 E,H). For low spike frequencies, α_e and α_s take values close to one indicating a strong white-noise influence. With increasing spike frequency, α_e and α_s show a monotonic rise to large values. This implies that the ISI density is more skewed and more peaked compared to an IG which illustrates the prevalence of colored noise in this firing rate regime. Furthermore, with increasing spike frequency, the ISI correlations exhibit a transition from negative correlations resulting from predominant white noise driving interacting with the adaptation current to positive correlations indicating strong impact of colored noise (see Figs. 11.9 F,I).

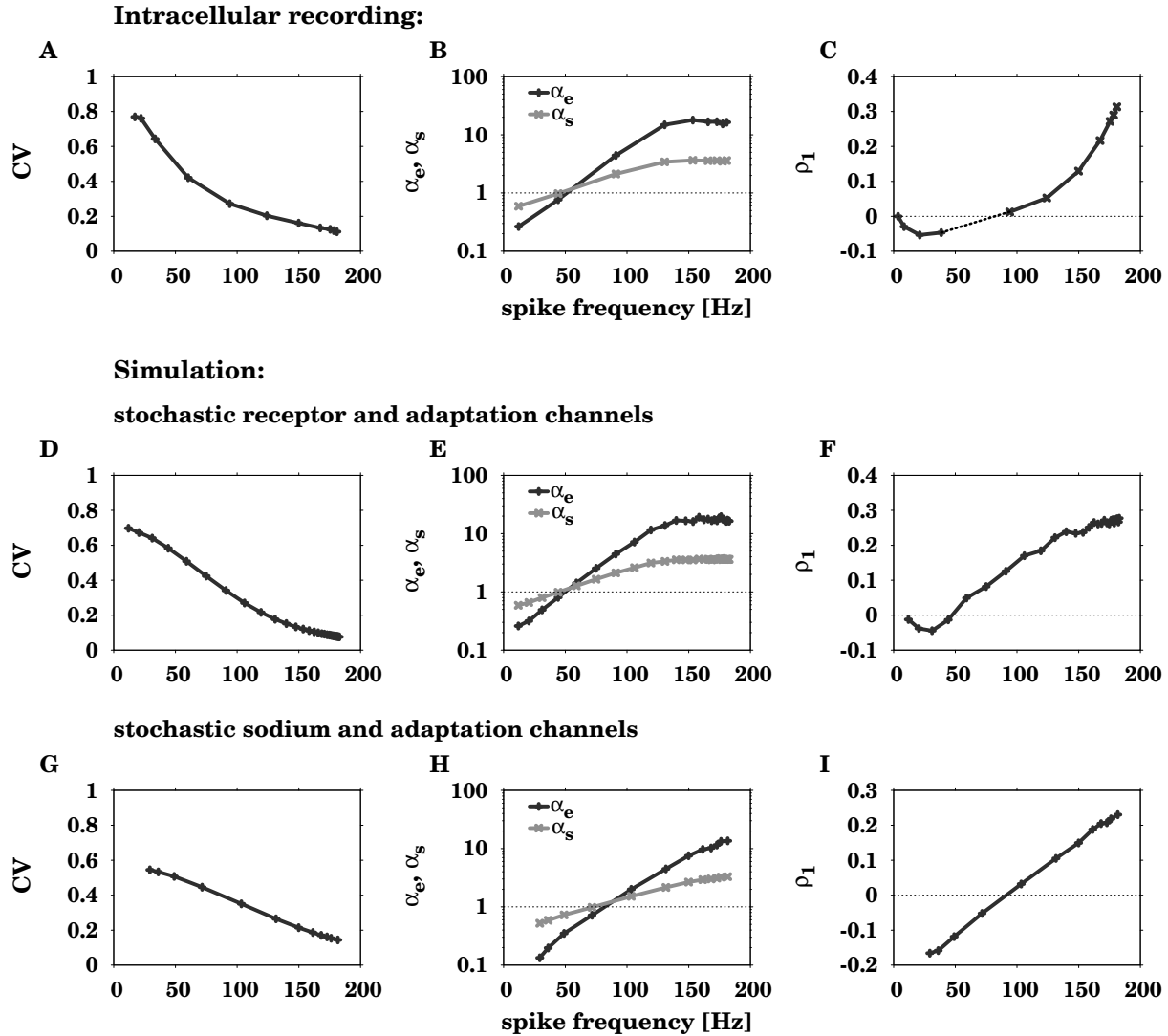


Figure 11.9: Comparison of the model with stochastic receptor/sodium and adaptation channels with experimental data. **A,D,G** Coefficient of variation (CV), **B,E,H** the rescaled skewness (α_s , Eq. (6.4)) and kurtosis (α_e , Eq. (6.5)), and **C,F,I** the serial correlation coefficient of lag 1 (ρ_1 , Eq. (6.6)) as a function of spike frequency. The ISI statistics of the recorded neuron (A-C) is a subset of data shown in Figs.10.2 C,D, 10.4 C, and 10.5 A. The serial correlation coefficients shown in C are taken from two auditory receptor cells which were recorded during stimulation with different pure-tone durations: 1 min stimulus for data of low spike frequency, 500 ms stimulus for data of high spike frequency (same cell as in A and B). For the simulation of the model with stochastic receptor and adaptation channels (D-F) we used $N_R = 20$ and $N_A = 600$ number of channels. For the simulation with stochastic sodium and adaptation channels (G-I) we used $N_{Na} = 40000$ and $N_A = 2000$.

Chapter 12

How does adaptation contribute to the spike-count variability?

Two types of neuronal variability are usually discriminated: Interspike-interval and spike-count variability. In the previous chapter, we have shown that a mixture of fast stochastic ionic currents and stochastic currents mediating spike-frequency adaptation shape the interspike-interval variability in locust auditory receptor cells. In this chapter, we analyze the latter type of spike-response variability. We quantify the spike-count variability of locust auditory receptor cells by the Fano factor which is calculated for different counting time frame lengths. Furthermore, we compare the experimental Fano-factor curves to the stochastic channel model of the locust auditory transduction cascade with stochastic adaptation currents.

12.1 The auditory system of locusts comprises spike-frequency adaptation with two time constants

Spike-count variability quantified by the Fano factor can quantify variability on different time scales. To measure variability on longer time scales, it is necessary to have recordings of the neuronal responses of locust auditory receptor neurons with a long spike train duration. So far, locust auditory spike responses have not been measured during stimulation with tones of long time duration. To this end, we performed intracellular recordings during stimulation with long-lasting pure tones of 1 minute duration.

The spike frequency of locust auditory receptor cells is known to decay during the first one hundred milliseconds after onset of a pure-tone stimulus of constant intensity (Römer, 1976; Benda et al., 2001). The spike responses of the auditory receptors recorded during stimulation with long-lasting tones show a mean spike frequency which decays over two timescales and which can be described by the sum of two exponential equations (see Fig. 12.1).

We measured the effective time constants of the two adaptation processes by fitting

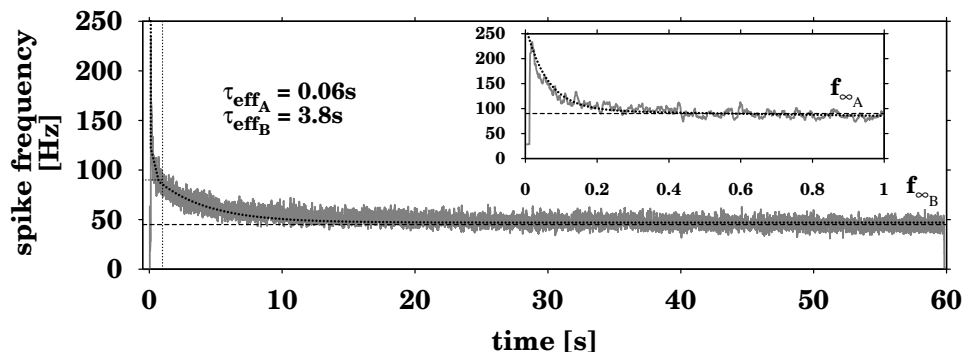


Figure 12.1: Two processes mediating spike-frequency adaptation in locust auditory receptor neurons. The mean spike frequency defined by the inverse interspike intervals across 15 spike trains (1 min duration) shows a frequency decay over two time scales. The fast adaptation current reduces the spike frequency over a range of approximately 100 ms (see inset, marked as fine dashed line in the main figure) and results in a temporary steady-state spike frequency $f_{\infty A}$. Subsequently, the slow component adapts the neuron in the range of several seconds to the final steady-state spike frequency $f_{\infty B}$. The black dotted line shows a fit of $f(t) = f_A \exp^{-t/\tau_{eff_A}} + f_B \exp^{-t/\tau_{eff_B}} + f_{\infty B}$ to the data.

exponentials to the mean spike frequency as a function of time (see Fig. 12.2A,B). The first adaptation process causes a spike-frequency decay with effective time constants in the range of 100 ms which is the time scale already known for locust auditory receptor cells (see Fig. 12.2C). The second adaptation process causes additionally a decay of the spike frequency with effective times constants of several seconds depending on sound intensity (Fig. 12.2D).

12.2 Spike-count variability in locust auditory receptors

In the previous chapter, we have shown that stochastic adaptation currents working on a time scale of a hundred milliseconds contribute to the interspike-interval variability and shape both ISI histograms and correlations. In contrast to fast adaptation processes, slow processes mediating spike-frequency adaptation on a time scale of several seconds, however, scarcely affect the statistics of interspike-intervals. Such slow processes instead can show distinct effects on the spike-count statistics quantified by the Fano factor $F(t_c)$ (Eq. (6.7), Middleton et al., 2003). This measure may depend on the observation time frame t_c and can signify variability additionally on a long time scale of several seconds or even minutes. Hence, spike-count variability can incorporate processes working not only on fast time scales but also on slow ones, such as a slow adaptation current with a time constant of several seconds.

The Fano factor approaches $F(t_c) = 1$ for small t_c (Teich et al., 1997). For large t_c , $F(t_c)$ is related to the ISI correlations and the coefficient of variation (Eq. (6.8), Cox and Lewis, 1966). For a renewal process with uncorrelated ISIs the Fano factor for large t_c is given by $F_{\infty} = CV^2$. Negative ISI correlations, in contrast, yield a decreased spike-count

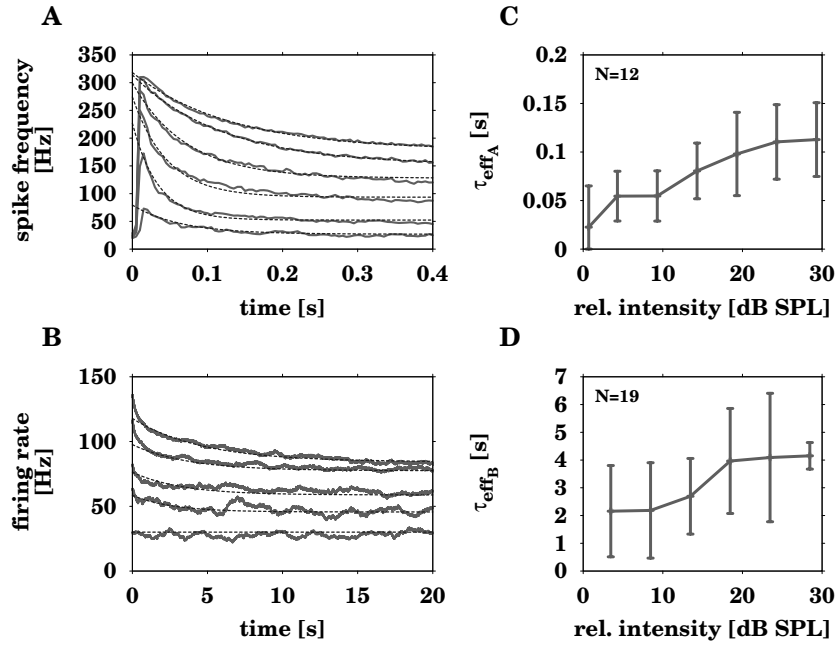


Figure 12.2: Effective time constants of two adaptation processes. **A** The mean spike frequencies of one receptor neuron (Stimuli: 500 ms pure tones of different sound intensities) defined as the inverse interspike interval show spike-frequency adaptation with a fast time scale. **B** The firing rate of another receptor neuron (Stimuli: 1 min pure tones of different sound intensities) defined as the average number of spikes per time window shows a slow component of spike-frequency adaptation. Here, the fast adaptation time constant shown in A was averaged out by using a time window of 100 ms. In A and B the spike frequencies decay in an approximately exponential manner (dashed lines) to their steady-states with effective time constants τ_{eff} . **C, D** The mean effective time constants \pm s.d. of the fast (C, τ_{effA}) and the slow adaptation process (D, τ_{effB}) measured from recordings of $N = 12$ receptor cells stimulated with 500 ms pure tones and $N = 19$ receptor cells stimulated with 1 min pure tones, respectively, show short time constants τ_{effA} in the range of 100 ms and long time constants τ_{effB} in the range of several seconds. The time constants are shown as a function of sound intensity relative to the threshold intensity (0 dB SPL) of a receptor cell.

variance compared to the one of a renewal process, while positive serial correlations cause Fano factors increasing as a power-law function with exponent κ which gives rise to a minimum of $F(t_c)$ at defined counting times t_c (Middleton et al., 2003).

The Fano factor curves estimated from spike responses of locust auditory receptor neurons, recorded during stimulation with tones of 1 minute duration, show a minimum at moderate counting times and a rise of $F(t_c)$ at large t_c (see Fig. 12.3A). Furthermore, depending on sound intensity, the experimental data display a shift of both the Fano factor minimum t_c^{min} and the exponent κ (see Fig. 12.3A-C). The Fano factor curves of the lower and medium/upper dynamic range (see Fig. 12.3D) highly differ in their shape. For sound intensities close to the spike threshold, the position of the minimum is in the range of 250 ms (see Fig. 12.3A,B,E). For sound intensities of the medium to upper dynamic range, t_c^{min} shifts to smaller counting times down to 25 ms (see Fig. 12.3A,B,F). In

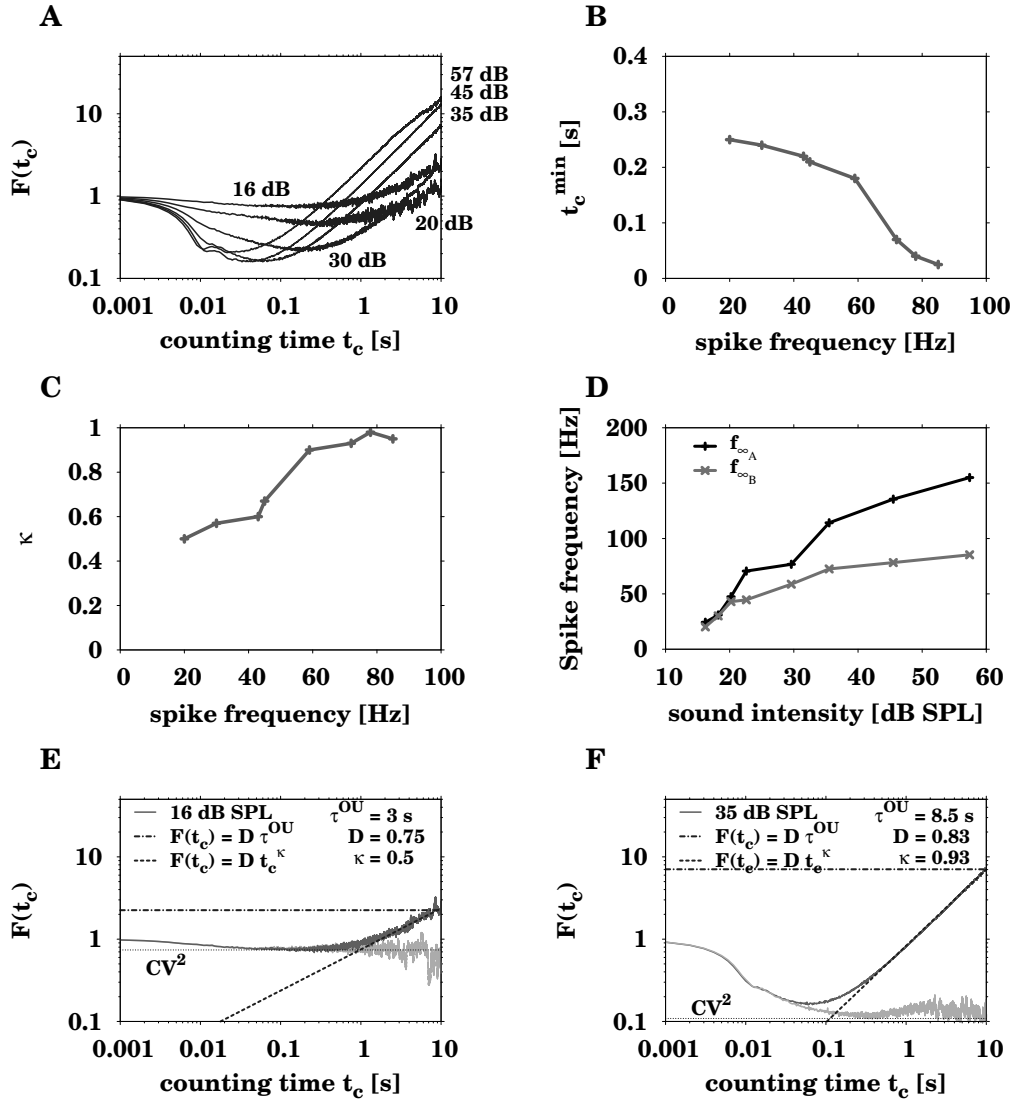


Figure 12.3: Fano factor analysis of the spike trains of an auditory receptor neuron for different sound intensities. **A** Fano factor curves for the steady-state spike trains of an intracellularly recorded receptor neuron for six different sound intensities (dB as abbreviation for dB SPL). **B,C** The counting time of the Fano factor minimum t_c^{\min} (**B**) and the exponent κ (**C**, cf. Eq. (6.12)) as a function of spike frequency. **D** The steady-state spike frequency of the receptor neuron shown in **A** after the frequency decay resulting from the fast adaptation process ($f_{\infty A}$, black line) and after the second decay resulting from the slow adaptation process ($f_{\infty B}$, gray line) as a function of sound intensity (cf. Fig. 12.1). **E,F** The Fano factor curves of the original spike trains (dark curve) and of the spike trains where the interspike intervals were shuffled (light curve) for a sound intensity of the lower (**E**) and upper dynamic range (**F**) of the same auditory receptor cell shown in **A**. The dashed lines show the theoretical curves derived by Middleton et al. (2003) for moderate counting times ($t_c < \tau^{OU}$, Eq. (6.12)) and for $t_c \rightarrow \infty$ defining the saturation regime (Eq. (6.13)).

all cases, there is no saturation of $F(t_c)$ visible up to a counting time of 10 s. Furthermore, the exponent κ of the rising curve part increases with increasing sound intensity. Only for sound intensities of the upper dynamic range, the exponents seem to remain constant at values close to one (see Fig. 12.3A,C).

The Fano factor curves obtained by a random shuffling of the interspike intervals (see Fig. 12.3E,F, light gray curve), where any ISI correlation has been removed, tend toward CV^2 as it is known for a renewal process. The measured Fano factor curves (see Fig. 12.3E,F, dark gray curve) show larger $F(t_c)$ values for large t_c compared to the shuffled ones (see Fig. 12.3E,F, light gray curve) demonstrating that the large $F(t_c)$ values at $t_c = 10$ s and the rising exponent κ result from positive ISI correlations.

Stochastic adaptation is a mechanism effectively acting as colored noise (Ornstein-Uhlenbeck noise) that slowly modulates the ISIs and thus yields positive ISI correlations (Schwalger et al., 2010). As shown before, auditory receptors of locusts display spike-frequency adaptation on two time scales. The steady-state spike frequencies f_{∞_A} and f_{∞_B} which are the mean rates after the decay due to the fast and slow adaptation process (cf. Fig. 12.1), respectively, show that the slow adaptation process starts interfering primarily for sound intensities of the medium dynamic range (see Fig. 12.3D). For sound intensities close to the spike threshold, f_{∞_A} and f_{∞_B} overlap indicating that the spike response of the neuron in the lower dynamic range is mainly adapted by the fast adaptation current and not by the second adaptation process working on a slow time scale.

Stochastic adaptation can be split into a deterministic adaptation part and an Ornstein-Uhlenbeck noise with a correlation time τ^{OU} which is equal to the effective adaptation time constant τ_{eff} (see section 11.1, Schwalger et al., 2010). For a perfect integrate-and-fire model driven by one long-range correlated Ornstein-Uhlenbeck noise source, the Fano factor has been extensively analyzed and analytic expressions have been derived for the position of the minimum t_c^{min} as well as for $F(t_c)$ for small and large counting times, respectively (see Eq. (6.9)-(6.11), Middleton et al., 2003). The level of $F(t_c)$, at which the Fano factor curve saturates at large counting times, is approximately defined by the product of the correlation time τ^{OU} and the intensity D^{OU} of the Ornstein-Uhlenbeck noise (Eq. (6.13)). For moderate counting times t_c , Middleton et al. (2003) indicated that the Fano factor for the PIF model with colored noise driving is solely dependent on D^{OU} (Eq. (6.12)) and the exponent is defined by $\kappa = 1$ for the case that $t_c < \tau^{OU}$. A least-square fit of these two theoretical approximations, Eq. (6.12) and Eq. (6.13), show that the experimental Fano factor curves have an exponent $\kappa \neq 1$ and that κ rises from values close to 0.5 to approximately 1 with increasing sound intensity (see Fig. 12.3A,C). Furthermore, the data show that the correlation time constant for a sound intensity of the lower dynamic range has a value of $\tau^{OU} > 3$ s because a saturation of the Fano factor curve is not visible at $F(t_c) = D^{OU}\tau^{OU} = 2.25$ ($\tau^{OU} = \tau_{eff}$) where $t_c = 10$ s and $\tau^{OU} = 3$ s (see Fig. 12.3E). The Fano factor curve for a sound intensity of the upper dynamic range shows in the same way that $\tau^{OU} > 8.5$ s (see Fig. 12.3F). This time constant, however, is larger than the effective time constants τ_{eff} measured from the mean spike-frequency as a function of time (see Fig. 12.2) suggesting that the theory of the

PIF model with a single colored-noise source is not sufficient to explain the experimental data. Additionally, the fact that locust auditory receptor neurons show spike-frequency adaptation over two time scales indicate that the combination of two adaptation currents may shape the spike-count variability.

In the following section, we therefore simulate a second adaptation current or the combination of a fast and slow adaptation current which may explain (i) the experimentally observed Fano factor curves with changing κ and t_c^{min} for increasing sound intensities, and (ii) the fact that the analytical approximations of the PIF model with a single colored-noise source, where $\tau^{OU} = \tau_{eff}$, do not agree with the experimental data.

12.3 Locust auditory transduction model with two stochastic adaptation currents

In the previous chapter, we have shown that the ISI statistics, i.e. the ISI distributions and correlations, of locust receptor cell responses can be replicated by means of a mixed channel noise model where both fast channel noise and slow fluctuations caused by one population of stochastic adaptation channels are present (see section 11.3). This model, however, is not able to explain the spike-count statistics showing a shift of the Fano factor curves for different sound intensities and reaching high values $F(t_c)$ for large counting times for sound intensities of the upper dynamic range that elicit high spike frequencies (see Fig. 12.4A). The reason for the good agreement of the model to the ISI statistics of the experimental data is that a second adaptation current possessing a long time constant of several seconds has no additional significant influence on the ISI variability. This is in contrast to the spike-count variability quantified by the Fano factor, determined for different counting time frames up to several seconds, on which slow processes can have distinct effects (see e.g. Middleton et al., 2003). Since we have shown that (i) locust auditory receptor cells comprise spike-frequency adaptation mediated by two adaptation processes (see Fig. 12.1 and Fig. 12.2) and (ii) the experimental Fano factor curves suggest correlation time constants of several seconds which are larger than the measured effective adaptation time constants (see Fig. 12.3), we hypothesized a strong contribution of the slow adaptation process and furthermore a potential interaction with the fast adaptation process.

To this end, we first simulated the locust auditory transduction cascade with a single slow stochastic adaptation current I_B ($I_A = 0 \mu\text{A}/\text{cm}^2$). The relation between the original adaptation time constant, τ , and the effective one, τ_{eff} , is given by the relation of the slopes of the onset- and steady-state f-I curve (Benda and Herz, 2003). For the recorded auditory receptor neuron shown in Fig. 12.3, we yielded a scaling factor of approximately 3, i.e. $\tau \approx 3\tau_{eff}$, which gives us a time constant $\tau_B = 9\text{s}$ for the slow adaptation current. This time constant was used in the models of the auditory receptor neuron with slow adaptation currents.

The simulations showed that one population of slow stochastic adaptation channels

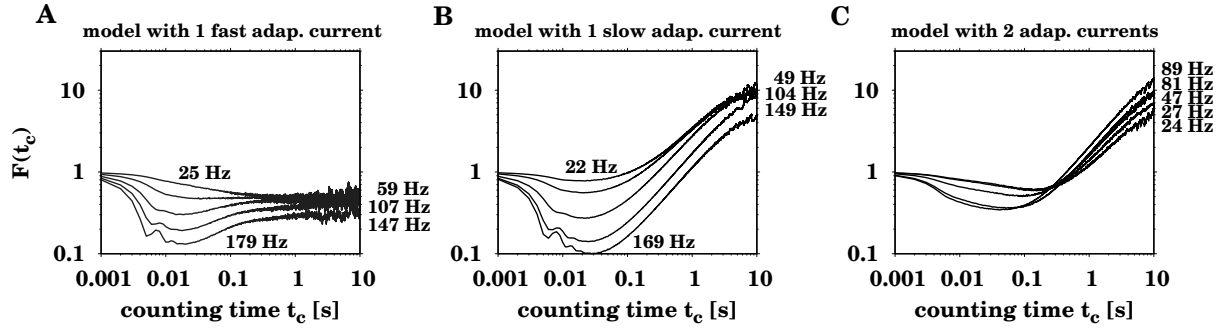


Figure 12.4: Fano factor curves of the locust auditory transduction model with one and two stochastic voltage-dependent adaptation currents. **A** Fano factor curves of the locust auditory transduction model with $N_R = 20$ stochastic receptor and $N_A = 600$ stochastic voltage-dependent adaptation channels with a fast adaptation time constant of 100 ms as used for Fig. 11.9D-F. The slow adaptation current was set to $I_B = 0 \mu\text{A}/\text{cm}^2$. **B** Fano factor curves of the locust auditory transduction model with $N_R = 20$ stochastic receptor and $N_B = 2000$ stochastic voltage-dependent adaptation channels with a slow adaptation time constant of 9 s. The fast adaptation current was set to $I_A = 0 \mu\text{A}/\text{cm}^2$. **C** Fano factor curves of the locust auditory transduction model with two stochastic voltage-dependent adaptation currents. We used $N_R = 2$ stochastic receptor and $N_A = 8000$ and $N_B = 500$ stochastic adaptation channels.

alone cannot explain the experimental Fano factor curves (see Fig. 12.4B). The resulting Fano factor curves shift approximately parallel to each other for increasing sound intensities evoking high spike frequencies. In addition, they show neither a shift of the minimal Fano factor position t_c^{min} to smaller counting times nor an increase of the Fano factor values, $F(t_c)$, for large counting times with increasing sound intensity.

We therefore simulated the locust auditory transduction model with two populations of stochastic adaptation currents I_A and I_B . The adaptation time constants were chosen as $\tau_A = 100 \text{ ms}$ and $\tau_B = 9 \text{ s}$ as observed from the experimental data. The model parameters were tuned so that the steady-state spike frequencies f_{∞_A} and f_{∞_B} correspond roughly to the ones of the auditory receptor cells (cf. Fig. 12.3D). The mixed channel noise model with two stochastic voltage-dependent adaptation currents can explain both the shift of t_c^{min} to smaller counting times and the change of the exponent κ for increasing sound intensities (Fig. 12.4C). For sound intensities of the lower dynamic range, these simulations, however, show Fano factor curves exhibiting higher levels of $F(t_c)$ for large counting times ($t_c = 10 \text{ s}$) compared to the experimental data (cf. Fig. 12.3A). The reason is that the voltage-dependent voltage-dependent adaptation currents are already strongly activated during stimulation with low sound intensities eliciting small spike frequencies f . The experimental data, however, show for these sound intensities no visible decay of the spike frequency by the slow adaptation process with a time constant of several seconds (cf. Fig. 12.3D). For $f < 40 \text{ Hz}$ the steady-state spike frequencies f_{∞_A} and f_{∞_B} are identical. This effect might be explained by currents passing slow calcium-dependent

potassium channels which only open if a sufficient amount of calcium ions has been accumulated.

To this end, we modeled the second slower adaptation current as slow calcium-dependent potassium currents mediating spike-frequency adaptation which are activated for spike frequencies approximately $f > 40\text{Hz}$ (see Fig. 12.5A). This model with a fast stochastic voltage-dependent and a slow stochastic calcium-dependent potassium current is able to explain both the ISI statistics (data not shown) and the spike-count statistics of locust auditory receptor cells (see Fig. 12.5B). With increasing sound intensity, the Fano factor curves show a shift of the position of their minimum t_c^{\min} to smaller counting times (see Fig. 12.5B,C) as well as an increase of both the Fano factor values and the exponent κ for large counting times (see Fig. 12.5B,D).

Two adaptation currents with time constants measured from step experiments can explain the spike-count variability of locust auditory receptor neurons quantified by the Fano factor. In the following chapter, we will analyze how the Fano factor is influenced

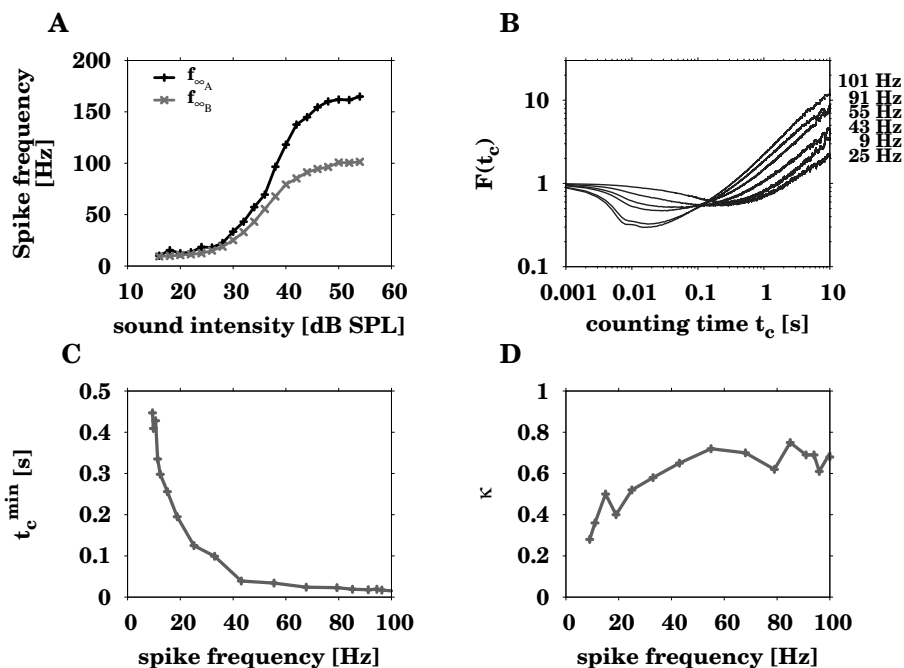


Figure 12.5: Fano factor curves of the locust auditory transduction model with one fast stochastic M-type and one slow stochastic calcium-dependent potassium currents. **A** The steady-state spike frequencies $f_{\infty A}$ and $f_{\infty B}$ and **B** the Fano factor curves of the locust auditory transduction model with a fast stochastic M-type and a slow stochastic calcium-dependent potassium current. We used $N_R = 20$ stochastic receptor and $N_A = 600$ M-type stochastic adaptation channels and a colored noise intensity $D_{Ca} = 0.01$ for the slow stochastic calcium-dependent potassium current. **C, D** The counting time of the Fano factor minimum t_c^{\min} (**C**) and the exponent κ (**D**, cf. Eq. (6.12)) as a function of spike frequency.

12.3 Locust auditory transduction model with two stochastic adaptation currents 83

by two adaptation currents and if a potential interaction of the two processes may shape the spike-count variability.

How do two time scales of adaptation shape the spike-count variability?

Spike-frequency adaptation can act on different time scales from a few tens or hundreds of milliseconds (Benda et al., 2005; Peron and Gabbiani, 2009a) to several seconds (Pollack, 1988; Sobel and Tank, 1994). Neurons, however, are not restricted to spike-frequency adaptation on a single time scale. A variety of neurons exist which exhibit multiple time scales of adaptation as response to sensory stimuli. Examples can be found on both the level of primary receptors and cortical neurons of the visual system (Fairhall et al., 2001a,b; Baccus and Meister, 2002), electrosensory system (Xu et al., 1996; Nelson et al., 1997), motor system (French, 1987, 1989; Spain et al., 1991a,b; Sawczuk et al., 1995, 1997) and auditory system (Nelken et al., 2003; Ulanovsky et al., 2004; Wimmer et al., 2008).

In the previous chapter, we have shown that the primary auditory receptor neurons of *Locusta migratoria* exhibit spike-frequency adaptation at least on two time scales. Furthermore, we have demonstrated that a model of the auditory transduction cascade with two stochastic adaptation currents is able to explain both the interspike-interval and spike-count variability observed in neuronal responses of locust auditory receptor neurons.

In this chapter, we analyze how two stochastic adaptation currents shape the spike-count variability. We first analyze the Fano factor for a perfect integrate-and-fire model with one and two colored noise sources since stochastic adaptation effectively acts as colored noise (Schwalger et al., 2010). Furthermore, we derive analytical approximations for the Fano factor for small, moderate and large counting times as well as for the position of the Fano factor minimum.

Additionally, we analyze both the Fano factor and the dynamics of a perfect integrate-and-fire and a Hodgkin-Huxley-type model with two adaptation currents. We show that two adaptation currents shape the spike-count variability by mutual interaction which we verify by means of a phenomenological firing-rate model with two currents mediating spike-frequency adaptation.

13.1 Spike-count variability in models with two adaptation currents

We first analyze the spike-count variability quantified by the Fano factor in perfect integrate-and-fire models. We analyze the Fano factor curves of PIF models with one and two colored noise sources and compare them to PIF models with two stochastic adaptation currents. Furthermore, we validate the results in more realistic single-compartment conductance-based models with spike-frequency adaptation.

13.1.1 PIF model driven by colored noise

Stochastic adaptation effectively acts as colored noise (Ornstein-Uhlenbeck noise, Schwalger et al., 2010). For a perfect integrate-and-fire model driven by a single Ornstein-Uhlenbeck (OU) noise source, whose dynamics are given by Eq. (9.1)-(9.2), analytic expressions for the Fano factor have been derived for small and large counting times, F_{small} and F_{large} , as well as for the position t_c^{min} where the Fano factor curve exhibits a minimum due to the effect of positive ISI correlations (see Eq. (6.9)-(6.11), Middleton et al., 2003). In this model, the exponent of the Fano factor curve for moderate counting times, Eq. (6.12), is given by $\kappa = 1$ if $t_c < \tau^{OU}$. For fast correlation time constants close to t_c^{min} , however, the exponent $\kappa = 1$ is not visible in the Fano factor curves because the curve already begins to saturate for $t_c^{min} < t_c < t_c^{sat}$ (see Fig. 13.1, t_c^{sat} : counting time for which $F(t_c)$ starts saturating). A colored noise source with a correlation time constant of a hundred milliseconds, for instance, results in an apparent exponent κ much smaller than one, whereas for correlation time constants of several seconds the linear part is clearly visible.

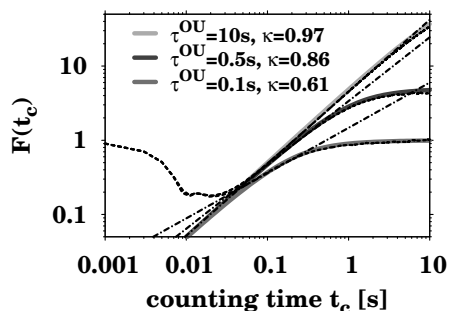


Figure 13.1: The exponent κ for different correlation time constants. Fano factor curves of a PIF model driven by a single Ornstein-Uhlenbeck noise source for three different correlation time constants τ^{OU} as indicated (black dotted lines). The current μ driving this model (and also the ones used for the following figures) was chosen to result in a firing rate of 100 Hz. The dashed-dotted lines are the theoretical curves for the Fano factor at moderate counting times $t_c^{min} < t_c < t_c^{sat}$ (cf. Eq. (6.12)). The different gray solid lines are the theoretical curves for $F_{large}(t_c)$ derived by Middleton et al. (2003) (Eq. (6.10)).

The dynamics of the membrane voltage of the PIF model with a noisy current driving the model is equivalent to a random walk model (Gerstein and Mandelbrot, 1964). If we increment the spike threshold by v_{th} each time the membrane voltage reaches it instead of resetting the voltage, the dynamics of the PIF model with OU noise (Eq. (9.1)-(9.2)) is equivalent to a Brownian motion with positive drift. The parameters $v(t)$ and $\mu + w_A(t)$ can, hence, be regarded as the position and the velocity of particles, respectively, with a positive bias $\mu > 0$.

The same concept of Brownian motion of particles can be applied to an integrate-and-fire model with more than one dimension. The dynamics of a PIF model with two independent driving colored-noise sources (Eq. (9.3)-(9.5)) can be mapped to a two-dimensional biased Brownian motion with positive drift (Risken, 1996; Middleton et al., 2003). As long as the two noise sources are independent, the variance of the position $x(t)$ of the motion starting at time $t = 0$, where $x(t) = x_0$, is defined by the sum of the motion variances for the one-dimensional case of each individual colored noise source. The Fano factor for Brownian motion at time t is equivalent to the ratio of the variance and the mean drift. The variance in the larger time limit is given by the mean-squared displacement (MSD) for a Brownian motion (Risken, 1996):

$$\langle (x(t) - x_0)^2 \rangle = \sum_{i=0}^n \langle (x_i(t) - x_i(0))^2 \rangle \quad (13.1)$$

$$= \sum_{i=0}^n \frac{2kT\tau_i t}{m_i} \left(1 - \frac{\tau_i}{t} (1 - e^{-t/\tau_i})\right) \quad (13.2)$$

where k is the Boltzmann constant, T is the temperature, m_i is the mass and τ_i is the relaxation time of the velocity of the i^{th} dimension.

In a PIF model, the position of the Brownian motion $x(t)$ corresponds to the evolving membrane potential $v(t)$. For a PIF model with multiple independent colored noise sources, the Fano factor (Eq. (6.7)) of the spike count for large counting times t_c is defined by the variance (Eq. (13.2)) divided by the drift $\mu t / v_{th}$. The variance of the Brownian motion is divided by v_{th}^2 to achieve the variance of the spike count. Identifying $D_i^{OU} \cong kT / m_i$, $\tau_i^{OU} \cong \tau_i$, and $t_c \cong t$ results in:

$$F_{large}(t_c) = \frac{2}{v_{th}\mu} \sum_{i=0}^n D_i^{OU} \tau_i^{OU} \left[1 - \frac{\tau_i^{OU}}{t_c} (1 - \exp^{-t_c/\tau_i^{OU}}) \right]. \quad (13.3)$$

For moderate counting times $t_c < \tau_{i=0}^{OU}$, where $\tau_{i=0}^{OU}$ is the fastest time constant, the Fano factor is given by

$$F_{mod}(t_c) = \frac{1}{v_{th}\mu} \sum_{i=0}^n D_i^{OU} t_c. \quad (13.4)$$

Since the Fano factor for small counting times is independent of the noise, F_{small} is given by Eq. (6.9). The position of t_c^{min} can be determined by solving the differential equation

$$\frac{d}{dt} [F_{small}(t_c) + F_{large}(t_c)] = 0. \quad (13.5)$$

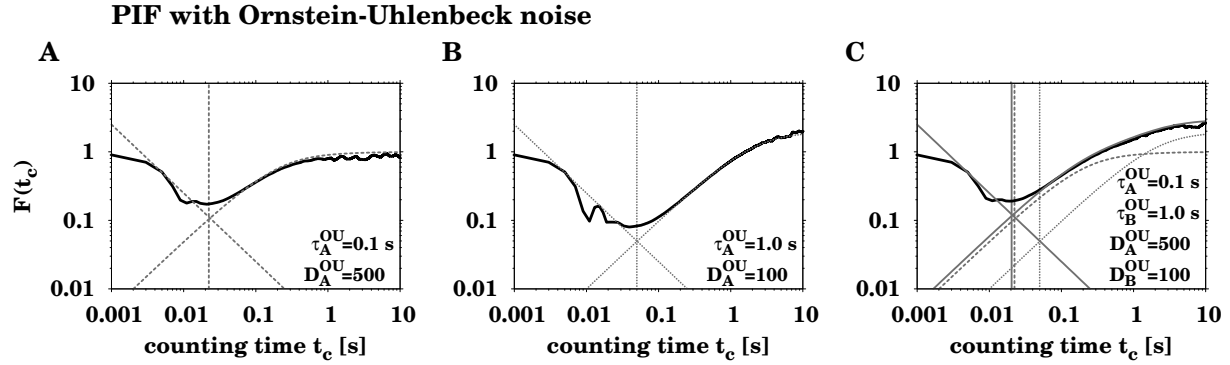


Figure 13.2: Fano factor curves of a PIF model driven by Ornstein-Uhlenbeck (OU) noise. **A,B** Fano factor curves (black lines) of a PIF model with a single OU noise source (Eq. (9.1)-(9.2)) and the theoretical approximations (dashed gray lines) F_{small} (Eq. (6.9)), F_{large} (Eq. (6.10)) and t_c^{min} (Eq. (6.11)) derived by Middleton et al. (2003) for the correlation time constants τ_A^{OU} and noise intensities D_A^{OU} as indicated. **C** Fano factor curve (black line) of a PIF model with both OU noise sources from A and B combined (Eq. (9.3)-(9.5)). The dashed gray lines are the same theoretical approximations as shown in A and B. The solid gray lines are the theoretical approximations F_{small} (Eq. (6.9)), F_{large} (Eq. (13.3)) and t_c^{min} (Eq. (13.6)) for a PIF model with n OU noise sources.

The approximate position of the minimum of the Fano factor is then given by:

$$t_c^{min} \approx \frac{v_{th}}{2\sqrt{\sum_{i=0}^n D_i^{OU}}} . \quad (13.6)$$

Fano factor curves of a PIF model with two independent OU noise sources show that the two individual noise sources shape the curves mainly in the counting time regime corresponding to their noise correlation times (see Fig. 13.2). The colored-noise source with the faster correlation time constant τ_A^{OU} primarily influences the position of the minimum t_c^{min} and the onset of the rising part of F_{large} (see Fig. 13.2A,C) while the saturation of the Fano factor curve is mainly determined by the process exhibiting the slower correlation time constant τ_B^{OU} (see Fig. 13.2B,C). Since F_{small} does not depend on the OU noise intensity and correlation time constant, the Fano factors for small counting times are identical independent of the number of noise sources and their characteristics.

For the PIF model with a single colored-noise source, the Fano factor rises for moderate counting times only with an apparent exponent $\kappa = 1$ if $\tau^{OU} \gg t_c^{min}$ (see Fig. 13.1). The same holds true for the PIF model driven by two colored-noise sources if $\tau_A^{OU} \gg t_c^{min}$ (see Fig. 13.3). Thus, the increase of the Fano factor curve for moderate counting times is dependent on both the noise intensities and time constants of the adaptation processes.

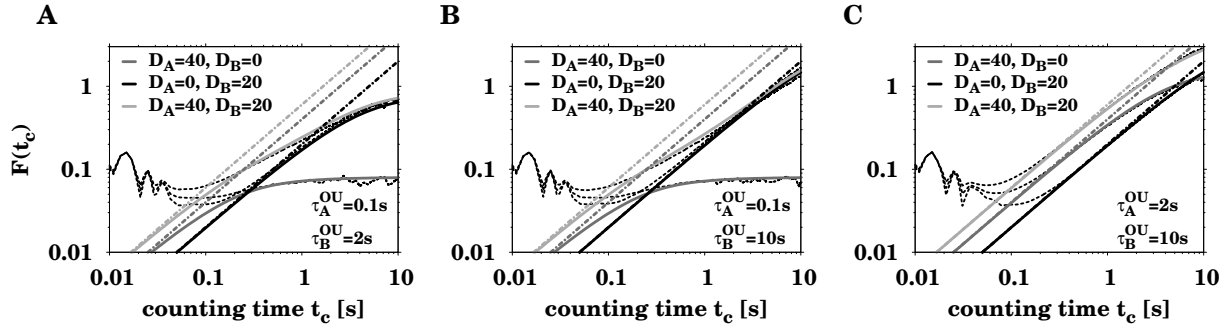


Figure 13.3: The exponent κ for different correlation time constants of one vs. two Ornstein-Uhlenbeck noise sources. Fano factor curves of a PIF model with one ($D_A = 0$ or $D_B = 0$) or two ($D_A \neq 0$ and $D_B \neq 0$) colored noise sources (black dashed lines) and the respective theoretical approximations $F_{mod}(t_c)$ for moderate counting times (Eq. (13.4), different gray dashed-dotted lines) and $F_{large}(t_c)$ for large counting times (Eq. (13.3), different gray solid lines). The noise intensities (D_A, D_B) were changed while the respective correlation time constants τ^{OU} were kept constant (as indicated).

13.1.2 PIF model with adaptation currents

Stochastic adaptation does effectively act as colored noise (Schwalger et al., 2010), but in contrast to colored noise is voltage-dependent and hence correlated with the firing rate. Thus, the assumption about independent noise processes previously made for a PIF with colored noise (see section 13.1.1) does not apply for a PIF with adaptation currents.

The dynamics of a PIF model with a single adaptation current are given by Eq. (9.6)-(9.7). The Fano factor for small and large counting times, F_{small} and F_{large} , as well as the position of the Fano factor minimum, t_c^{min} , can be determined by Eq. (6.9)-(6.11) using the scaled effective parameters derived by Schwalger et al. (2010):

$$\tilde{\mu} = \lambda\mu \quad (13.7)$$

$$\tilde{D} = \lambda D\alpha^2 \quad (13.8)$$

$$\tilde{\tau}_A = \lambda\tau_A \quad (13.9)$$

with the scaling factor $\lambda = (1 + \alpha\tau_A(\Delta w_A/v_{th}))^{-1}$ (cf. section 9.1). The analytic expressions for the Fano factor hence read:

$$F_{small}(t_c) \approx \frac{v_{th}}{4\lambda\mu t_c} \quad (13.10)$$

$$F_{large}(t_c) = \frac{2\lambda D\alpha^2\tau_A}{v_{th}\mu} \left[1 - \frac{\lambda\tau_A}{t_c} (1 - \exp^{-t_c/(\lambda\tau_A)}) \right] \quad (13.11)$$

$$t_c^{min} \approx \frac{v_{th}}{2\sqrt{\lambda D\alpha^2}}. \quad (13.12)$$

Examples of Fano factor curves of the PIF model with one and two stochastic adaptation currents are shown in Fig. 13.4. Similar to the PIF model with colored noise, the

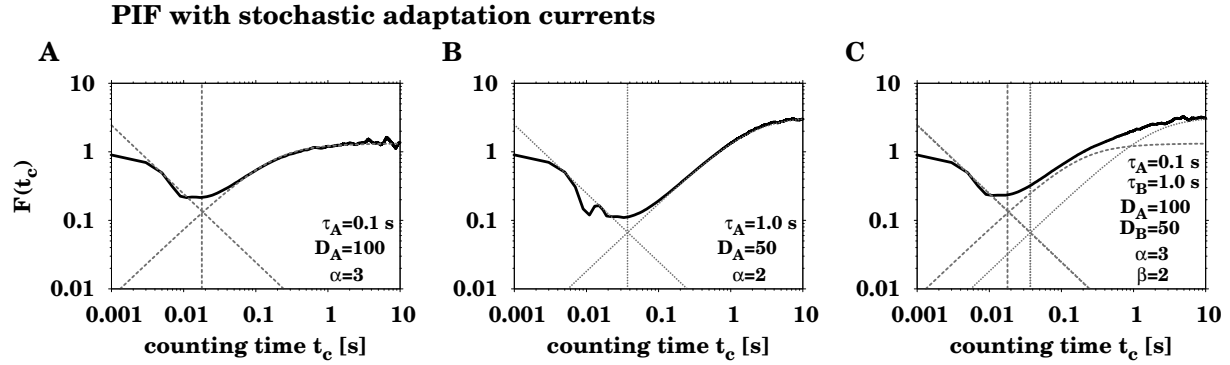


Figure 13.4: Fano factor curves of a PIF model with stochastic adaptation currents. **A,B** Fano factor curves (black lines) of a PIF model with a single stochastic adaptation current (Eq. (9.6)-(9.7)) and the theoretical approximations (dashed gray lines) F_{small} (Eq. (13.10)), F_{large} (Eq. (13.11)) and t_c^{min} (Eq. (13.12)) for different adaptation time constants τ and noise intensities D_A as indicated. **C** Fano factor curve (black line) of a PIF model with both adaptation currents from A and B combined (Eq. (9.8)-(9.10)). The dashed gray lines are the same theoretical approximations shown in A and B.

Fano factor curve of the PIF model with two adaptation currents shows a major impact of the adaptation currents on the Fano factor values in the counting time regime that corresponds to their adaptation time constants. The adaptation current with the fast decay time constant τ_A primarily influences the position of the minimum t_c^{min} and the onset of the rising part of F_{large} (see Fig. 13.4A,C). The saturation of the Fano factor curve, in contrast, is mainly determined by the adaptation current with the slower time constant τ_B (see Fig. 13.4B,C). F_{small} is independent of the noise sources and hence identical for small counting times for all settings.

All parameters of the adaptation currents, i.e. adaptation time constant, noise intensity and strength, affect the shape of the Fano factor curves (see Fig. 13.5). For a PIF model with a fast and a slow adaptation current, an increasing noise intensity D_A of the fast adaptation current shifts the Fano factor minimum both to higher $F(t_c)$ values and to smaller counting times (see Fig. 13.5A). The noise intensity D_B of the slow adaptation process, on the other hand, shapes mainly the Fano factors for large counting times and determines the position where the Fano factor curve saturates (see Fig. 13.5B): The larger D_B , the higher $F(t_c)$ in its saturation. If the slow adaptation current is deterministic ($D_B = 0$), the Fano factor decreases for large counting times. This is caused by a major impact of negative ISI correlations in the large counting time regime as a result of deterministic adaptation (cf. Eq. (6.8), Schwalger et al., 2010). Increasing adaptation strength α of the fast adaptation current raises the Fano factor minimum to higher $F(t_c^{min})$ values and slightly decreases $F(t_c)$ in the saturating curve part (see Fig. 13.5C). In contrast, raising strength β of the slow adaptation current increases $F(t_c)$ both at the minimal position t_c^{min} and at the saturation (see Fig. 13.5D). Likewise as for the model with colored noise, the position of t_c^{min} is independent of the adaptation time constant τ_A or τ_B . The

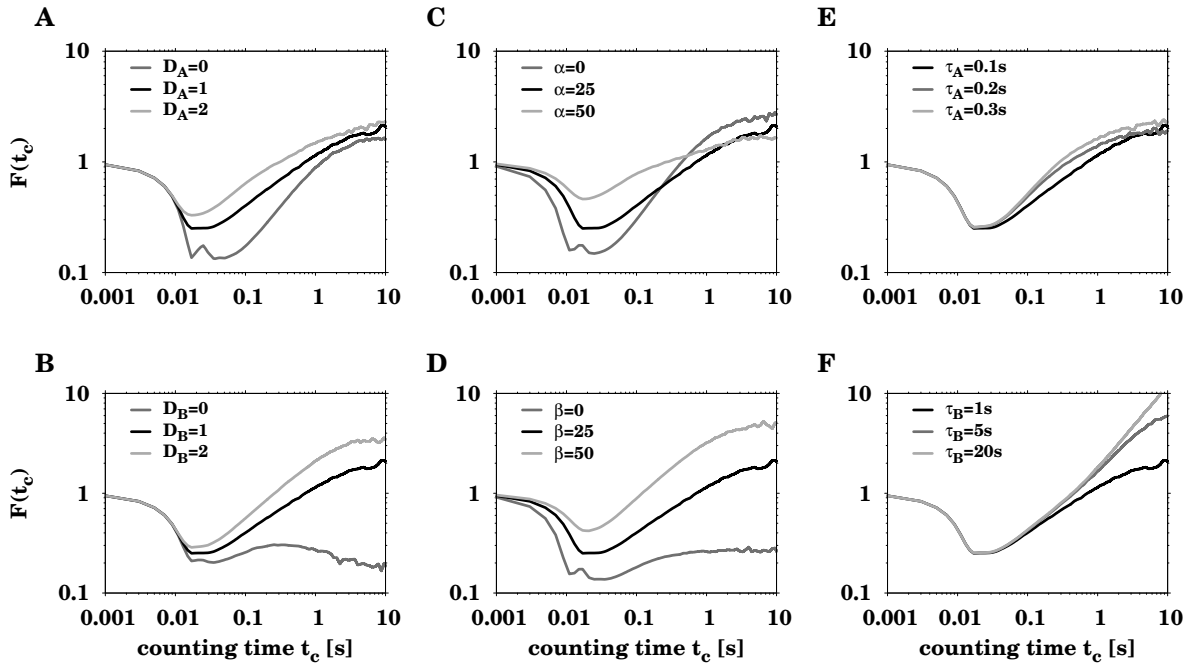


Figure 13.5: Effect of adaptation strength, noise intensity and time constant on the Fano factor curve. Fano factor curves for a PIF model with two stochastic adaptation currents A and B (Eq. (9.8)-(9.10)) reducing the spike-frequency with a short and long adaptation time constant τ_A and τ_B . In each panel one parameter of the model was changed (as indicated) while the others were kept constant. The black lines indicate Fano factor curves for the PIF model with identical parameters ($D_A = 1, D_B = 1, \alpha = 25, \beta = 25, \tau_A = 0.1 \text{ s}, \tau_B = 1 \text{ s}$). D_A, D_B : noise intensity of the adaptation currents A and B ; α, β : adaptation strengths of the adaptation currents A and B .

decay time τ_A of the fast adaptation current has only a slight impact on the Fano factor values in the medium counting time regime (see Fig. 13.5E). The time constant τ_B of the slow adaptation current, in contrast, determines the position, where the Fano factor curve saturates, and the saturation level (see Fig. 13.5F).

13.1.3 Interaction of two adaptation currents

The main difference between a perfect integrate-and-fire model with two colored noise sources and one with two adaptation currents, effectively acting as colored noise, is that a deterministic adaptation current with noise intensity $D_A = 0$ still can influence the spike-count variability in the latter model (see Fig. 13.6A-C).

The dynamics of the adaptation variables w_A and w_B (Eq. (9.9)-(9.10)) are dependent on the occurrence of an action potential. The time constant of an adaptation current determines how fast adaptation currents are accumulated. Hence, adaptation with a fast time constant can react more rapidly on a change of the firing rate in comparison to slow adaptation currents. This can be seen in a simulation of a PIF model with one fast

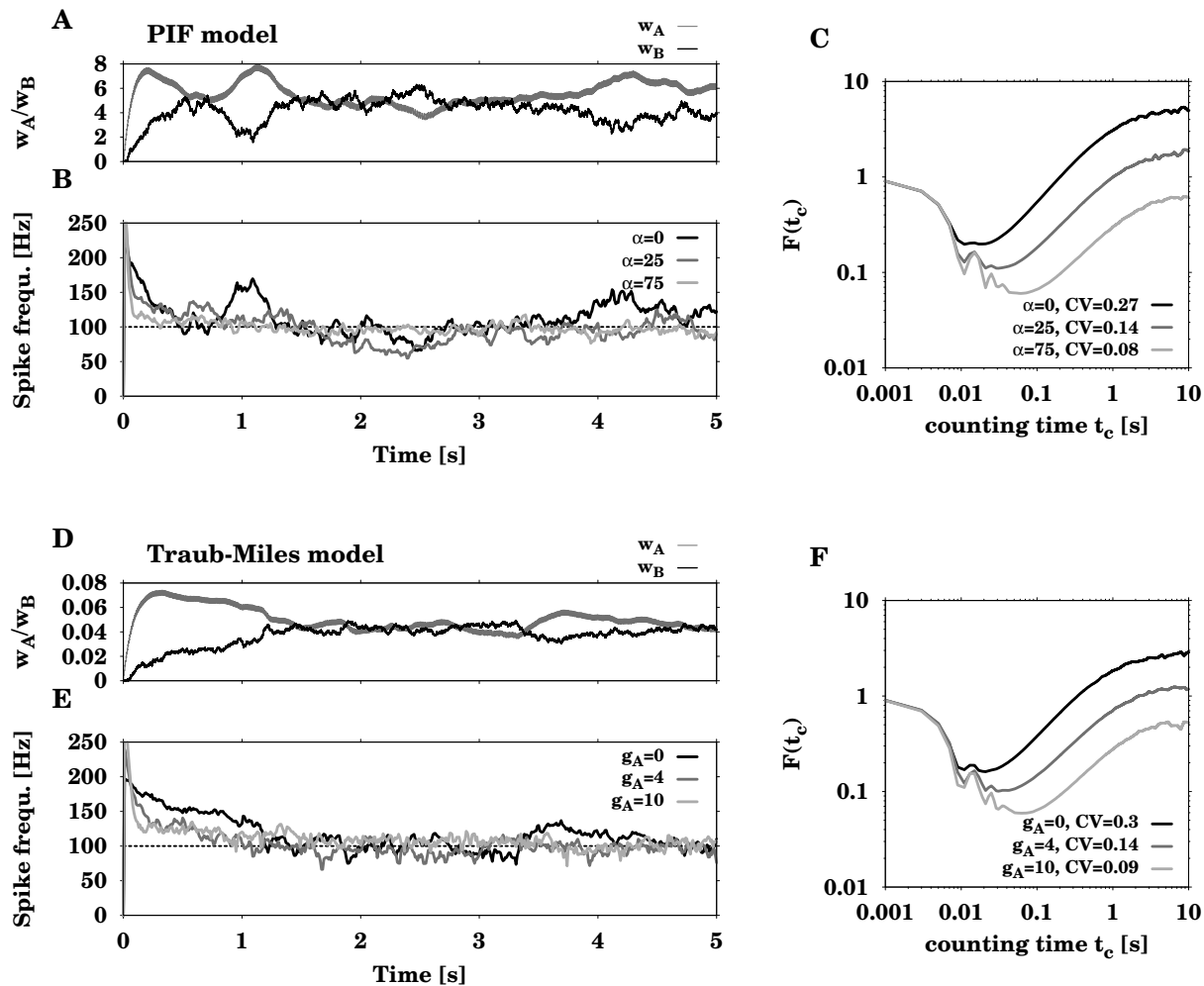


Figure 13.6: Two adaptation currents counteract and affect the ISI and spike-count variability. **A-C** PIF model (Eq. (9.8)-(9.10)) with one fast deterministic ($D_A = 0$, $\tau_A = 0.1s$) for three different adaptation strength α as indicated and one slow stochastic adaptation current ($D_B = 2$, $\beta = 25$, $\tau_B = 1s$). **A** Adaptation variables w_A and w_B over time ($\alpha = 0$). **B** Mean spike frequency of one trial over time for three different strengths α of the deterministic adaptation current as indicated. **C** Fano factor curves for the model with the three different adaptation strengths shown in B. **D-F** Traub-Miles model (Eq. (9.11)) with one fast deterministic ($D_A = 0$, $\tau_A = 0.1s$) for three different conductances g_A in mS/cm^2 as indicated and one slow stochastic adaptation current ($D_B = 0.00006$, $g_B = 5$, $\tau_B = 1s$). **D** Adaptation variables w_A and w_B over time ($g_A = 0$). **E** Mean spike frequency of one trial over time for three different conductances g_A of the deterministic adaptation current as indicated. **F** Fano factor curves for the model with the three different adaptation strengths shown in E.

deterministic and one slow stochastic adaptation current (see Fig. 13.6A,B). A random decline of the adaptation variable w_B of the slow stochastic adaptation current leads to a degrading adaptation current and thus to an increase of the spike frequency. As a result, the activation variable w_A of the fast adaptation current increases and reduces spike

frequency again. This demonstrates that fast and slow adaptation currents counteract. If w_B decreases, the firing rate and hence w_A rises (see Fig. 13.6A) which in turn decreases the rate. By means of this antagonistic behavior, a fast adaptation current is able to regularize spike-response variability (see Fig. 13.6A-C). An increase of the adaptation strength α of the fast adaptation current amplifies the countervailing action and reduces the variability of the mean spike frequency (see Fig. 13.6B). Thus, both interspike-interval as well as spike-count variability quantified by the CV and the Fano factor, respectively, decline with increasing α (see Fig. 13.6C). These observations do not only apply for a simple adapting perfect integrate-and-fire model but are also valid for a more realistic conductance-based Traub-Miles model with a fast deterministic and a slow stochastic current mediating spike-frequency adaptation (see Fig. 13.6D-F).

The same counteracting behavior is observed for a PIF and Traub-Miles model with two stochastic adaptation currents (see Fig. 13.7A). In these models, however, a rise of the adaptation strength (α or g_A) of the fast stochastic adaptation current results in an increase of the coefficient of variation (see Fig. 13.7B,C). The Fano factor, though, is only increased for medium counting times while the values for large counting times are still reduced. The rise of the adaptation strength (β or g_B) of the slow stochastic adaptation current, in contrast, yields an increase of both the CV and the Fano factor for all counting times.

In models with a fast stochastic and a slow deterministic adaptation current, the counteraction of the two currents is less pronounced because the deterministic current is too slow to react on the fast random changes of the stochastic current (Fig. 13.8A). In simulations of the PIF model, an increase of the strength β of the slow adaptation current has no significant effect on the ISI variability quantified by the CV (Fig. 13.8B). Nevertheless, the spike-count variability is decreased at large counting times. For this combination of adaptation currents, the Traub-Miles model shows slightly different results (Fig. 13.8C). Here, the variability at medium counting times is additionally slightly increased. This leads to increasing CVs and a rising Fano factor minimum for increasing g_B , while the Fano factor for large counting times is similarly reduced as for the PIF model. It is, however, unclear what the reason is for this discrepancy between the models.

13.2 Firing-rate models for spike-frequency adaptation with two adaptation currents

Simulations of both perfect integrate-and-fire and Hodgkin-Huxley-type models with spike-frequency adaptation on two time scales suggest an interaction of two adaptation currents. To gain more insight into the dynamics and interaction of adaptation currents, we theoretically analyze a phenomenological firing-rate model for spike-frequency adaptation on two time scales. Moreover, we derive equations which can be used to estimate the adaptation properties, i.e. adaptation strengths and time constants, from

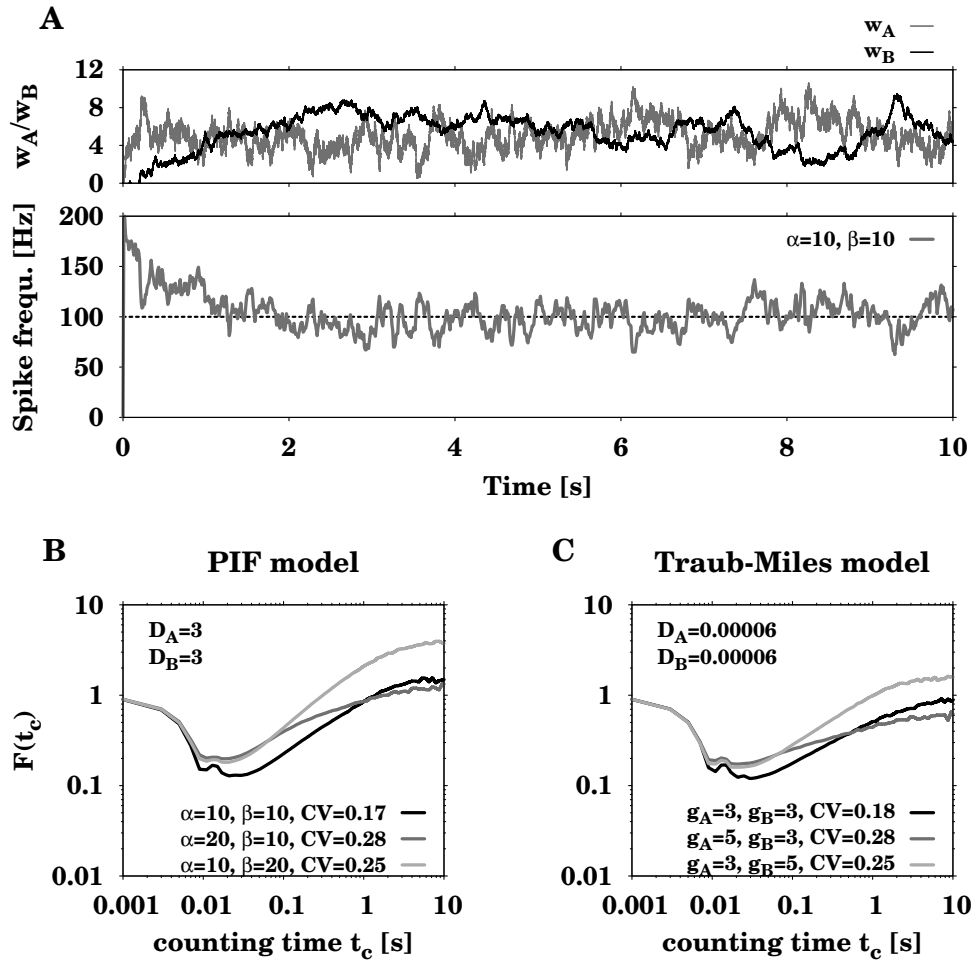


Figure 13.7: Variability in a PIF and Traub-Miles model with two stochastic adaptation currents. **A** The adaptation variables w_A and w_B (top) and the mean spike frequency of one trial (bottom) of the PIF model as a function of time ($D_A = 3$, $D_B = 3$, $\alpha = 10$, $\beta = 10$, $\tau_A = 0.1$ s, $\tau_B = 1$ s). **B,C** The Fano factor curves for the PIF and Traub-Miles model. In both models the noise intensities, D_A and D_B , of both adaptation currents were kept constant while the adaptation strengths, α and β , were changed (parameters as indicated, τ_A and τ_B as in A).

experimentally measured spike responses.

A firing-rate model for spike-frequency adaptation mediated by a single adaptation current has been derived by Benda and Herz (2003). The dynamics of this model are given by

$$f = c(I - A) \quad (13.13)$$

$$\tau_A \dot{A} = \alpha f - A \quad (13.14)$$

where $f_0 = cI$ is the linearized onset f-I curve with the onset gain c and input current I . The adaptation state A decays with the adaptation time constant τ_A and is driven by αf

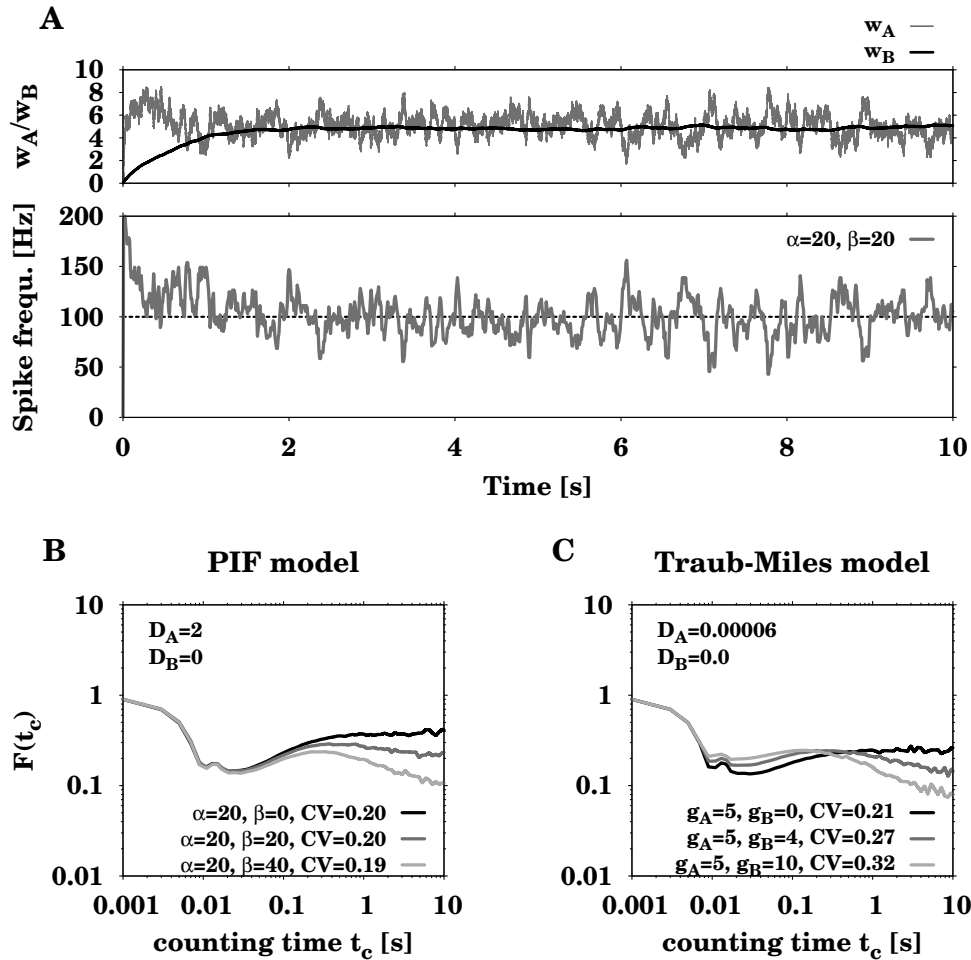


Figure 13.8: Variability in a PIF and Traub-Miles model with one fast stochastic and one slow deterministic adaptation current. **A** The adaptation variables w_A and w_B (top) and the mean spike frequency of one trial (bottom) of the PIF model as a function of time ($D_A = 2, D_B = 0, \alpha = 20, \beta = 20, \tau_A = 0.1$ s, $\tau_B = 1$ s). **B,C** The Fano factor curves for the PIF and Traub-Miles model. In both models, the noise intensity D_A as well as the adaptation strength α and conductance g_A , respectively, of the fast stochastic adaptation current were kept constant while the adaptation strength β and conductance g_B , respectively, of the slow deterministic adaptation current ($D_B = 0$) were changed (parameters as indicated, τ_A and τ_B as in A).

where α is the adaptation strength.

Substituting the spike frequency f , Eq. (13.13), into Eq. (13.14) gives us the effective time constant $\tau_A^{eff} = \tau_A / (\alpha c + 1)$. The effective time constant τ_A^{eff} is the time constant which can be measured by fitting an exponential function to the mean spike frequency (cf. Fig. 12.1 and Fig. 12.2). In general, the two time constants τ_A and τ_A^{eff} differ (Benda and Herz, 2003). The main reason for that is that the strength of the spike-frequency adaptation is driven by αf (see Eq. (13.14)). Thus, the adaptation strength is dependent

on the actual spike frequency.

In the following, we expand this phenomenological firing-rate model by a second adaptation current and analyze its dynamics.

13.2.1 Linear adaptation model

Expanding the formalism by Benda and Herz (2003) by a second adaptation current yields a firing-rate model for spike-frequency adaptation which is given by:

$$f = c(I - A - B) \quad (13.15)$$

$$\tau_A \dot{A} = \alpha f - A \quad (13.16)$$

$$\tau_B \dot{B} = \beta f - B. \quad (13.17)$$

The adaptation states A and B decay with the corresponding adaptation time constants τ_A and τ_B . The adaptation strengths are given by α and β . The onset spike-frequency is defined by $f_0(I) = cI$ where I is the input current, $A = B = 0$, and where c is a constant defining the slope of the onset f-I curve ($c = f'_0(I)$). In this model, we assume both a linear onset f-I curve and a linear adaptation αf and βf . The subtractive effect of the adaptation currents A and B results in a shift of the neuron's f-I curve in the direction of higher input currents. Substituting f , Eq. (13.15), into Eq. (13.16) - (13.17) yields:

$$\tau_A \dot{A} = (-\alpha c - 1)A - \alpha c B + \alpha c I \quad (13.18)$$

$$\tau_B \dot{B} = -\beta c A - (\beta c + 1)B + \beta c I. \quad (13.19)$$

We can rewrite these equations in matrix form:

$$\begin{pmatrix} \dot{A} \\ \dot{B} \end{pmatrix} = \begin{pmatrix} \frac{-\alpha c - 1}{\tau_A} & \frac{-\alpha c}{\tau_A} \\ \frac{-\beta c}{\tau_B} & \frac{-\beta c - 1}{\tau_B} \end{pmatrix} \begin{pmatrix} A \\ B \end{pmatrix} + \begin{pmatrix} \frac{\alpha c I}{\tau_A} \\ \frac{\beta c I}{\tau_B} \end{pmatrix}. \quad (13.20)$$

The matrix has the eigenvalues

$$\lambda_1 = \frac{1}{2\tau_A\tau_B} (-\tau_A(\beta c + 1) - \tau_B(\alpha c + 1) - w) \quad (13.21a)$$

$$\lambda_2 = \frac{1}{2\tau_A\tau_B} (-\tau_A(\beta c + 1) - \tau_B(\alpha c + 1) + w) \quad (13.21b)$$

and the corresponding eigenvectors

$$\vec{v}_1 = \begin{pmatrix} \tau_B(\alpha c + 1) - \tau_A(\beta c + 1) + w \\ 2\beta c \tau_A \end{pmatrix} \quad (13.22a)$$

$$\vec{v}_2 = \begin{pmatrix} \tau_B(\alpha c + 1) - \tau_A(\beta c + 1) - w \\ 2\beta c \tau_A \end{pmatrix} \quad (13.22b)$$

where $w = \sqrt{\tau_A^2(\beta c + 1)^2 + \tau_B^2(\alpha c + 1)^2 + 2\tau_A\tau_B(\alpha\beta c^2 - \beta c - \alpha c - 1)}$.

The spike frequency as a function of time of the linear firing-rate model with two adaptation currents is determined by the sum of the adaptation variables A and B (see Fig. 13.9). The evolution of A and B over time can be described by means of the eigenvalues $\lambda_{1,2}$, Eq. (13.21), and eigenvectors $\vec{v}_{1,2}$, Eq. (13.22):

$$\begin{pmatrix} A(t) \\ B(t) \end{pmatrix} = k_1\vec{v}_1e^{\lambda_1 t} + k_2\vec{v}_2e^{\lambda_2 t} + \begin{pmatrix} A_\infty(t) \\ B_\infty(t) \end{pmatrix} \quad (13.23)$$

where $A_\infty = \alpha c I / (\alpha c + \beta c + 1)$, $B_\infty = \beta c I / (\alpha c + \beta c + 1)$, and where $k_{1,2}$ are constants (see Fig. 13.9 top – dashed lines). Substituting A and B in Eq. (13.15) by $A(t)$ and $B(t)$ of Eq. (13.23) gives us then:

$$f(t) = -ck_1\tilde{v}_1e^{\lambda_1 t} - ck_2\tilde{v}_2e^{\lambda_2 t} + c(I - A_\infty - B_\infty) \quad (13.24)$$

where $\tilde{v}_1 = \vec{v}_{1_1} + \vec{v}_{1_2}$ and $\tilde{v}_2 = \vec{v}_{2_1} + \vec{v}_{2_2}$ are the sums of the eigenvector elements. The function $f(t)$ describes the spike-frequency which decays over time t due to the adaptation processes A and B (see Fig. 13.9 bottom). The fast adaptation variable A first increases rapidly with $-\lambda_1^{-1}$ and declines then with a slower time constant given by $-\lambda_2^{-1}$ to its steady-state (see Fig. 13.9 top – dashed lines). The final decline results from the rise of the slower adaptation variable B which slowly increases to its steady-state exceeding the one of the fast adaptation variable. $-\lambda_1^{-1}$ and $-\lambda_2^{-1}$ are also the two time constants determining the decay of f in response to a step stimulus. Each of the eigenvalues λ_1 and λ_2 depend on both adaptation time constants τ_A and τ_B (see Eq. (13.21)). This again reflects the interaction of both adaptation processes which is confirmed by the previously described simulations of a PIF and Traub-Miles model with two adaptation currents.

Before we will describe in the following how we can deduce the adaptation strengths and time constants from experimentally measured spike responses, we will first have a closer look on the effective time constants τ_{eff} of the model with one (Eqs. (13.13)-(13.14)) and two adaptation currents (Eqs. (13.15)-(13.17)). To test if it was valid in chapter 10 to analyze the effect of the fast adaptation current on the interspike-interval variability without considering a potential interaction of a slower adaptation process, we compared the effective time constants of the two models for different adaptation properties (see Fig. 13.10). Varying the adaptation strength of the fast adaptation current (defined by αc) yields effective time constants of the fast process which are comparable for both models, thus $-\lambda_1^{-1} = \tau_A^{eff}$ (Fig. 13.10A). The same is true when we change the adaptation strength of the slow adaptation process (defined by βc , Fig. 13.10B). Varying the adaptation time constants τ_A or τ_B shows that the effective time constants of both models, i.e. τ_A^{eff} and $-\lambda_1^{-1}$, are comparable when $\tau_B \gg \tau_A$ (Fig. 13.10C,D). And this is the case for locust auditory receptor neurons whose spike responses show adaptation over two time scales in the range of a hundred milliseconds and several seconds. The effective time constants of the slow adaptation process, however, differ for both models ($-\lambda_2^{-1} \neq \tau_B^{eff}$) showing

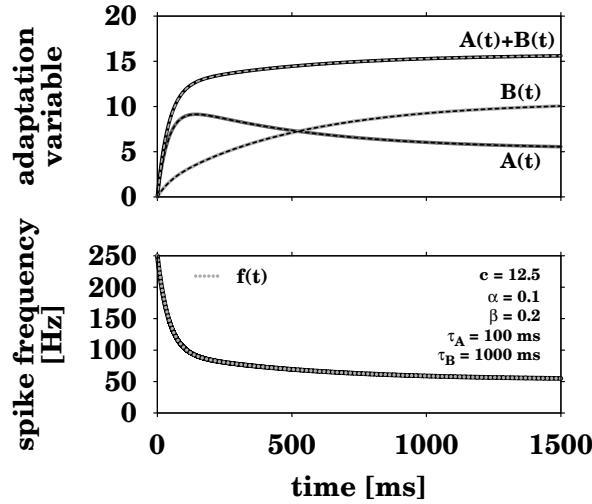


Figure 13.9: Linear firing-rate model with two adaptation currents. The adaptation variables of the fast ($A(t)$) and slow adaptation current ($B(t)$) as a function of time for an input current $I = 20$ starting at time $t = 0$ ms (top). The analytical expressions given by Eq. (13.23) are drawn as dashed lines. The sum of both ($A(t) + B(t)$) determines the adaptation of the spike frequency from its onset- to its steady-state (bottom). The analytical expression $f(t)$ for the spike frequency, given by Eq. (13.24), is drawn as gray dotted line.

that this process cannot be analyzed without considering both adaptation mechanisms (Fig. 13.10A-D). This suggests that the interspike-interval statistics can be analyzed just by considering the fast adaptation process but that it is important to take both adaptation mechanisms into account when analyzing the spike-count variability on time scales comparable or longer than $-\lambda_2^{-1}$.

From experimental measurements we are able to fit the following two-exponential function to the mean spike frequency over time measured in response to a step stimulus:

$$f(t) = C_1 e^{\lambda_1 t} + C_2 e^{\lambda_2 t} + C_3 \quad (13.25)$$

where $C_3 = f_\infty(t)$ is the steady-state spike frequency (cf. Fig. 12.1). Given a fit of $f(t)$, Eq. (13.25), to a measured spike-frequency over time of a recorded neuron, the fit parameters can be described as $C_1 = -ck_1\tilde{v}_1$, $C_2 = -ck_2\tilde{v}_2$, and $C_3 = c(I - A_\infty - B_\infty)$ with the unknowns $k_{1,2}$ and $\tilde{v}_{1,2}$ (cf. Eq. (13.24)). For $t = 0$, Eq. (13.23) can be solved for k_1 and k_2 :

$$k_1 = -\frac{(\lambda_1 \lambda_2 \tilde{v}_2 - \lambda_2^2 \tilde{v}_1 + 2\lambda_2 - 2\lambda_1)I}{\lambda_2(\tilde{v}_2 - \tilde{v}_1)(\lambda_1 \tilde{v}_2 - \lambda_2 \tilde{v}_1)} \quad (13.26)$$

$$k_2 = \frac{(\lambda_1^2 \tilde{v}_2 - \lambda_1 \lambda_2 \tilde{v}_1 + 2\lambda_2 - 2\lambda_1)I}{\lambda_1(\tilde{v}_2 - \tilde{v}_1)(\lambda_1 \tilde{v}_2 - \lambda_2 \tilde{v}_1)}. \quad (13.27)$$

Solving $C_1 = -ck_1\tilde{v}_1$ and $C_2 = -ck_2\tilde{v}_2$ for \tilde{v}_1 and \tilde{v}_2 using the solutions for k_1 and k_2 ,

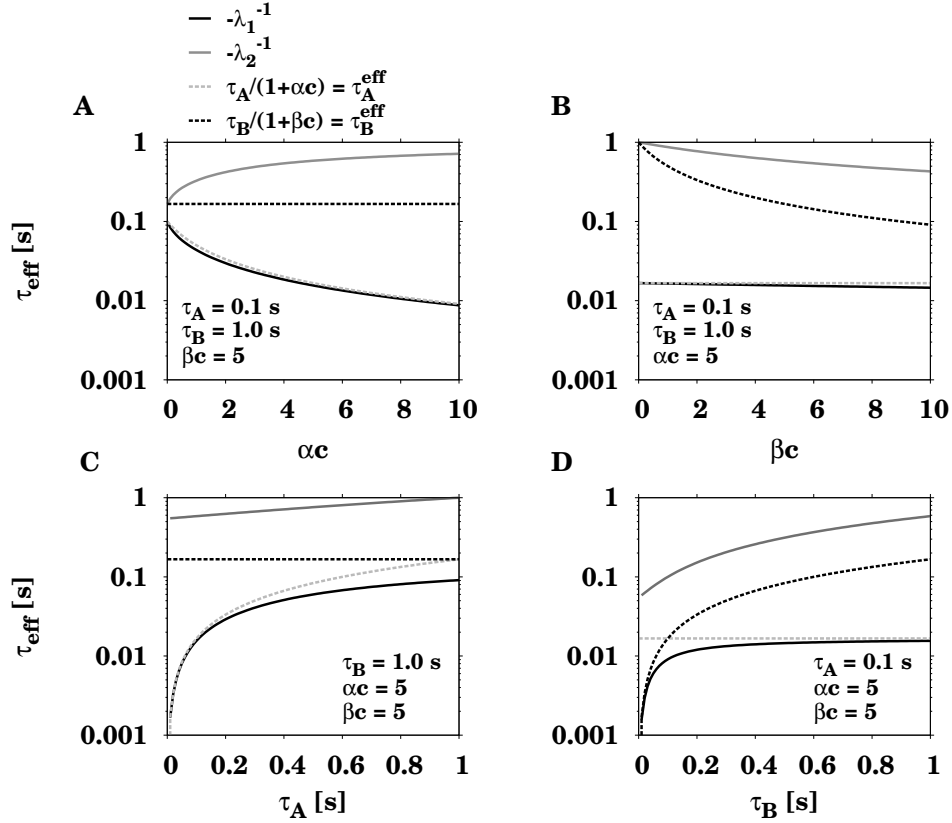


Figure 13.10: Comparison of the effective time constants of the firing-rate model with one and two adaptation currents. The effective time constant of the firing-rate model with a single adaptation current, Eqs. (13.13)-(13.14), is given by $\tau_{eff} = \tau/(1+s)$ where s is the product of the adaptation strength (α or β) and the onset gain c and where τ is the original adaptation time constant. The ones of the firing-rate model with two adaptation currents, Eqs. (13.15)-(13.17), are given by $-\lambda_1^{-1}$ and $-\lambda_2^{-1}$ (Eq. (13.21)). We compared the effective time constants of the model with two adaptation currents to the model with one adaptation current but the same parameters of the fast and slow adaptation current (A and B) for different (A) αc , (B) βc , (C) τ_A and (D) τ_B . The comparison shows that $-\lambda_1^{-1}$ and $\tau_A/(1+\alpha c)$ are comparable if $\tau_B \gg \tau_A$.

Eq. (13.26)-(13.27), results in:

$$\tilde{v}_1 = \frac{I(\lambda_2 - \lambda_1) - \frac{C_2}{c}\lambda_2 - \frac{C_1}{c}\lambda_1 + z}{\lambda_1\lambda_2 I - \frac{C_2}{c}\lambda_1\lambda_2 - \frac{C_1}{c}\lambda_1\lambda_2} \quad (13.28)$$

$$\tilde{v}_2 = \frac{I(\lambda_1 - \lambda_2) - \frac{C_2}{c}\lambda_2 - \frac{C_1}{c}\lambda_1 + z}{\lambda_1\lambda_2 I - \frac{C_2}{c}\lambda_1\lambda_2 - \frac{C_1}{c}\lambda_1\lambda_2} \quad (13.29)$$

where $z = \sqrt{I^2(\lambda_2 - \lambda_1)^2 - \frac{2I}{c}(\lambda_2 - \lambda_1)(\lambda_2 C_2 - \lambda_1 C_1) + \frac{1}{c^2}(\lambda_2 C_2 + \lambda_1 C_1)^2}$.

Using the fit parameters C_1 , C_2 , λ_1 and λ_2 of a fit of Eq. (13.25) to the experimental mean spike frequency over time for a given input current I , \tilde{v}_1 and \tilde{v}_2 can be calculated

by Eqs. (13.28) - (13.29). The parameters λ_1 , λ_2 , \tilde{v}_1 and \tilde{v}_2 can then be used to estimate the adaptation properties. These are achieved by solving the 4-dimensional equation system consisting of both the eigenvalues λ_1 and λ_2 (Eq. (13.21)) and the eigenvectors \tilde{v}_1 and \tilde{v}_2 (Eq. (13.22)) for the adaptation strengths α and β and the adaptation time constants τ_A and τ_B :

$$\alpha = -\frac{(\tilde{v}_2 - \tilde{v}_1)(\lambda_1^2 \tilde{v}_2 - \lambda_1 \lambda_2 \tilde{v}_1 + 2\lambda_2 - 2\lambda_1)(\lambda_1 \lambda_2 \tilde{v}_2 - \lambda_2^2 \tilde{v}_1 + 2\lambda_2 - 2\lambda_1)}{2c(\lambda_2 - \lambda_1)(\lambda_1^2 \tilde{v}_2^2 - 2\lambda_1 \lambda_2 \tilde{v}_1 \tilde{v}_2 + 2\lambda_2 \tilde{v}_2 - 2\lambda_1 \tilde{v}_2 + \lambda_2^2 \tilde{v}_1^2 - 2\lambda_2 \tilde{v}_1 + 2\lambda_1 \tilde{v}_1)} \quad (13.30)$$

$$\beta = -\frac{(\lambda_2 - \lambda_1)^2 \tilde{v}_1 \tilde{v}_2}{c(\lambda_1^2 \tilde{v}_2^2 - 2\lambda_1 \lambda_2 \tilde{v}_1 \tilde{v}_2 + 2\lambda_2 \tilde{v}_2 - 2\lambda_1 \tilde{v}_2 + \lambda_2^2 \tilde{v}_1^2 - 2\lambda_2 \tilde{v}_1 + 2\lambda_1 \tilde{v}_1)} \quad (13.31)$$

$$\tau_A = \frac{\lambda_1 \tilde{v}_2 - \lambda_2 \tilde{v}_1}{2(\lambda_2 - \lambda_1)} \quad (13.32)$$

$$\tau_B = \frac{\tilde{v}_1 - \tilde{v}_2}{\lambda_1 \tilde{v}_2 - \lambda_2 \tilde{v}_1}. \quad (13.33)$$

These adaptation properties can be calculated just based on a fit of the two-exponential function, Eq. (13.25), to the measured spike-frequency of a neuron (see Fig. 13.11A,B and Table 13.1)

13.2.2 Non-linear adaptation model

F-I curves of real neurons are non-linear and very often described by a square-root function (Ermentrout, 1998). A simple non-linear firing rate model with two adaptation currents is hence given by:

$$f = \tilde{c}\sqrt{I - A - B} \quad (13.34)$$

$$\tau_A \dot{A} = \alpha f - A \quad (13.35)$$

$$\tau_B \dot{B} = \beta f - B. \quad (13.36)$$

where I is an input current, A and B two deterministic adaptation currents and \tilde{c} a constant.

For the linear firing-rate model we have shown that the adaptation properties, i.e. adaptation strengths and time constants, can be calculated by Eqs. (13.30) - (13.33) using the eigenvectors and eigenvalues determined from a fit of a two-exponential function, Eq. (13.25), to the experimentally measured mean spike frequency. The gain constant c of the linear model is given by the slope of the onset f-I curve. For the non-linear firing-rate model, we estimated c by linearizing the onset f-I curve $f_0(I)$, Eq. (13.34), for which $A = 0$ and $B = 0$.

We used three different methods to determine c and tested them by means of the linear (Eq. (13.15)-(13.17)) and non-linear firing-rate model (see Eq. (13.34)-(13.36)) and, additionally, based on a more realistic single-compartment conductance-based Traub-Miles model with spike-frequency adaptation (see section 9.2, Eq. (9.11) with $D_A = 0$ and

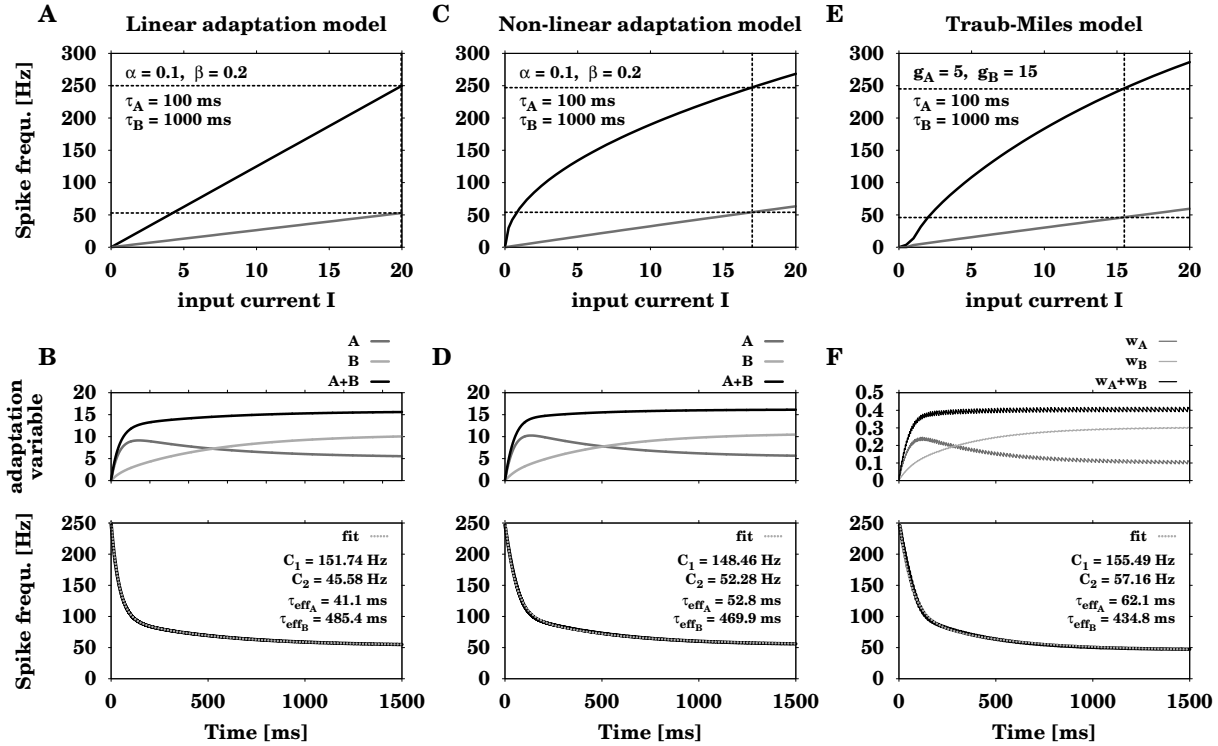


Figure 13.11: Generalized firing-rate models with two adaptation currents in comparison to a Traub-Miles model. **A,C,E** Onset- (black lines) and steady-state f-I curves (gray lines) for the linear (Eqs. (13.15)-(13.17)) and non-linear adaptation model (Eqs. (13.34)-(13.36)) as well as for the Traub-Miles model (Eq. (9.11)) with a fast ($\tau_A = 0.1\text{s}$) and slow adaptation current ($\tau_B = 1\text{s}$). **B,D,F** (top) The adaptation variables of the fast and slow adaptation current over time (light and dark gray lines) for a defined input current I as marked in A,C,E as dashed line. The adaptation variables are voltage-dependent and the sum of both (black line) determines the adaptation of the spike frequency from its onset- to its steady-state. (bottom) The mean spike frequency of the current over time (black line) with a fit of Eq. (13.25) (gray dashed lines).

$D_B = 0$). Simulations of these three models show that the adaptation variables follow a similar time course independent of the individual model dynamics and shape of f-I curve (see Fig. 13.11A,C,E and B,D,F top). The sum of the adaptation variables defines the decay of the spike frequency which can be fitted using a two-exponential function, Eq. (13.25), in all three models (see Fig. 13.11B,D,F bottom). For the different models, the estimated adaptation properties, i.e. the strengths and time constants of the two adaptation currents, are illustrated in Table 13.1 for respectively one exemplary input current I (same ones as used in Fig. 13.11B,D,F).

In Benda and Herz (2003), the constant c of the linear model was calculated by expanding the f-I curve around $f_\infty(I)$:

$$c = f'_0(f_0^{-1}(f_\infty(I))) \quad (13.37)$$

where f_0^{-1} is the inverse function of the onset f-I curve f_0 . This method, however, is only

Model	$c = f'_0(f_0^{-1}(f_\infty(I)))$	α	β	$\tau_A[ms]$	$\tau_B[ms]$
Linear	12.5	0.099	0.20	98.23	994.07
Non-linear	35.14	0.009	0.005	69.93	534.76
Traub-Miles	24.8	0.023	0.026	101.32	596.50
	$c = (f_0 - f_\infty)/(I - f_0^{-1}(f_\infty(I)))$	α	β	$\tau_A[ms]$	$\tau_B[ms]$
Linear	12.52	0.099	0.198	98.03	990.05
Non-linear	12.4	0.101	1.496	144.41	3577.52
Traub-Miles	15.77	0.062	0.363	144.44	1440.77
	$c = f_0(I)/I$	α	β	$\tau_A[ms]$	$\tau_B[ms]$
Linear	12.5	0.099	0.20	98.23	994.07
Non-linear	14.55	0.073	0.223	120.12	1097.39
Traub-Miles	15.86	0.062	0.343	143.60	1393.86

Table 13.1: Calculation of the adaptation strengths α and β as well as the time constants τ_A and τ_B of the two adaptation currents from the mean spike frequency over time. Using Eqs. (13.30)-(13.33) we are able to calculate the original adaptation properties, which were $\alpha = 0.1$, $\beta = 0.2$, $\tau_A = 100ms$ and $\tau_B = 1000ms$, from the fit of Eq. (13.25) to the mean spike frequency over time (data here are exemplary for the samples shown in Fig. 13.11B,D,F). We used different linearization procedures to determine the gain parameter c which is constant for every input current I of the linear adaptation model (Eqs. (13.15)-(13.17)) but changes for every I of non-linear models. For models whose f-I curves are roughly the square root of the input current I the gain parameter $c = f_0(I)/I$ provided the best approximation for the calculation of the adaptation properties α , β , τ_A and τ_B .

correct for small deviations of f_∞ from f_0 . In the case of a two-fold adapting model the spike frequencies of the onset- and steady-state deviate a lot. Thus, the calculation of the adaptation properties results in an underestimation of the adaptation strengths and time constants for both non-linear models.

Following Benda and Herz (2003), the steady-state of the non-linear firing rate model is given by

$$A_\infty + B_\infty = f_\infty^{-1}(f_\infty(I)) - f_0^{-1}(f_\infty(I)) = I - f_0^{-1}(f_\infty(I)). \quad (13.38)$$

For the linear firing-rate model we have shown that $A_\infty = \alpha c I / (\alpha c + \beta c + 1)$ and $B_\infty = \beta c I / (\alpha c + \beta c + 1)$. Solving $A_\infty + B_\infty$ for c results in $c = (A_\infty + B_\infty) / ((\alpha + \beta)(I - A_\infty - B_\infty))$. Substituting α and β by Eq. (13.30)-(13.31) and Eq. (13.28)-(13.29) gives us then $c = (C1 + C2) / (A_\infty + B_\infty)$. Since $C1$ and $C2$ describe the frequency decay from f_0 to f_∞ (see Eq. (13.25)), c can be determined by

$$c = (f_0 - f_\infty) / (I - f_0^{-1}(f_\infty(I))). \quad (13.39)$$

Similarly as for the estimation of c given by Eq. (13.37), this solution is just correct for small deviations of f_∞ from f_0 . The calculation of the adaptation properties results

here in large deviations of the adaptation time constants in particular for the non-linear firing-rate model.

A third way of linearization is given by squaring $f_0(I)$ and solving for c . This gives us the slope of the tangent line at I :

$$c = f_0(I)/I. \quad (13.40)$$

For models featuring an onset f-I curve which is in approximation described by a square-root function (or a linear function), this solution for c yielded the best estimates of the adaptation properties.

The nonlinear dynamics of a neuron's spike-generating mechanism make it hard to achieve the correct adaptation properties just based on the spike-frequency of a recorded neuron. However, the method described here allows to get an approximation of the properties of spike-frequency adaptation mediated by two adaptation currents. The firing-rate models, furthermore, support an important role of the interaction of two adaptation currents on long time scales. However, for the case that the adaptation processes are working on separate time scales, the models, additionally, suggest that the interaction can be ignored for short time scales in the range of the fast adaptation time constant.

Simulations of the locust auditory transduction cascade suggested that the spike-count variability observed in spike responses of locust auditory receptor neurons can be explained by two adaptation currents. In this chapter, we analyzed how two adaptation currents shape the spike-count variability. By means of theoretical investigations, we demonstrated that two adaptation currents shape the Fano factor by mutual interaction and that the fast adaptation process reduces the noise of the slow process at low-frequencies.

Part IV. DISCUSSION

The contribution of different noise sources to the spike-response variability in locust auditory receptor neurons

Spike-response variability in locust auditory receptor neurons

Spike-response variability is a common feature of sensory neurons that impacts neural information processing. However, little is known about the nature of the noise sources causing variability. In this thesis, we investigated potential sources of spike-response variability in auditory receptor neurons of *Locusta migratoria*. In particular, we focused on the stochastic opening of the mechanosensory receptor channels and other ion channels whose activation is strongly correlated to sound intensity, like the ones carrying the adaptation current and channels that play a significant role in the generation of action potentials.

By means of interspike-interval statistics, we were able to distinguish different kinds of channel noise sources. Simulations of a minimal conductance-based model suggested that fast stochastic ionic currents and slow stochastic adaptation currents contribute differentially to the spike-response variability in locust auditory receptor cells. Moreover, they suggested channel noise from an adaptation current and from the receptor or sodium current as the main sources for the spike-response variability.

Furthermore, we analyzed both the dynamics and the spike-count variability of models with two adaptation currents. The findings suggested that two adaptation currents shape the spike-count variability by mutual interaction and that at least two adaptation processes are responsible for the long-range variability in locust auditory receptor neurons.

Chapter 15

Different noise sources and how they contribute to the ISI variability

The aim of chapter 10 and 11 of this thesis was to infer properties of the dominating intrinsic neuronal noise source solely from the statistics of interspike intervals. Our data obtained from *in vivo* axonal recordings of locust auditory receptor neurons show a transition from a white-noise dominated regime at low spike frequencies to a colored-noise dominated regime at high spike frequencies. In particular, the ISIs in the lower dynamic range of the receptor response have a high variability with CVs up to 0.9 as well as a pronounced peak of D_{rnwl} . With increasing spike frequency the shape of the ISI histograms changed from an inverse Gaussian, that typically results from white noise sources (Gerstein and Mandelbrot, 1964), to more peaked probability densities with heavier tails, indicating a colored-noise source (Lindner, 2004). In accordance with the ISI distributions, the corresponding ISI correlations showed a transition from slightly negative values to positive coefficients with increasing spike frequency.

In response to pure tones with constant sound intensities the auditory receptor neurons of locusts respond with firing rates of up to a few hundred Hertz (Römer, 1976). This and the non-exponential shape of the ISI distributions (Schaette et al., 2005) strongly indicate that these neurons operate in the super-threshold regime. In this regime the neurons would regularly oscillate, i.e. they would generate periodic spike trains, if they were noiseless and driven by a constant input. The canonical model for such a limit-cycle dynamics is the perfect integrate-and-fire (PIF) model. The simplest way to introduce spike-timing variability in this model is to add a white-noise driving. The evolution of the state variable of the PIF model is then equivalent to a random walk with drift towards an absorbing barrier for which the inverse Gaussian is known to describe the first-passage-time distribution, which in our case yields the ISI distribution (Gerstein and Mandelbrot, 1964).

The locust receptor neurons also show pronounced spike-frequency adaptation (Römer, 1976; Benda et al., 2001). Despite the presence of an additional slow dynamics causing spike-frequency adaptation the ISI density of a PIF neuron model with additive

white noise can still be well approximated by an inverse Gaussian (Schwalger et al., 2010). However, the interaction of the white noise with the adaptation dynamics results in negative ISI correlations (Wang et al., 1998; Chacron et al., 2000; Liu and Wang, 2001; Benda et al., 2010; Schwalger et al., 2010) – a feature that is absent in a white-noise driven PIF model without adaptation. Negative ISI correlations have been reported for various preparations (see Farkhooi et al., 2009 for a review), and have been suggested to play a role in reducing long-term variability (Ratnam and Nelson, 2000; Chacron et al., 2001, 2007).

At low spike frequencies our recorded ISI distributions are well described by inverse Gaussians and we also found small but significant negative correlations in this regime. Both findings suggest that at low spike frequencies the dominating noise source of locust auditory receptors generates white noise that interacts with a deterministic adaptation dynamics.

By means of simulations of Hodgkin-Huxley-type models we tested different hypotheses on possible white-noise sources that could account for the experimentally observed results. Channel noise originating from the delayed rectifier failed to reproduce either the peak in $D_{r_{nwl}}$ or the ISI distributions and correlations. However, both stochastic receptor currents as well as stochastic sodium currents reproduced this peak as well as the white-noise ISI distributions and the negative ISI correlations in interaction with a deterministic adaptation current. These findings suggested that stochastic sodium or receptor currents may strongly shape the lower dynamic range of locust auditory receptor neurons.

Colored noise like Ornstein-Uhlenbeck noise with sufficiently long correlation times results in different ISI statistics. The ISI distributions are more peaked and have longer tails compared to the inverse Gaussian, and the correlations of the noise directly translate to positive correlations between successive ISIs (Lindner, 2004; Schwalger et al., 2010). Positive correlations have been observed in other neural systems (Lowen and Teich, 1992; Gabbiani and Krapp, 2006) but the origin of the corresponding colored noise was unknown or hypothesized to be of synaptic origin (Chacron et al., 2001; Middleton et al., 2003).

Let us note that estimates of ISI correlations calculated from too few ISIs are strongly biased towards negative numbers (Flyvbjerg and Petersen, 1989). This can easily happen when calculating the correlations from responses to short stimuli for each trial separately. For this reason it might be that Schaette et al. (2005) did not observe any positive ISI correlations in their recordings from the locust auditory receptor neuron.

Our simulations of the locust auditory transduction cascade with single stochastically gated channels demonstrated that stochastic adaptation currents can account for peaked ISI histograms which can be described by the colored-noise probability density. Furthermore, stochastic adaptation produced positive ISI correlations and reproduced the peak in $D_{r_{nwl}}$. These results suggested that stochastic adaptation may strongly contribute to the spike-response variability in the upper dynamic range.

How does a noisy adaptation current shape the ISI histograms and the correlations between ISIs? We analyzed this question for the limit case of pure stochastic adaptation

and for the case of a deterministic adaptation current and an additional white noise current.

For a PIF model, it was shown that stochasticity in the adaptation leads to pronounced peaks and a heavy tail compared to the case of deterministic adaptation, for which the ISI density is close to an inverse Gaussian (Schwalger et al., 2010). Furthermore, the limit cases showed a pronounced difference in the ISI correlations. For a deterministic adaptation current and a white noise driving one observes negative correlations between ISIs as reported previously (e.g. Liu and Wang, 2001). In contrast, with slow adaptation noise ISIs exhibit long-range positive correlations. The underlying mechanism leading to the large kurtosis and the positive ISI correlations in the case of stochastic adaptation rests upon the fact that slow adaptation noise effectively acts as an independent colored noise with a large correlation time (Schwalger et al., 2010). One can think of the colored noise as a slow external process that slowly modulates the instantaneous firing rate or, equivalently, slowly changes the ISIs in the sequence. Such a sequence of many short ISIs in a row and a few long ISIs gives rise to a large skewness and kurtosis and positive serial correlations.

Our simulations of a more realistic Hodgkin-Huxley-type model with stochastic adaptation or deterministic adaptation plus white noise predicted all the features observed in the perfect integrate-and-fire model augmented with an adaptation mechanism. This indicates the generality and robustness of our findings.

The peaked shape of the ISI distributions as well as the positive ISI correlations we observed at higher spike frequencies in the receptor neurons of locusts can thus be explained by a colored-noise source. The additional match of the correlation time-constant of the noise obtained from the ISI distributions with the time constant of the apparent spike-frequency adaptation further suggests that the stochasticity of an adaptation current is the source of the colored noise (Schwalger et al., 2010).

Our simulations confirm that a stochastic adaptation current together with fast channel noise indeed reproduces both the white-noise ISI distributions and negative ISI correlations at low spike frequencies and the colored-noise ISI distributions and positive correlations at higher spike frequencies. The impact of the colored noise in relation to the white noise increases with spike frequency for two reasons. First, the ratio between adaptation time scale and mean ISI becomes larger with increasing firing rate. The strength of positive ISI correlations and the deviations of the ISI density from an IG grow if this ratio increases. Second, the mean fraction of open adaptation channels increases with spike frequency from values close to zero to less than 10 %, as measured in the simulations of the modified Traub-Miles model (Ermentrout, 1998). Because the standard deviation of the fraction of open channels is zero when all channels are closed and monotonically rises until half of the channels are open (a state that is never reached here), the fluctuations of the adaptation current increase with spike frequency and so does the strength of the resulting colored noise. In marked contrast, the level of fluctuations for the fast noise sources saturates at large signal amplitude or high firing rates (simulation data not shown). We note that a stochastic adaptation current could also explain very similar data on CV and ISI correlations found in response to current pulse

injections in a looming-sensitive neuron (Gabbiani and Krapp, 2006), in particular, the observed transition from negative ISI correlations at low rate and high CV to positive ISI correlations at high firing rate and low CV.

Gollisch and Herz (2004) have shown that spike-frequency adaptation of locust receptor neurons has both an input- and an output-driven component. The input-driven component could be due to fatigue of the tympanum or the transducer channels and directly depend on the acoustic input. In contrast, the output-driven component could be attributed to adaptation currents that are activated by the resulting action potentials. However, they were not able to quantify the relative strength of the two adaptation components. Because in these neurons the adaptation time constant depends on spike frequency and thus on the spike response (Benda et al., 2001; Benda and Herz, 2003), output-driven adaptation currents seem to be the dominant adaptation mechanism. This further supports our finding of a colored-noise source possibly originating from an adaptation current.

There is a vast variety of output-driven ionic currents causing spike-frequency adaptation. The most prominent ones are voltage-gated M-type currents (Brown and Adams, 1980) and calcium-activated potassium currents (Madison and Nicoll, 1984; Sah and Davies, 2000). Also, slow inactivation of the voltage-gated sodium current is a possible source of output-driven spike-frequency adaptation (Fleidervish et al., 1996; Torkkeli et al., 2001). In cockroach tactile spine neurons the rapid adaptation component is caused by slow inactivation of the sodium current (French, 1987), whereas the slow adaptation current can be attributed to the activation of an electrogenic sodium pump (French, 1989). Which of these adaptation mechanisms is causing spike-frequency adaptation and the colored noise in the locust auditory receptor neuron is not known and cannot be deduced by our indirect methods from the ISI statistics. For the simulations we used M-type currents as a prototype for any adaptation mechanism. In the super-threshold regime, both the deterministic component of the adaptation dynamics and the effects of the stochasticity are similar for the different adaptation mechanisms on the level of spike timing (Benda and Herz, 2003; Schwalger et al., 2010). This suggests that the main results derived here are not specific to a certain adaptation current, but apply quite generally to any noise associated to the slow dynamics of adaptation.

What, however, is a possible source of the white noise? Thermal noise due to the membrane resistance has only a minor importance in neurons compared to other noise origins (Lecar and Nossal, 1971; Manwani and Koch, 1999; van Rossum et al., 2003). In the auditory system, thermal noise may also result from pressure fluctuations caused by collisions of air molecules with the eardrum. However, when simulating eardrum oscillations with additive Gaussian noise, the strength of the noise needed to reproduce the experimentally observed interspike-interval variability was so high that the neuron was not able to code for sound intensity any more (data not shown).

Synaptic noise is considered as one of the major noise sources in the nervous system. Locust auditory receptors, however, are bipolar neurons that are directly attached to the eardrum (Gray, 1960) and generate action potentials without intermediate synapses and, hence, in absence of synaptic noise.

The most likely candidate for the white noise therefore is channel noise resulting from random opening and closing of ion channels (White et al., 2000). From experimental studies using non-stationary noise analysis sodium (Sigworth, 1980), receptor (Holton and Hudspeth, 1986), and adaptation currents (Villarroel, 1997) are known for contributing to current fluctuations. Modeling studies addressed the distinct effects of channel noise from different ionic currents on spike-timing variability (Chow and White, 1996; Schneidman et al., 1998; van Rossum et al., 2003). Dorval and White (2005) demonstrated experimentally that channel noise from sodium currents drive sub-threshold oscillations.

The simulations demonstrated that noise from different types of finite ion channel populations can have a profound influence on neuronal action potential generation. However, the simulations do not allow to accurately estimate the actual number of ion channels of the receptor, sodium or adaptation current, since there are too many degrees of freedom. In particular, the number of ion channels of a population and the single-channel conductivity to some degree counteract each other so that different combinations of these two parameter result in similar ISI statistics. Still, the number of receptor channels we used in the mixed-case model ($N_R = 20$, Fig. 11.9) matches the reported order of magnitude of channel numbers of other mechanosensory transducer currents (Drosophila: $N \approx 20$ per sensory neuron, Nadrowski et al., 2008; bullfrog: $N = 85 \pm 45$ per hair bundle, Howard and Hudspeth, 1988).

Note that especially at higher firing rates the ISI variability is quite small in locust auditory receptor cells, quantified both by relative ($CV \approx 0.1$) and absolute measures ($\sqrt{\langle \Delta T^2 \rangle} < 1$ ms). Such high spike-timing precision in these neurons was also observed during natural (Ronacher et al., 2004, 2008) and dynamic stimulation and underlies their coding efficiency (Machens et al., 2001; Rokem et al., 2006). Thus, the positive correlations we observed in this regime affect the ISIs by less than a millisecond. Also, the small negative correlations at low spike frequencies might be negligible in the context of encoding the amplitude modulation of an acoustic stimulus. This explains the good performance of a renewal model in reproducing mean firing rate and spike-count statistics in response to dynamic stimuli (Schaeffer et al., 2005) by utilizing the regularizing effect of neural refractoriness (Berry and Meister, 1998).

At low spike frequencies, however, the variability becomes quite large with CVs ranging from about 0.5 up to 0.9. Here, two opposing hypothesis on why the spike timing variability is so high in this regime are possible. First, although this variability might deteriorate coding fidelity of a single receptor, this regime might not play an important role for the whole population of receptor neurons to encode sound stimuli and thus this noise could be tolerated. Second, because averaging over trials in these neuron improves stimulus representation (Machens et al., 2001), noise might be advantageous. This would suggest that the number of receptor or sodium channels is on purpose small, in order to result in the necessary amount of noise for improving the representation of the sound stimuli in the population of receptor neurons.

Direct measurements of the current noise close to the site of receptor current and spike generation, for example by non-stationary noise analysis under voltage-clamp,

potentially damage the delicate sensory structures and thus bias the obtained results. This is in particular a problem in auditory systems of both insects and vertebrates. Therefore, indirect methods that infer properties of the transduction cascade and the spike generator from recordings of the auditory nerve, that leave the ear intact, allow to investigate functional aspects of sensory transduction and set detailed references for future invasive measurements. Using the iso-response method, Gollisch et al. (2002); Gollisch and Herz (2005) have been able to characterize the auditory transduction cascade of locust auditory receptor neurons and to differentiate between input- and output-driven adaptation processes in these neurons (Gollisch and Herz, 2004).

We here recorded interspike-interval statistics generated from the intact locust ear from the auditory nerve far away from the ear. By comparing higher-order statistics of the data with the properties known from canonical models for spiking neurons in their super-threshold regime we were able to demonstrate that white- and colored-noise sources dominate the interspike-interval statistics in different firing regimes. Additional simulations of conductance-based models as well as the analytical study by Schwalger et al. (2010) strongly suggest a stochastic adaptation current as the source for the colored noise and the receptor or sodium current as the possible sources for the white noise. Because the theories we used for interpreting our results are so general, our approach for dissecting intrinsic sources of neural noise can be applied to many other neurons as well.

Chapter 16

Effect of multiple time scales of adaptation on the spike-count variability

The aim of chapter 12 was to analyze the contribution of neuronal noise sources to the spike-count variability observed in spike responses of auditory receptor neurons of *Locusta migratoria*. We quantified the spike-count variability by the Fano factor that was calculated for different counting time frame lengths. Spike responses of one minute duration that were used to measure the Fano factor for counting time frames up to $t_c = 10$ s, demonstrated for the first time that the spike responses of locust auditory receptor neurons adapt at least over two time scales in the range of 0.1 s and several seconds.

The Fano factor curves of the auditory spike responses exhibit a minimum at moderate counting times and monotonically increase as power-law functions with exponent κ to values up to $F(t_c) \approx 10$ at large counting times depending on sound intensity. No saturation of $F(t_c)$ is visible for counting time frames up to 10 s. With increasing sound intensity the position of the Fano factor minimum, t_c^{min} , shifts to smaller counting times and the exponent increases from $\kappa \approx 0.5$ to exponents close to one. The increase of the Fano factor curve for moderate and large counting times is caused by positive ISI correlations (Cox and Lewis, 1966).

Positive ISI correlations arise from colored noise (Lindner, 2004; Schwalger et al., 2010). For a PIF model driven by an exponentially correlated (colored) Ornstein-Uhlenbeck (OU) noise with large correlation time constant, the Fano factor has been extensively analyzed and analytical expressions have been derived (Middleton et al., 2003). OU noise increases the Fano factor with exponent $\kappa = 1$ for moderate counting times $t_c < \tau^{OU}$ depending on the noise intensity. The counting time at which the Fano factor curve saturates is close to the finite correlation time of the colored noise. The noise intensity determines at which Fano factor level the curve saturates.

The shift of the Fano factor curves of the locust auditory receptor neurons, i.e. the decrease of t_c^{min} and increase of κ , with increasing sound intensities cannot be explained by the PIF model driven by a single colored noise source because (i) an OU process with

a fast correlation time constant does not yield large $F(t_c)$ at large counting times, and (ii) an OU process with a slow correlation time constant, that could explain the Fano factor at large t_c , does not yield exponents $\kappa < 1$.

In a similar way, the locust auditory transduction model with a single stochastic adaptation current, effectively acting as colored noise, cannot explain the measured Fano factor curves. Simulations of the locust auditory transduction cascade with both the fast and the slow stochastic adaptation current can indeed reproduce the ISI statistics and both the decrease of t_c^{min} and increase of κ with increasing sound intensities.

Spike responses of the locust auditory receptor neurons show that the slow adaptation process is only activated for firing rates $f > 40$ Hz. We therefore modeled the slow adaptation current as a Ca^{2+} -activated (AHP) potassium current. We assumed that the AHP current is only activated by calcium concentrations exceeding a certain threshold.

Ca^{2+} -activated potassium currents mediating spike-frequency adaptation are known to have a slow time course in the range of seconds (Sah, 1996; Faber and Sah, 2003). So far, however, it is not known which currents are responsible for spike-frequency adaptation in the auditory receptors of *Locusta migratoria*. Future experiments, in which the ionic currents responsible for spike-frequency adaptation are pharmacologically blocked, could verify our hypothesis that the slow adaptation in locust auditory receptor neurons is mediated by Ca^{2+} -activated potassium currents.

In chapter 13, we analyzed a PIF model with one and two independent colored noise sources. Middleton et al. (2003) showed for the PIF model with a single OU noise source with a large correlation time constant τ^{OU} that the exponent κ , which defines the Fano factor rise at moderate counting times $t_c^{min} < t_c < \tau^{OU}$, equals one. This, however, is only true for $t_c \ll \tau^{OU}$. A PIF model driven by a colored noise with $\tau^{OU} = 0.1$ s, that is equal to the fast adaptation time constant of locust auditory receptor neurons, yields Fano factor curves with an apparent exponent κ much smaller than one. The reason is that we do not see the linear part but only the shallower ($\kappa < 1$) curve close to saturation. This would explain why the Fano factor curves of locust auditory receptor neurons show exponents $\kappa \approx 0.5$ for low sound intensities where the fast adaptation process with a time constant $\tau = 0.1$ s alone mediates spike-frequency adaptation and where t_c^{min} takes values even larger than τ . Large t_c^{min} result from a low noise level. An increase of the noise level with increasing sound intensities, that results in decreased t_c^{min} , might be caused by a second noise process starting at higher sound intensities that additionally affects the spike-response variability.

For the Fano factor curves of a PIF model with two independent colored noise sources, the same holds true. If the correlation time constant τ_A^{OU} of the fast colored noise source is close to t_c^{min} and the intensity of the slower colored noise source is not too large, we again do not see the linear part of $F(t_c)$ but only the shallower part close to saturation with $\kappa < 1$. This suggests that the decrease of t_c^{min} and increase of κ observed for the Fano factor curves of locust auditory receptor neurons with increasing sound intensity is caused by a transition of a major contribution of the fast adaptation process for low sound intensities to a major contribution of the slower adaptation process for larger

sound intensities.

Adaptation currents are driven by action potentials (Benda and Herz, 2003). In contrast to independent colored noise sources, they are therefore correlated to each other. The dynamics of a PIF model and a more realistic Hodgkin-Huxley-type model with two adaptation processes show a mutual interaction of two currents mediating spike-frequency adaptation. Analytical expressions, that we have derived for a firing-rate model with two adaptation processes, confirm this mutual interaction. The two interacting currents show an antagonistic behavior which can regularize the spike-response variability. A rapid deterministic current counteracts a slow stochastic adaptation current and, thus, decreases both ISI and spike-count variability. Fast adaptation regularizes the variability arising from a slower noise source by reducing noise power at low frequencies. In contrast to the noise shaping of a fast deterministic adaptation current in interaction with white noise described by Chacron et al. (2004), this is a reduction of the total noise level.

Let us note that the effective time constant τ_A^{eff} of the fast adaptation process is not altered by the presence of an additional slow adaptation process provided $\tau_B \gg \tau_A$. For the locust auditory system, the slow adaptation process with a time constant τ_B of several seconds is much slower than the rapid one with a time constant τ_A of a hundred milliseconds. This independence of the existence of a second slower adaptation process demonstrates and justifies the analysis of the ISI statistics on short time scales without considering an interaction of a slower adaptation process as we have done in chapter 10.

Fano factor curves exhibiting a minimum were observed in cat auditory nerve fibers (Teich, 1989), in the cat visual system (Teich et al., 1997), and in electroreceptors of weakly electric fish (Chacron et al., 2001). Fano factor curves of cat auditory hair cells show Fano factor curves similar to the ones of locust auditory receptor cells where the exponent of the curve for moderate counting times is given by $\sqrt{t_c}$ (exponent: $\kappa = 0.5$, Teich, 1989). Additionally, the Fano factor rises to large values $F(t_c) \approx 10$ without a visible saturation up to the measured counting time of 20 s. This suggests a potential interaction of a rapid and a slow colored noise source in the cat auditory system. Teich (1989) attributed the increase of the Fano factor curve to the fractal nature of the auditory neuronal spike responses. Similar Fano factor curves were also found in cat retinal ganglion cells (RGC) and lateral-geniculate-nucleus cells (LGN) which both exhibit exponents $\kappa < 1$ (RGC: mean $\kappa = 0.76 \pm 0.22$ s.d.; LGN: mean $\kappa = 0.64 \pm 0.23$ s.d.) and $F(t_c) > 10$ for $t_c = 1000$ s without visible saturation (Teich et al., 1997). The spike-count and interspike-interval variability of RGC and LGN could be explained by a fractal binomial-noise-driven doubly stochastic gamma point process where the fractal binomial noise is generated from the sum of K alternating fractal renewal processes. Fractal binomial noise is used to describe the fractal behavior of stochastic ion channel opening (Lowen and Teich, 1995). Our results suggest that these data could also be explained by stochastic ionic currents effectively acting as colored noise, such as multiple stochastic adaptation currents.

For weakly electric fish, the counting time frame defining the Fano factor minimum corresponded to the time scale which is used to detect prey (Nelson and Maciver, 1999). In general, a single stochastic adaptation current, effectively acting as colored noise,

is sufficient to cause such a minimum. A second colored noise source, additionally affecting the spike-response variability and increasing the noise level, shifts t_c^{min} to smaller counting times. The resulting increase of the spike-count variability of auditory receptor neurons for large counting times is most probable not relevant for locusts. For example, for the grasshopper *Chorthippus biguttulus*, which exhibits a similar spike-count variability compared to *Locusta migratoria* (Ronacher and Krahe, 2000), the first 250 ms of a calling song is sufficient for a reliable recognition of a song (Ronacher and Krahe, 1998; Ronacher et al., 2008). The minimal counting time t_c^{min} of the Fano factor curves of locust auditory receptor neurons decreases from 250 ms to 25 ms with increasing sound intensity. This could be explained by a reduction of the signal duration that is necessary for a reliable recognition of calling songs with higher sound intensity.

Functional role of channel noise

In this thesis, both experimental findings and simulations of minimal conductance-based models of auditory receptor neurons of *Locusta migratoria* suggest ion channel noise from adaptation currents as well as from the receptor or sodium current as the main source of the interspike-interval and spike-count variability. But what may be the functional role of such channel noise in the auditory system?

Experimental and theoretical studies have shown that noise in general can play a beneficial functional role in a variety of biological systems (Douglass et al., 1993; Bezrukov and Vodyanoy, 1995; Collins et al., 1995; Wiesenfeld and Moss, 1995; Levin and Miller, 1996). In these studies, they particularly focused on stochastic resonance, i.e. the noise-induced enhancement of weak signals. Experiments have demonstrated that auditory hair cells exhibit stochastic resonance at physiologically relevant noise levels (Jaramillo and Wiesenfeld, 1998, 2000; Zeng et al., 2000; Indresano et al., 2003). Furthermore, a theoretical study on stochastic resonance in a system with white- and colored-noise driving demonstrated that colored noise may be better for enhancing the neuron's response to a weak signal in comparison to white noise (Nozaki et al., 1999). This is valid for the case that the noise bandwidth is sufficiently high and, thus, the noise can be used in this regime to detect subthreshold signals with a smaller noise level. A model of the mechano-electrical transduction of auditory hair cells demonstrated that two colored-noise sources (gate and bundle noise) were able to explain the experimentally measured signal-to-noise ratios of frog saccular hair cells (Lindner et al., 2005b). Like in locust auditory receptor neurons, two different adaptation mechanisms, a fast and a slow one, are known for auditory hair cells (Eatock, 2000; Gillespie, 2004). These may effectively work as two colored-noise sources. A theoretical study showed that the combination of two adaptation processes can produce oscillations at a characteristic frequency and, thus, provide an active amplifier mechanism (Vilfan and Duke, 2003). However, if subthreshold stochastic resonance or active amplification mechanisms may play a functional role in the locust auditory system is not known yet.

The transmission of suprathreshold signals was commonly believed to be impaired by noise. A recent theoretical study, however, showed that noise can have a beneficial

role also in the suprathreshold signal transduction of auditory hair cells (Xiang-Hui et al., 2008). Classical stochastic resonance was shown to extend the dynamic range of a system to subthreshold signals, whereas suprathreshold stochastic resonance enhances it at larger signal intensities (Stocks, 2000). Suprathreshold stochastic resonance reveals a facilitation of signal transmission by a population of sensory neurons which receive the same input and collectively encode the signal. Population coding was suggested to average variable responses of individual neurons to achieve reliable responses (Sakurai, 1996; Pouget et al., 2000; Averbeck and Lee, 2004; Averbeck et al., 2006). Recently, a theoretical study, in which the effect of suprathreshold resonance has been analyzed, demonstrated that the signal detection of a population of neurons could be enhanced by an optimal amount of ion channel noise (Ashida and Kubo, 2010). This indicates that channel noise may play an essential role in population coding and in the optimization of responses of a population of sensory neurons. So far, however, only theoretical studies exist about suprathreshold resonance. Locust auditory receptor cells are neurons which fire action potentials in the suprathreshold regime with high spike frequencies. Furthermore, Machens et al. (2001) showed that the rate of information about signal features in locust auditory receptor neurons is improved when neuronal responses are pooled. This suggests that rather suprathreshold than classical subthreshold stochastic resonance may play a functional role in the locust auditory system.

In single neurons, the transmission of information may be limited by the stochasticity of ion channels (Laughlin et al., 1998; White et al., 2000). To increase information it would be necessary to increase the number of channels in the membrane so that fluctuations are averaged out. An increase of the channel number, however, increases the consumption of energy used for signal transmission (Laughlin et al., 1998). On the contrary, a low number of ion channels yield low energy costs but poor information transmission. In a theoretical study, it was shown that an optimal energy efficiency is gained for a specific medium number of ion channels (Schreiber et al., 2002). This study additionally demonstrated that noisy input signals reduce the optimal number of ion channels. This suggests that a low number of channels in locust auditory receptor neurons may yield an energy efficient signal transmission in the presence of additional background noise, such as in a loud environment. The preferred habitat of locusts is in fields and meadows. At such places, background noise from the environment, such as from moving water or from sounds made by animals of identical or different species, may add noise to the communication signals allowing an energy efficient information processing with a low number of ion channels in the membrane of the auditory receptor neurons.

The effects of correlations between successive interspike intervals which arise from different noise sources on neuronal coding was recently reviewed in Avila-Akerberg and Chacron (2011). Already in a very early experimental study, the importance and effects of ISI correlations on the activity of muscles has been demonstrated. In this study, Sugano and Tsukada (1978) stimulated excitatory motor axons electrically with three different types of spike sequences with (i) negative, (ii) positive, and (iii) uncorrelated ISI correlations. Using these different statistical stimuli, they were able to show that the opening movement of crayfish opener muscles varies significantly for the three types

of correlated spike sequence stimuli. Spike sequences with negative ISI correlations resulted in less variable motor responses in comparison to sequences with the same spike frequency but uncorrelated or positive correlated ISIs (Birk, 1972; Sugano and Tsukada, 1978). Likewise, spike responses with negative ISI correlations display less variable spike-count distributions which can increase the discriminability and detectability of weak signals (Ratnam and Nelson, 2000; Chacron et al., 2001; Goense and Ratnam, 2003). The functional role of positive ISI correlations, in contrast, is less understood. Positive correlated ISI sequences electrically stimulating the motor axons of the crayfish opener muscle yielded larger movement amplitudes in contrast to negative correlated or uncorrelated spike sequences (Sugano and Tsukada, 1978). In studies concerning spike-count variability, positive ISI correlations have been shown to increase variability for large counting times. This, in turn, yields a minimum for specific time frames for which variability is smallest (Chacron et al., 2001; Longtin et al., 2003; Middleton et al., 2003). Thus, this defines an optimal time scale for the detection of signals. The combination of negative and positive correlations may therefore yield optimal noise levels for behaviorally relevant time scales.

In clinical applications, neuronal noise, such as channel noise, can have a beneficial role in cochlear implants. Cochlear implants are medical devices which can help patients who suffer from deafness caused by a loss of sensory hair cells in the cochlea (Rubinstein and Miller, 1999). Using electrical stimulation of auditory nerve fibers, cochlear implants try to evoke neuronal responses which are normally generated by acoustic stimulation. Inner hair cells, however, are known to release neurotransmitters in a stochastic manner and with a high degree of spontaneous release. Electric stimulation, in contrast, lacks spontaneous activity and evokes deterministic responses (Kiang and Moxon, 1972). The addition of an optimal level of external noise induces stochastic responses and enhances the signal detection and discrimination (Morse and Evans, 1996; Zeng et al., 2000). This suggests that it may be possible to improve hearing and speech comprehension using cochlear implants by means of the addition of noise. A theoretical study confirmed this indication and showed additionally that suprathreshold resonance provides a mechanism which can improve information transmission in cochlear implants (Stocks et al., 2002). Further studies also showed that noise is able to increase the dynamic range of patients with implanted cochlear implants as well as to improve their ability to encode temporal information (Morse and Evans, 1999a,b; Matsuoka et al., 2000).

References

- Abbott LF, Varela JA, Sen K, Nelson SB (1997) Synaptic depression and cortical gain control. *Science* 275:220–224. [16]
- Albert JT, Nadrowski B, Göpfert MC (2007) Mechanical signatures of transducer gating in the drosophila ear. *Curr. Biol.* 17:1000–1006. [16]
- Ashida G, Kubo M (2010) Suprathreshold stochastic resonance induced by ion channel fluctuation. *Physica D* 239:327 – 334. [12, 120]
- Averbeck BB, Latham PE, Pouget A (2006) Neural correlations, population coding and computation. *Nat. Rev. Neurosci.* 7:358–366. [120]
- Averbeck BB, Lee D (2004) Coding and transmission of information by neural ensembles. *Trends Neurosci.* 27:225–230. [120]
- Avila-Akerberg O, Chacron MJ (2011) Nonrenewal spike train statistics: causes and functional consequences on neural coding. *Exp. Brain Res.* 210:353–371. [120]
- Avissar M, Furman AC, Saunders JC, Parsons TD (2007) Adaptation reduces spike-count reliability, but not spike-timing precision, of auditory nerve responses. *J. Neurosci.* 27:6461–6472. [17, 43]
- Baccus SA, Meister M (2002) Fast and slow contrast adaptation in retinal circuitry. *Neuron* 36:909 – 919. [39, 85]
- Bair W, Koch C (1996) Temporal precision of spike trains in extrastriate cortex of the behaving macaque monkey. *Neural Comput.* 8:1185–1202. [3]
- Begenisich T, Stevens CF (1975) How many conductance states do potassium channels have? *Biophys. J.* 15:843–846. [7]
- Benda J, Bethge M, Hennig M, Pawelzik K, Herz A (2001) Spike-frequency adaptation: phenomenological model and experimental tests. *Neurocomput.* 38–40:105–110. [30, 44, 75, 109, 112]
- Benda J, Hennig RM (2008) Spike-frequency adaptation generates intensity invariance in a primary auditory interneuron. *J. Comput. Neurosci.* 24:113–136. [61]
- Benda J, Herz AVM (2003) A universal model for spike-frequency adaptation. *Neural Comput.* 15:2523–2564. [80, 94, 95, 96, 101, 102, 112, 117]
- Benda J, Longtin A, Maler L (2005) Spike-frequency adaptation separates transient communication signals from background oscillations. *J. Neurosci.* 25:2312–2321. [15,

- 61, 85]
- Benda J, Maler L, Longtin A (2010) Linear versus nonlinear signal transmission in neuron models with adaptation currents or dynamic thresholds. *J. Neurophysiol.* 104:2806–2820. [61, 68, 110]
- Benzi R, Sutera A, Vulpiani A (1981) The mechanism of stochastic resonance. *J. Phys. A* 14:L453. [11]
- Berg HC, Purcell EM (1977) Physics of chemoreception. *Biophys. J.* 20:193–219. [6]
- Berry MJ, Meister M (1998) Refractoriness and neural precision. *J. Neurosci.* 18:2200–2211. [113]
- Berry MJ, Warland DK, Meister M (1997) The structure and precision of retinal spike trains. *Proc. Natl. Acad. Sci. USA* 94:5411–5416. [3, 43]
- Bezrukov SM, Vodyanoy I (1995) Noise-induced enhancement of signal transduction across voltage-dependent ion channels. *Nature* 378:362–364. [12, 119]
- Bialek W, Setayeshgar S (2008) Cooperativity, sensitivity, and noise in biochemical signaling. *Phys. Rev. Lett.* 100:258101. [6]
- Birk JR (1972) Enhanced specificity of information in axons with negatively correlated adjacent interspike intervals. *Biol. Cybern.* 10:201–203. [121]
- Braun HA, Schäfer K, Voigt K, Peters R, Bretschneider F, Pei X, Wilkens L, Moss F (1997) Low-dimensional dynamics in sensory biology. 1: Thermally sensitive electroreceptors of the catfish. *J. Comput. Neurosci.* 4:335–347. [12]
- Braun HA, Wissing H, Schäfer K, Hirsch MC (1994) Oscillation and noise determine signal transduction in shark multimodal sensory cells. *Nature* 367:270–273. [12]
- Britten KH, Newsome WT, Shadlen MN, Celebrini S, Movshon JA (1996) A relationship between behavioral choice and the visual responses of neurons in macaque MT. *Vis. Neurosci.* 13:87–100. [43]
- Brown DA, Adams PR (1980) Muscarinic suppression of a novel voltage-sensitive K^+ current in a vertebrate neurone. *Nature* 283:673–676. [16, 112]
- Brumm H, Voss K, Köllmer I, Todt D (2004) Acoustic communication in noise: regulation of call characteristics in a new world monkey. *J. Exp. Biol.* 207:443–448. [5]
- Bryant HL, Segundo JP (1976) Spike initiation by transmembrane current: a white-noise analysis. *J. Physiol.* 260:279–314. [3]
- Calvin WH, Stevens CF (1967) Synaptic noise as a source of variability in the interval between action potentials. *Science* 155:842–844. [5, 43]
- Calvin WH, Stevens CF (1968) Synaptic noise and other sources of randomness in motoneuron interspike intervals. *J. Neurophysiol.* 31:574–587. [5]
- Castillo JD, Katz B (1954) Quantal components of the end-plate potential. *J. Physiol.* 124:560–573. [5]
- Chacron MJ, Longtin A, Maler L (2001) Negative interspike interval correlations increase the neuronal capacity for encoding time-dependent stimuli. *J. Neurosci.* 21:5328–5343. [14, 48, 61, 110, 117, 121]
- Chacron MJ, Longtin A, St-Hilaire M, Maler L (2000) Suprathreshold stochastic firing dynamics with memory in P-type electroreceptors. *Phys. Rev. Lett.* 85:1576–1579. [61, 110]

-
- Chacron MJ, Lindner B, Longtin A (2004) Noise shaping by interval correlations increases information transfer. *Phys. Rev. Lett.* 92:080601. [15, 61, 117]
- Chacron MJ, Lindner B, Longtin A (2007) Threshold fatigue and information transfer. *J. Comput. Neurosci.* 23:301–311. [110]
- Chance FS, Nelson SB, Abbott LF (1998) Synaptic depression and the temporal response characteristics of V1 cells. *J. Neurosci.* 18:4785–4799. [16]
- Chow CC, White JA (1996) Spontaneous action potentials due to channel fluctuations. *Biophys. J.* 71:3013–3021. [43, 113]
- Collins JJ, Chow CC, Imhoff TT (1995) Stochastic resonance without tuning. *Nature* 376:236–238. [119]
- Colquhoun D, Hawkes AG (1977) Relaxation and fluctuations of membrane currents that flow through drug-operated channels. *Proc. R. Soc. Lond. B Biol. Sci.* 199:231–262. [6]
- Cordo P, Inglis JT, Verschueren S, Collins JJ, Merfeld DM, Rosenblum S, Buckley S, Moss F (1996) Noise in human muscle spindles. *Nature* 383:769–770. [12]
- Corey DP, Hudspeth AJ (1983) Kinetics of the receptor current in bullfrog saccular hair cells. *J. Neurosci.* 3:962–976. [53]
- Cox DR, Lewis PAW (1966) *The statistical analysis of series of events*. Chapman and Hall, London. [26, 76, 115]
- de Ruyter van Steveninck RR, Lewen GD, Strong SP, Koberle R, Bialek W (1997) Reproducibility and variability in neural spike trains. *Science* 275:1805–1808. [3, 43]
- Demmer H, Kloppenburg P (2009) Intrinsic membrane properties and inhibitory synaptic input of kenyon cells as mechanisms for sparse coding? *J. Neurophysiol.* 102:1538–1550. [15]
- Dorval AD, White JA (2005) Channel noise is essential for perithreshold oscillations in entorhinal stellate neurons. *J. Neurosci.* 25:10025–10028. [113]
- Douglass JK, Wilkens L, Pantazelou E, Moss F (1993) Noise enhancement of information transfer in crayfish mechanoreceptors by stochastic resonance. *Nature* 365:337–340. [12, 119]
- Duchamp-Viret P, Kostal L, Chaput M, Lánský P, Rospars JP (2005) Patterns of spontaneous activity in single rat olfactory receptor neurons are different in normally breathing and tracheotomized animals. *J. Neurobiol.* 65:97–114. [43]
- Eaton RA (2000) Adaptation in hair cells. *Annu. Rev. Neurosci.* 23:285–314. [119]
- Ehrenstein G, Lecar H, Nossal R (1970) The nature of the negative resistance in biomolecular lipid membranes containing excitability-inducing material. *J. Gen. Physiol.* 55:119–133. [7]
- Engel TA, Schimansky-Geier L, Herz AVM, Schreiber S, Erchova I (2008) Subthreshold membrane-potential resonances shape spike-train patterns in the entorhinal cortex. *J. Neurophysiol.* 100:1576–1589. [61]
- Epping WJ (1990) Influence of adaptation on neural sensitivity to temporal characteristics of sound in the dorsal medullary nucleus and torus semicircularis of the grassfrog. *Hear. Res.* 45:1–13. [15]
- Ermentrout B (1998) Linearization of F-I curves by adaptation. *Neural Comput.* 10:1721–1729. [29, 30, 39, 100, 111]

- Ermentrout B, Pascal M, Gutkin B (2001) The effects of spike frequency adaptation and negative feedback on the synchronization of neural oscillators. *Neural Comput.* 13:1285–1310. [35, 66]
- Faber DS, Young WS, Legendre P, Korn H (1992) Intrinsic quantal variability due to stochastic properties of receptor-transmitter interactions. *Science* 258:1494–1498. [5]
- Faber ESL, Sah P (2003) Calcium-activated potassium channels: Multiple contributions to neuronal function. *Neuroscientist* 9:181–194. [116]
- Fairhall AL, Lewen GD, Bialek W, de Ruyter Van Steveninck RR (2001a) Efficiency and ambiguity in an adaptive neural code. *Nature* 412:787–792. [39, 85]
- Fairhall AL, Lewen GD, Bialek W, de Ruyter van Steveninck RR (2001b) Multiple timescales of adaptation in a neural code. *NIPS* 13:124–130. [39, 85]
- Faisal AA, Selen LPJ, Wolpert DM (2008) Noise in the nervous system. *Nat. Rev. Neurosci.* 9:292–303. [5, 43]
- Fano U (1947) Ionization yield of radiations. II. The fluctuations of the number of ions. *Phys. Rev.* 72:26–29. [26]
- Farkhooi F, Muller E, Nawrot MP (2011) Adaptation reduces variability of the neuronal population code. *Phys. Rev. E* 83:050905. [15]
- Farkhooi F, Strube-Bloss MF, Nawrot MP (2009) Serial correlation in neural spike trains: Experimental evidence, stochastic modeling, and single neuron variability. *Phys. Rev. E* 79:021905. [110]
- Finlayson PG, Adam TJ (1997) Excitatory and inhibitory response adaptation in the superior olive complex affects binaural acoustic processing. *Hear. Res.* 103:1–18. [16]
- Fleidervish IA, Friedman A, Gutnick MJ (1996) Slow inactivation of Na⁺ current and slow cumulative spike adaptation in mouse and guinea-pig neocortical neurones in slices. *J. Physiol.* 493 (Pt 1):83–97. [16, 112]
- Flyvbjerg H, Petersen HG (1989) Error estimates on averages of correlated data. *J. Chem. Phys.* 91:461–466. [110]
- Franks KM, Stevens CF, Sejnowski TJ (2003) Independent sources of quantal variability at single glutamatergic synapses. *J. Neurosci.* 23:3186–3195. [5]
- Frehland E, Faulhaber KH (1980) Nonequilibrium ion transport through pores. The influence of barrier structures on current fluctuations, transient phenomena and admittance. *Biophys. Struct. Mech.* 7:1–16. [5]
- French AS (1987) Removal of rapid sensory adaptation from an insect mechanoreceptor neuron by oxidizing agents which affect sodium channel inactivation. *J. Comp. Physiol. A* 161:275–282. [39, 85, 112]
- French AS (1988) Transduction mechanisms of mechanosensilla. *Annu. Rev. Entomol.* 33:39–58. [18]
- French AS (1989) Ouabain selectively affects the slow component of sensory adaptation in an insect mechanoreceptor. *Brain Res.* 504:112–114. [39, 85, 112]
- Gabbiani F, Krapp HG (2006) Spike-frequency adaptation and intrinsic properties of an identified, looming-sensitive neuron. *J. Neurophysiol.* 96:2951–2962. [15, 61, 110, 112]
- Geisler CD, Goldberg JM (1966) A stochastic model of the repetitive activity of neurons. *Biophys. J.* 6:53–69. [61]

- Gerstein GL, Mandelbrot B (1964) Random walk models for the spike activity of a single neuron. *Biophys. J.* 4:41–68. [24, 37, 47, 87, 109]
- Gibson MA, Bruck J (2000) Efficient exact stochastic simulation of chemical systems with many species and many channels. *J. Phys. Chem. A* 104:1876–1889. [34]
- Gillespie DT (1976) A general method for numerically simulating the stochastic time evolution of coupled chemical reactions. *J. Comp. Phys.* 22:403–434. [34]
- Gillespie PG, Walker RG (2001) Molecular basis of mechanosensory transduction. *Nature* 413:194–202. [18]
- Gillespie PG (2004) Myosin I and adaptation of mechanical transduction by the inner ear. *Philos. Trans. R. Soc. Lond. B Biol. Sci.* 359:1945–1951. [119]
- Givois V, Pollack GS (2000) Sensory habituation of auditory receptor neurons: implications for sound localization. *J. Exp. Biol.* 203:2529–2537. [15]
- Glantz RM, Schroeter JP (2004) Analysis and simulation of gain control and precision in crayfish visual interneurons. *J. Neurophysiol.* 92:2747–2761. [61]
- Goense JBM, Ratnam R (2003) Continuous detection of weak sensory signals in afferent spike trains: the role of anti-correlated interspike intervals in detection performance. *J. Comp. Physiol. A* 189:741–759. [121]
- Gollisch T, Herz AMV (2005) Disentangling sub-millisecond processes within an auditory transduction chain. *PLoS Biol.* 3:e8. [18, 20, 30, 31, 44, 53, 114]
- Gollisch T, Herz AVM (2004) Input-driven components of spike-frequency adaptation can be unmasked in vivo. *J. Neurosci.* 24:7435–7444. [16, 44, 112, 114]
- Gollisch T, Schütze H, Benda J, Herz AVM (2002) Energy integration describes sound-intensity coding in an insect auditory system. *J. Neurosci.* 22:10434–10448. [18, 44, 114]
- Granit R, Kernell D, Shortess GK (1963) Quantitative aspects of repetitive firing of mammalian motoneurons, caused by injected currents. *J. Physiol.* 168:911–931. [-]
- Gray EG (1960) The fine structure of the insect ear. *Philos. Trans. R. Soc. Lond. B Biol. Sci.* 243:75–94. [18, 31, 44, 51, 112]
- Grewe J, Kretzberg J, Warzecha AK, Egelhaaf M (2003) Impact of photon noise on the reliability of a motion-sensitive neuron in the fly's visual system. *J. Neurosci.* 23:10776–10783. [5, 43]
- Grewe J, Weckström M, Egelhaaf M, Warzecha AK (2007) Information and discriminability as measures of reliability of sensory coding. *PLoS ONE* 2:e1328. [5]
- Hessler NA, Shirke AM, Malinow R (1993) The probability of transmitter release at a mammalian central synapse. *Nature* 366:569–572. [43]
- Hill KG (1983) The physiology of locust auditory receptors. I. Discrete depolarizations of receptor cells. *J. Comp. Physiol. A* 152:475–482. [18, 19]
- Hille B (2001) *Ion Channels of Excitable Membranes*. Sinauer Associates Inc., U.S, 3rd edition. [6]
- Hodgkin AL, Huxley AF (1952) A quantitative description of membrane current and its application to conduction and excitation in nerve. *J. Physiol.* 117:500–544. [6]
- Holton T, Hudspeth AJ (1986) The transduction channel of hair cells from the bull-frog characterized by noise analysis. *J. Physiol.* 375:195–227. [113]

- Howard J, Hudspeth AJ (1988) Compliance of the hair bundle associated with gating of mechano-electrical transduction channels in the bullfrog's saccular hair cell. *Neuron* 1:189–199. [31, 53, 113]
- Hudspeth AJ, Choe Y, Mehta AD, Martin P (2000) Putting ion channels to work: Mechano-electrical transduction, adaptation, and amplification by hair cells. *Proc. Natl. Acad. Sci. USA* 97:11765–11772. [16, 31, 53]
- Indresano AA, Frank JE, Middleton P, Jaramillo F (2003) Mechanical noise enhances signal transmission in the bullfrog sacculus. *JARO* 4:363–370. [119]
- Ingham NJ, McAlpine D (2004) Spike-frequency adaptation in the inferior colliculus. *J. Neurophysiol.* 91:632–645. [17]
- Ingham NJ, McAlpine D (2005) GABAergic inhibition controls neural gain in inferior colliculus neurons sensitive to interaural time differences. *J. Neurosci.* 25:6187–6198. [16]
- Jaramillo F, Wiesenfeld K (1998) Mechano-electrical transduction assisted by Brownian motion: A role for noise in the auditory system. *Nat. Neurosci.* 1:384–388. [6, 119]
- Jaramillo F, Wiesenfeld K (2000) Physiological noise level enhances mechano-electrical transduction in hair cells. *Chaos Solitons Fractals* 11:1869 – 1874. [119]
- Johnson JB (1928) Thermal agitation of electricity in conductors. *Phys. Rev.* 32:97. [5]
- Joris PX, Schreiner CE, Rees A (2004) Neural processing of amplitude-modulated sounds. *Physiol. Rev.* 84:541–577. [17]
- Kara P, Reinagel P, Reid RC (2000) Low response variability in simultaneously recorded retinal, thalamic, and cortical neurons. *Neuron* 27:635–646. [3, 11, 43]
- Kiang NY, Moxon EC (1972) Physiological considerations in artificial stimulation of the inner ear. *Ann. Otol. Rhinol. Laryngol.* 81:714–730. [121]
- Kim KJ, Rieke F (2003) Slow Na⁺ inactivation and variance adaptation in salamander retinal ganglion cells. *J. Neurosci.* 23:1506–1516. [16]
- Knight BW (1972) Dynamics of encoding in a population of neurons. *J. Gen. Physiol.* 59:734–766. [-]
- Kostál L, Lánský P (2008) Randomness of spontaneous activity and information transfer in neurons. *Physiol. Res.* 57 Suppl 3:S133–S138. [3]
- Krahe R, Ronacher B (1993) Long rise times of sound pulses in grasshopper songs improve the directionality cues received by the CNS from the auditory receptors. *J. Comp. Physiol. A* 173:425–434 10.1007/BF00193515. [18]
- Kreiman G, Krahe R, Metzner W, Koch C, Gabbiani F (2000) Robustness and variability of neuronal coding by amplitude-sensitive afferents in the weakly electric fish *eigenmannia*. *J. Neurophysiol.* 84:189–204. [43]
- Kung C (2005) A possible unifying principle for mechanosensation. *Nature* 436:647–654. [6]
- Kuznetsova MS, Higgs MH, Spain WJ (2008) Adaptation of firing rate and spike-timing precision in the avian cochlear nucleus. *J. Neurosci.* 28:11906–11915. [17]
- Laughlin SB (1989) The role of sensory adaptation in the retina. *J. Exp. Biol.* 146:39–62. [15]
- Laughlin SB, de Ruyter van Steveninck RR, Anderson JC (1998) The metabolic cost of

- neural information. *Nat. Neurosci.* 1:36–41. [120]
- Laughlin SB, Lillywhite PG (1982) Intrinsic noise in locust photoreceptors. *J. Physiol.* 332:25–45. [43]
- Lecar H, Nossal R (1971) Theory of threshold fluctuations in nerves. II. Analysis of various sources of membrane noise. *Biophys. J.* 11:1068–1084. [6, 51, 112]
- Levin JE, Miller JP (1996) Broadband neural encoding in the cricket cercal sensory system enhanced by stochastic resonance. *Nature* 380:165–168. [12, 119]
- Levine MW, Shefner JM (1977) A model for the variability of interspike intervals during sustained firing of a retinal neuron. *Biophys. J.* 19:241–252. [43]
- Levine MW (2007) Variability in the firing of retinal ganglion cells of goldfish: A review. *Vis. Neurosci.* 24:239–246. [43]
- Lillywhite PG, Laughlin SB (1979) Transducer noise in a photoreceptor. *Nature* 277:569–572. [43]
- Lindner B (2004) Interspike interval statistics of neurons driven by colored noise. *Phys. Rev. E* 69:022901. [25, 37, 48, 109, 110, 115]
- Lindner B, Chacron MJ, Longtin A (2005a) Integrate-and-fire neurons with threshold noise: a tractable model of how interspike interval correlations affect neuronal signal transmission. *Phys. Rev. E* 72:021911. [61]
- Lindner JF, Bennett M, Wiesenfeld K (2005b) Stochastic resonance in the mechano-electrical transduction of hair cells. *Phys. Rev. E* 72:051911. [119]
- Liu YH, Wang XJ (2001) Spike-frequency adaptation of a generalized leaky integrate-and-fire model neuron. *J. Comput. Neurosci.* 10:25–45. [48, 61, 68, 110, 111]
- Longtin A, Laing C, Chacron M (2003) Correlations and memory in neurodynamical systems In Rangarajan G, Ding M, editors, *Processes with Long-Range Correlations*, Vol. 621 of *Lecture Notes in Physics*, pp. 286–308. Springer Berlin / Heidelberg. [121]
- Lowen SB, Teich MC (1992) Auditory-nerve action potentials form a nonrenewal point process over short as well as long time scales. *J. Acoust. Soc. Am.* 92:803–806. [110]
- Lowen SB, Teich MC (1995) Estimation and simulation of fractal stochastic point processes. *Fractals* 3:183–210. [117]
- Machens CK, Stemmler MB, Prinz P, Krahe R, Ronacher B, Herz AV (2001) Representation of acoustic communication signals by insect auditory receptor neurons. *J. Neurosci.* 21:3215–3227. [18, 43, 113, 120]
- Machens CK, Gollisch T, Kolesnikova O, Herz AVM (2005) Testing the efficiency of sensory coding with optimal stimulus ensembles. *Neuron* 47:447–456. [43]
- Machens CK, Schütze H, Franz A, Kolesnikova O, Stemmler MB, Ronacher B, Herz AVM (2003) Single auditory neurons rapidly discriminate conspecific communication signals. *Nat. Neurosci.* 6:341–342. [18]
- Madison DV, Nicoll RA (1984) Control of the repetitive discharge of rat CA 1 pyramidal neurones in vitro. *J. Physiol.* 354:319–331. [16, 112]
- Mainen ZF, Sejnowski TJ (1995) Reliability of spike timing in neocortical neurons. *Science* 268:1503–1506. [3]
- Manley JA, Müller-Preuss P (1978) Response variability of auditory cortex cells in the squirrel monkey to constant acoustic stimuli. *Exp. Brain Res.* 32:171–180. [17]

- Manwani A, Koch C (1999) Detecting and estimating signals in noisy cable structure. I: Neuronal noise sources. *Neural Comput.* 11:1797–1829. [6, 51, 112]
- Matsuoka AJ, Abbas PJ, Rubinstein JT, Miller CA (2000) The neuronal response to electrical constant-amplitude pulse train stimulation: additive Gaussian noise. *Hear. Res.* 149:129–137. [121]
- McDonnell MD, Abbott D (2009) What is stochastic resonance? Definitions, misconceptions, debates, and its relevance to biology. *PLoS Comput. Biol.* 5:e1000348. [11]
- Michelsen, Rohrseitz (1995) Directional sound processing and interaural sound transmission in a small and a large grasshopper. *J. Exp. Biol.* 198:1817–1827. [31]
- Michelsen A (1971) The physiology of the locust ear. I. Frequency sensitivity of single cells in the isolated ear. *J. Comp. Physiol. A* 71:49–62. [18, 31]
- Middleton JW, Chacron MJ, Lindner B, Longtin A (2003) Firing statistics of a neuron model driven by long-range correlated noise. *Phys. Rev. E* 68:021920. [14, 26, 37, 76, 77, 78, 79, 80, 86, 87, 88, 110, 115, 116, 121]
- Morse RP, Evans EF (1996) Enhancement of vowel coding for cochlear implants by addition of noise. *Nat. Med.* 2:928–932. [121]
- Morse RP, Evans EF (1999a) Additive noise can enhance temporal coding in a computational model of analogue cochlear implant stimulation. *Hear. Res.* 133:107–119. [121]
- Morse RP, Evans EF (1999b) Preferential and non-preferential transmission of formant information by an analogue cochlear implant using noise: the role of the nerve threshold. *Hear. Res.* 133:120–132. [121]
- Muller E, Buesing L, Schemmel J, Meier K (2007) Spike-frequency adapting neural ensembles: beyond mean adaptation and renewal theories. *Neural Comput.* 19:2958–3010. [61]
- Nadrowski B, Albert JT, Göpfert MC (2008) Transducer-based force generation explains active process in *Drosophila* hearing. *Curr. Biol.* 18:1365–1372. [113]
- Nadrowski B, Martin P, Jülicher F (2004) Active hair-bundle motility harnesses noise to operate near an optimum of mechanosensitivity. *Proc. Natl. Acad. Sci. USA* 101:12195–12200. [6]
- Neher E, Stevens CF (1977) Conductance fluctuations and ionic pores in membranes. *Annu. Rev. Biophys. Bioeng.* 6:345–381. [8, 33, 43]
- Nelken I, Fishbach A, Las L, Ulanovsky N, Farkas D (2003) Primary auditory cortex of cats: feature detection or something else? *Biol. Cybern.* 89:397–406 10.1007/s00422-003-0445-3. [85]
- Nelson ME, Maciver MA (1999) Prey capture in the weakly electric fish *Apteronotus albifrons*: sensory acquisition strategies and electrosensory consequences. *J. Exp. Biol.* 202:1195–1203. [117]
- Nelson ME, Xu Z, Payne JR (1997) Characterization and modeling of P-type electrosensory afferent responses to amplitude modulations in a wave-type electric fish. *J. Comp. Physiol. A* 181:532–544. [15, 39, 85]
- Nozaki D, Mar DJ, Grigg P, Collins JJ (1999) Effects of colored noise on stochastic resonance in sensory neurons. *Phys. Rev. Lett.* 82:2402–2405. [119]

- Parc YW, Koh DS, Sung W (2009) Stochastic resonance in an ion channel following the non-arrhenius gating rate. *Eur. Phys. J. B* 69:127–131 10.1140/epjb/e2009-00116-5. [12]
- Pearson KG, Robertson RM (1981) Interneurons coactivating hindleg flexor and extensor motoneurons in the locust. *J. Comp. Physiol. A* 144:391–400. [23]
- Peron S, Gabbiani F (2009a) Spike frequency adaptation mediates looming stimulus selectivity in a collision-detecting neuron. *Nat. Neurosci.* 12:318–326. [15, 61, 85]
- Peron SP, Gabbiani F (2009b) Role of spike-frequency adaptation in shaping neuronal response to dynamic stimuli. *Biol. Cybern.* 100:505–520. [61]
- Pollack GS (1988) Selective attention in an insect auditory neuron. *J. Neurosci.* 8:2635–2639. [85]
- Popov AV, Svetlogorskaya ID (1972) Receptor interaction and ultrastructural organization of the auditory nerve in *Locusta migratoria*. *Neurosci. Behav. Physiol.* 5:282–288. [18]
- Pouget A, Dayan P, Zemel R (2000) Information processing with population codes. *Nat. Rev. Neurosci.* 1:125–132. [120]
- Prut Y, Perlmutter SI (2003) Firing properties of spinal interneurons during voluntary movement. I. State-dependent regularity of firing. *J. Neurosci.* 23:9600–9610. [3, 11]
- Ratnam R, Nelson ME (2000) Nonrenewal statistics of electrosensory afferent spike trains: Implications for the detection of weak sensory signals. *J. Neurosci.* 20:6672–6683. [61, 110, 121]
- Richard DG, Wiley RH (1980) Reverberations and amplitude fluctuations in the propagation in the forest: Implications for animal communication. *Am. Zool.* 115:381–399. [5]
- Risken H (1996) *The Fokker-Planck Equation: Methods of Solutions and Applications*. Springer, 2nd edition. [87]
- Robert D, Göpfert MC (2002) Novel schemes for hearing and orientation in insects. *Curr. Opin. Neurobiol.* 12:715–720. [18]
- Rokem A, Watzl S, Gollisch T, Stemmler M, Herz AVM, Samengo I (2006) Spike-timing precision underlies the coding efficiency of auditory receptor neurons. *J. Neurophysiol.* 95:2541–2552. [18, 43, 113]
- Ronacher B, Franz A, Wohlgemuth S, Hennig RM (2004) Variability of spike trains and the processing of temporal patterns of acoustic signals - problems, constraints, and solutions. *J. Comp. Physiol. A* 190:257–277. [15, 19, 43, 113]
- Ronacher B, Krahe R (1998) Song recognition in the grasshopper *Chorthippus biguttulus* is not impaired by shortening song signals: implications for neuronal encoding. *J. Comp. Physiol. A* 183:729–735 10.1007/s003590050295. [118]
- Ronacher B, Krahe R (2000) Temporal integration vs. parallel processing: Coping with the variability of neuronal messages in directional hearing of insects. *Euro. J. Neurosci.* 12:2147–2156. [118]
- Ronacher B, Krahe R, Hennig RM (2000) Effects of signal duration on the recognition of masked communication signals by the grasshopper *Chorthippus biguttulus*. *J. Comp. Physiol. A* 186:1065–1072. [-]
- Ronacher B, Wohlgemuth S, Vogel A, Krahe R (2008) Discrimination of acoustic com-

- munication signals by grasshoppers (*Chorthippus biguttulus*): Temporal resolution, temporal integration, and the impact of intrinsic noise. *J. Comp. Physiol.* 122:252–263. [3, 11, 113, 118]
- Rose D (1979) An analysis of the variability of unit activity in the cat's visual cortex. *Exp. Brain Res.* 37:595–604. [3]
- Rospars JP, Lánský P, Vaillant J, Duchamp-Viret P, Duchamp A (1994) Spontaneous activity of first- and second-order neurons in the frog olfactory system. *Brain Res.* 662:31–44. [43]
- Rubinstein JT, Miller CA (1999) How do cochlear prostheses work? *Curr. Opin. Neurobiol.* 9:399–404. [121]
- Russell DF, Wilkens LA, Moss F (1999) Use of behavioural stochastic resonance by paddle fish for feeding. *Nature* 402:291–294. [12]
- Römer H (1976) Die Informationsverarbeitung tympanaler Rezeptorelemente von *Locusta migratoria* (Acrididae, Orthoptera). *J. Comp. Physiol. A* 109:101–122. [18, 31, 44, 75, 109]
- Römer H, Lewald J (1992) High-frequency sound transmission in natural habitats: Implications for the evolution of insect acoustic communication. *Behav. Ecol. Sociobiol.* 29:437–444 10.1007/BF00170174. [5]
- Sah P (1996) Ca^{2+} -activated K^{+} currents in neurones: types, physiological roles and modulation. *Trends Neurosci.* 19:150–154. [116]
- Sah P, Davies P (2000) Calcium-activated potassium currents in mammalian neurons. *Clin. Exp. Pharmacol. Physiol.* 27:657–663. [16, 112]
- Sakmann B, Neher E (1995) *Single-Channel Recording*. New York: Plenum Press, 2nd edition. [6]
- Sakurai Y (1996) Population coding by cell assemblies—what it really is in the brain. *Neurosci. Res.* 26:1–16. [120]
- Sawczuk A, Powers RK, Binder MD (1995) Spike frequency adaptation studied in hypoglossal motoneurons of the rat. *J. Neurophysiol.* 73:1799–1810. [85]
- Sawczuk A, Powers RK, Binder MD (1997) Contribution of outward currents to spike-frequency adaptation in hypoglossal motoneurons of the rat. *J. Neurophysiol.* 78:2246–2253. [85]
- Schaette R, Gollisch T, Herz AVM (2005) Spike-train variability of auditory neurons in vivo: Dynamic responses follow predictions from constant stimuli. *J. Neurophysiol.* 93:3270–3281. [17, 18, 19, 43, 44, 109, 110, 113]
- Schiolten P, Larsen ON, Michelsen A (1981) Mechanical time resolution in some insect ears. *J. Comp. Physiol. A* 143:289–295 10.1007/BF00611164. [18]
- Schneidman E, Freedman B, Segev I (1998) Ion channel stochasticity may be critical in determining the reliability and precision of spike timing. *Neural Comput.* 10:1679–1703. [52, 57, 113]
- Schreiber S, Machens CK, Herz AVM, Laughlin SB (2002) Energy-efficient coding with discrete stochastic events. *Neural Comput.* 14:1323–1346. [120]
- Schwalger T, Lindner B (2010) Theory for serial correlations of interevent intervals. *Eur. Phys. J. Spec. Top.* 187:211–221 10.1140/epjst/e2010-01286-y. [61]

- Schwalger T, Fisch K, Benda J, Lindner B (2010) How noisy adaptation of neurons shapes interspike interval histograms and correlations. *PLoS Comput. Biol.* 6:e1001026. [25, 26, 37, 47, 48, 62, 63, 64, 67, 68, 79, 85, 86, 89, 90, 110, 111, 112, 114, 115]
- Schwalger T, Lindner B (2008) Higher-order statistics of a bistable system driven by dichotomous colored noise. *Phys. Rev. E* 78:021121. [69]
- Shadlen MN, Newsome WT (1994) Noise, neural codes and cortical organization. *Curr. Opin. Neurobiol.* 4:569–579. [5]
- Shadlen MN, Newsome WT (1998) The variable discharge of cortical neurons: implications for connectivity, computation, and information coding. *J. Neurosci.* 18:3870–3896. [5]
- Shannon RV, Zeng FG, Kamath V, Wygonski J, Ekelid M (1995) Speech recognition with primarily temporal cues. *Science* 270:303–304. [17]
- Sigworth FJ (1980) The variance of sodium current fluctuations at the node of ranvier. *J. Physiol.* 307:97–129. [7, 43, 53, 55, 57, 113]
- Sobel EC, Tank DW (1994) In vivo Ca^{2+} dynamics in a cricket auditory neuron: An example of chemical computation. *Science* 263:823–826. [15, 61, 85]
- Softky WR, Koch C (1993) The highly irregular firing of cortical cells is inconsistent with temporal integration of random epsps. *J. Neurosci.* 13:334–350. [3]
- Spain WJ, Schwindt PC, Crill WE (1991a) Post-inhibitory excitation and inhibition in layer V pyramidal neurones from cat sensorimotor cortex. *J. Physiol.* 434:609–626. [85]
- Spain WJ, Schwindt PC, Crill WE (1991b) Two transient potassium currents in layer V pyramidal neurones from cat sensorimotor cortex. *J. Physiol.* 434:591–607. [85]
- Stocks NG (2000) Suprathreshold stochastic resonance in multilevel threshold systems. *Phys. Rev. Lett.* 84:2310–2313. [12, 120]
- Stocks NG, Allingham D, Morse RP (2002) The application of suprathreshold stochastic resonance to cochlear implant coding. *Fluct. Noise Lett.* 2:L169–L181. [121]
- Storm JF (1990) Potassium currents in hippocampal pyramidal cells. *Prog. Brain. Res.* 83:161–187. [16]
- Stumpner A, Ronacher B (1991) Auditory interneurons in the metathoracic ganglion of the grasshopper *Chorthippus biguttulus*: I. Morphological and physiological characterization. *J. Exp. Biol.* 158:391–410. [18]
- Stumpner A, Ronacher B, Helvesen Ov (1991) Auditory interneurons in the metathoracic ganglion of the grasshopper *Chorthippus biguttulus*: II. Processing of temporal patterns of the song of the male. *J. Exp. Biol.* 158:411–430. [18]
- Sugano N, Tsukada M (1978) Effect of correlated adjacent interspike interval sequences of the excitatory motor axon on the opening movement of the crayfish claw opener muscles. *Biol. Cybern.* 29:63–67. [120, 121]
- Teich MC (1989) Fractal character of the auditory neural spike train. *IEEE Trans. Biomed. Eng.* 36:150–160. [117]
- Teich MC, Heneghan C, Lowen SB, Ozaki T, Kaplan E (1997) Fractal character of the neural spike train in the visual system of the cat. *J. Opt. Soc. Am. A* 14:529–546. [26, 76, 117]
- Teich MC, Khanna SM (1985) Pulse-number distribution for the neural spike train in the

- cat's auditory nerve. *J. Acoust. Soc. Am.* 77:1110–1128. [43]
- Tolhurst DJ, Movshon JA, Dean AF (1983) The statistical reliability of signals in single neurons in cat and monkey visual cortex. *Vision Res.* 23:775–785. [43]
- Torkkeli PH, Sekizawa S, French AS (2001) Inactivation of voltage-activated Na⁺ currents contributes to different adaptation properties of paired mechanosensory neurons. *J. Neurophysiol.* 85:1595–1602. [16, 112]
- Tweedie MCK (1947) Functions of a statistical variate with given means, with special reference to Laplacian distributions. *Proc. Camb. Philol. Soc.* 43:41–49. [24]
- Ulanovsky N, Las L, Farkas D, Nelken I (2004) Multiple time scales of adaptation in auditory cortex neurons. *J. Neurosci.* 24:10440–10453. [39, 85]
- van Rossum MCW, O'Brien BJ, Smith RG (2003) Effects of noise on the spike timing precision of retinal ganglion cells. *J. Neurophysiol.* 89:2406–2419. [51, 112, 113]
- Vergara C, Latorre R, Marrion NV, Adelman JP (1998) Calcium-activated potassium channels. *Curr. Opin. Neurobiol.* 8:321–329. [16]
- Vilela RD, Lindner B (2009) Are the input parameters of white noise driven integrate and fire neurons uniquely determined by rate and CV? *J. Theor. Biol.* 257:90–99. [24]
- Vilfan A, Duke T (2003) Two adaptation processes in auditory hair cells together can provide an active amplifier. *Biophys. J.* 85:191–203. [119]
- Vilin YY, Ruben PC (2001) Slow inactivation in voltage-gated sodium channels: Molecular substrates and contributions to channelopathies. *Cell Biochem. Biophys.* 35:171–190. [16]
- Villarroel A (1997) Nonstationary noise analysis of M currents simulated and recorded in PC12 cells. *J. Neurophysiol.* 77:2131–2138. [113]
- Vogel A, Hennig RM, Ronacher B (2005) Increase of neuronal response variability at higher processing levels as revealed by simultaneous recordings. *J. Neurophysiol.* 93:3548–3559. [3, 11, 43]
- von Helversen D (1972) Gesang des Männchens und Lautschema des Weibchens bei der Feldheuschrecke *Chorthippus biguttulus* (Orthoptera, Acrididae). *J. Comp. Physiol. A* 81:381–422 10.1007/BF00697757. [17]
- von Helversen D, von Helversen O (1997) Recognition of sex in the acoustic communication of the grasshopper *Chorthippus biguttulus* (Orthoptera, Acrididae). *J. Comp. Physiol. A* 180:373–386. [17]
- Wang HS, Pan Z, Shi W, Brown BS, Wymore RS, Cohen IS, Dixon JE, McKinnon D (1998) KCNQ2 and KCNQ3 potassium channel subunits: Molecular correlates of the M-channel. *Science* 282:1890–1893. [110]
- Wang XJ (1998) Calcium coding and adaptive temporal computation in cortical pyramidal neurons. *J. Neurophysiol.* 79:1549–1566. [61]
- Warzecha AK, Egelhaaf M (1999) Variability in spike trains during constant and dynamic stimulation. *Science* 283:1927–1930. [43]
- Westerman LA, Smith RL (1984) Rapid and short-term adaptation in auditory nerve responses. *Hear. Res.* 15:249–260. [15]
- White JA, Klink R, Alonso A, Kay AR (1998) Noise from voltage-gated ion channels may influence neuronal dynamics in the entorhinal cortex. *J. Neurophysiol.* 80:262–269. [12]

-
- White JA, Rubinstein JT, Kay AR (2000) Channel noise in neurons. *Trends Neurosci.* 23:131–137. [6, 7, 43, 113, 120]
- Wiesenfeld K, Moss F (1995) Stochastic resonance and the benefits of noise: from ice ages to crayfish and squids. *Nature* 373:33–36. [11, 119]
- Wimmer K, Hildebrandt KJ, Hennig RM, Obermayer K (2008) Adaptation and selective information transmission in the cricket auditory neuron AN2. *PLoS Comput. Biol.* 4:e1000182. [39, 85]
- Windmill JFC, Bockenhauer S, Robert D (2008) Time-resolved tympanal mechanics of the locust. *J. R. Soc. Interface* 5:1435–1443. [18]
- Xiang-Hui Z, Zhang-Cai L, Bing Z, Nan Y (2008) Suprathreshold stochastic resonance in mechano-electrical transduction of hair cells. *Chinese Phys. Lett.* 25:1490. [120]
- Xu Z, Payne JR, Nelson ME (1996) Logarithmic time course of sensory adaptation in electrosensory afferent nerve fibers in a weakly electric fish. *J. Neurophysiol.* 76:2020–2032. [39, 85]
- Zeng FG, Fu QJ, Morse R (2000) Human hearing enhanced by noise. *Brain Res.* 869:251–255. [119, 121]

Danksagung / Acknowledgments

Diese Doktorarbeit ist während meiner Tätigkeit als wissenschaftliche Mitarbeiterin am Lehrstuhl für Computational Neuroscience der Ludwig-Maximilians-Universität München entstanden. Den erfolgreichen Abschluss der vorliegenden Arbeit verdanke ich der Unterstützung vieler Menschen, die mich während der gesamten Zeit begleitet haben. Hiermit möchte ich die Gelegenheit nutzen, mich bei allen zu bedanken.

An erster Stelle möchte ich mich bei Jan Benda für das interessante Thema, mit dem ich Experiment und Theorie verbinden konnte, sowie für seine intensive Betreuung während der gesamten Zeit meiner Doktorarbeit bedanken.

Großen Dank gilt Andreas Herz für die offizielle Betreuung meiner Dissertation sowie für die Unterstützung und hilfreichen Anregungen.

Mein Dank geht auch an Tilo Schwalger und Benjamin Lindner am Max-Planck-Institut für Physik komplexer Systeme in Dresden für die erfolgreiche Kooperation, die nicht vorbildlicher hätte verlaufen können. Besonderer Dank gilt Tilo für die angenehme Zusammenarbeit und Beantwortung all meiner Fragen.

Ganz besonders möchte ich meiner gesamten Arbeitsgruppe, im Besonderen Jan Grewe, Jörg Henninger, Florian Walker und Henriette Walz, für das angenehme Arbeitsklima, die netten Ablenkungen und Unterhaltungen zwischendurch und für allerlei Hilfestellungen danken.

Mein Dank richtet sich auch an Rüdiger Krahe, der sich freundlicherweise bereit erklärt hat, Teile meiner Arbeit Korrektur zu lesen.

Für die Unterstützung in meinem privaten Umfeld bedanke ich mich besonders bei meiner Familie. Ihr habt mich in jeglicher Hinsicht unterstützt, stets an mich geglaubt und mir Rückhalt gegeben. Danke, dass ihr für mich da seid!

Karin Fisch



Informatikerin & Neurowissenschaftlerin

Alramstr. 25
81371 München

Geboren am 25. März 1981
in Saarburg, Rheinland-Pfalz

☎ (+49) 176 / 219 05 093
✉ k.fisch@ymail.com

curriculum vitae

BERUFSERFAHRUNG

- 02/2008 – heute **Ludwig-Maximilians-Universität München / Humboldt Universität Berlin**
Wissenschaftliche Mitarbeiterin
Promotion im Bereich „Computational Neuroscience“
Dissertation (Computersimulation & Elektrophysiologie): „The contribution of spike-frequency adaptation to the variability of spike responses in a sensory neuron“
- 01/2009 – 11/2009 **TomTec Imaging Systems GmbH**
Angestellte (Teilzeit) im Bereich Medizinische Bildverarbeitung

AUSBILDUNG

- 10/2004 – 11/2007 **Master in Neurowissenschaften an der Universität zu Köln**
Schwerpunkte: Neuroimaging, Elektrophysiologie, Pharmakologie
Masterarbeit (Computersimulation & Elektrophysiologie): „Untersuchungen zur Rolle und Funktion tarsaler sensorischer Signale bei der Laufmuster-generierung im Mittelbein der Stabheuschrecke Carausius morosus“, Tierphysiologie der Universität zu Köln
Abschluss: Master of Science
- 10/2000 – 08/2004 **Diplomstudium Angewandte Informatik an der Fachhochschule Trier**
Anwendungsfach: Medizin
Diplomarbeit im Bereich Medizinische Bildverarbeitung: „Verfahren zur operationellen STN-Lokalisation in MR-Bildern“, Institut für Innovative Informatik-Anwendungen der Fachhochschule Trier
Auszeichnung der Diplomarbeit durch den Förderkreis der Fachhochschule Trier
Abschluss: Diplom-Informatikerin (FH)
- 08/1991 – 07/2000 **Abitur am Gymnasium Saarburg**
Leistungskurse: Mathematik, Biologie, Englisch
Abschluss: Allgemeine Hochschulreife

curriculum vitae

FREMDSPRACHEN

Englisch	Fließend in Wort und Schrift
Französisch	Grundkenntnisse
Spanisch	Grundkenntnisse

SONSTIGE PRAKTISCHE TÄTIGKEITEN

- 06/2006 – 07/2006 **University of British Columbia, Vancouver, Kanada**
Laborpraktikum im Department of Cellular and Physiological Sciences
- 05/2006 – 06/2006 **Vancouver General Hospital, Kanada**
Forschungspraktikum im Bereich Medizinische Bildverarbeitung (Neurochirurgie)
- 09/2002 – 02/2003 **Dräger Medical AG & Co. KGa, Lübeck**
Praxissemester im Bereich Entwicklung Intensive Care
- 04/2002 – 06/2002 **Institut für Telematik, Trier**
Wissenschaftliche Hilfskraft im Bereich Telemedizin
- 10/2001 – 02/2002 **Fachhochschule Trier**
Tutorin im Fach Theoretische Informatik
- 02/2001 – 09/2001 **GWI Research GmbH, Trier**
Werksstudentin im Datenbank-Informationsmanagement

PUBLIKATIONEN

- 10/2010 Schwalger, T., Fisch, K., Benda, J., Lindner, B.: *How noisy adaptation of neurons shapes interspike interval histograms and correlations*. PLoS Computational Biology 6:e1001026.

Ehrenwörtliche Erklärung

Hiermit versichere ich, Karin Fisch, dass die vorliegende Arbeit von mir selbständig und nur unter Verwendung der angegebenen Hilfsmittel angefertigt wurde.

München, den 27. Juli 2011

Karin Fisch